

---

En route towards advanced catalyst materials for the  
electrocatalytic water splitting reaction

Mechanistic insights into the formation of metal carbides, phosphides, sulfides and  
nitrides

---

Dissertation

zur Erlangung des akademischen Grades

"doctor rerum naturalium"

(Dr. rer. nat.)

in der Wissenschaftsdisziplin „Materialwissenschaft“

Eingereicht an der Mathematisch-Naturwissenschaftlichen

Fakultät der Universität Potsdam

von

Marc Ledendecker

Potsdam, Januar 2016

This work is licensed under a Creative Commons License:  
Attribution 4.0 International  
To view a copy of this license visit  
<http://creativecommons.org/licenses/by/4.0/>

Published online at the  
Institutional Repository of the University of Potsdam:  
URN [urn:nbn:de:kobv:517-opus4-93296](http://nbn-resolving.de/urn:nbn:de:kobv:517-opus4-93296)  
<http://nbn-resolving.de/urn:nbn:de:kobv:517-opus4-93296>

## Table of Contents

<b>1</b>	<b>Introduction and background</b> .....	<b>1</b>
1.1	Energy situation.....	1
1.2	Hydrogen fuels .....	4
1.3	The water splitting reaction .....	7
1.4	The famous Volcano plot.....	12
1.5	Approaches towards active electrocatalysts.....	15
<b>2</b>	<b>Outline</b> .....	<b>20</b>
<b>3</b>	<b>Nickel and manganese based materials embedded into highly porous nitrogen-doped carbon for the tunable electrocatalysis of HER and OER</b> .....	<b>23</b>
3.1	Background.....	23
3.2	Preparation and characterization .....	25
3.3	Electrocatalytic water reduction and oxidation.....	31
3.4	Material optimization for water oxidation.....	34
3.5	Summary.....	38
<b>4</b>	<b>Ni<sub>3</sub>C nanoparticle formation and its electrochemical performance towards the hydrogen evolution reaction</b> .....	<b>39</b>
4.1	Background.....	39
4.2	Preparation and growth .....	41
4.3	Ni <sub>3</sub> C and its water reduction abilities.....	48
4.4	Summary.....	52

<b>5</b>	<b>Evolution of nanostructured Ni<sub>5</sub>P<sub>4</sub> and its use as cost-efficient bifunctional electrocatalyst towards the HER and OER.....</b>	<b>54</b>
5.1	Background.....	54
5.2	Synthesis, growth and characterization of nickel phosphide .....	55
5.3	Electrocatalytic water splitting reaction .....	65
5.4	Summary.....	83
<b>6</b>	<b>Experimental and theoretical benchmarking of nickel based materials for the hydrogen evolution reaction .....</b>	<b>85</b>
6.1	Background.....	85
6.2	Preparation.....	86
6.3	Adsorption and the famous Volcano plot .....	91
6.4	Summary.....	102
<b>7</b>	<b>Conclusions and perspectives.....</b>	<b>105</b>
<b>8</b>	<b>Appendix.....</b>	<b>111</b>
8.1	Abbreviations .....	111
8.2	Chemicals and materials .....	113
8.3	Experimental part.....	114
8.4	Characterization methods.....	128
<b>9</b>	<b>References .....</b>	<b>138</b>
<b>10</b>	<b>Declaration .....</b>	<b>148</b>

# 1 Introduction and background

---

## 1.1 Energy situation

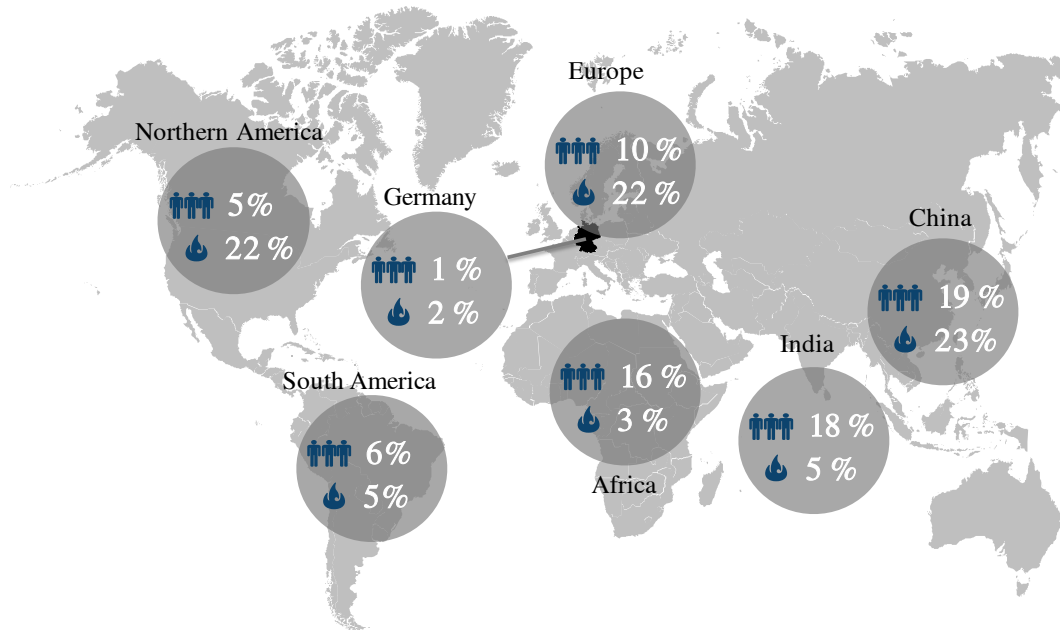


Figure 1: World map with selected countries/areas and their population and energy consumption in percentage on the overall world. Composed from [1, 2].

Increased energy demand, a steadily rising world population and the correlated impact on the environment pose new challenges to the world. Figure 1 displays the population percentage of selected regions and countries with their respective energy consumption.[1, 2] For instance, Europe measures around 10% of the world population and accounts for 22% of the worldwide energy consumption, thus, showing a relatively high consumption per capita as compared to most other regions. Africa and India together contribute to 34% of the world population but account for only 8% of the total energy consumption. Moreover, from 1991 to 2015, the world population increased about 36% whereas in the same time frame, the energy consumption increased about almost 60%.[1, 2] This can also be attributed to the steady economical rise of newly industrialized countries such as China, India, Brazil,

---

Russia (BRIC countries) following the Western countries in economic development. The world population growth is expected to continue leading to about 9.6 billion world inhabitants in the year 2050 which is an increase of around 32% relative to the current world population.[3] Various scenarios of future energy consumption have been developed by energy agencies, climate protection organizations etc. Several of them expect a growth in energy consumption of about 60% in 2050 compared to 2015.[4]

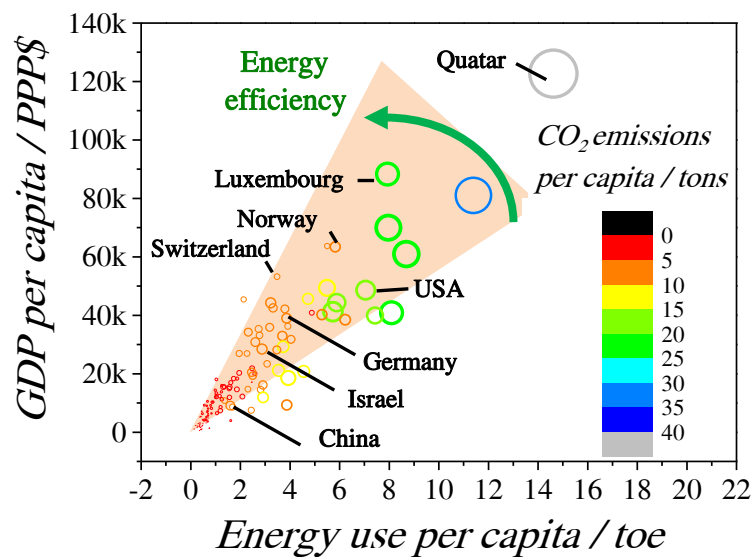


Figure 2: Three dimensional plot of energy use[5], GDP[6] and CO<sub>2</sub> emission[7] per capita in 2009 of most countries on the world. Selected countries are indicated. Beside the x-axis (energy use) and y-axis (GDP) a third dimension was introduced as bubble size/color (CO<sub>2</sub> emission).

Furthermore, when regarding the interdependence between the energy use and gross domestic product (GDP) per capita (Figure 2), a scaling relationship between the two can be observed. By and large, the more energy is used for the production of products, the higher is the economic performance and, going usually hand in hand, the higher the standard of living. Thus, it can be argued, that in order to bring the less developed countries – those in the lower left corner of the graph – a higher standard of living, their GDP needs to increase. Their energy consumption is thereby likely to

increase as well to a degree depending in what sector of economy the country will engage most. However, a certain divergence exists. Hereby, when drawing a line through zero and the respective country's position on the graph, the slope can be interpreted as an indicator for the energy efficiency. In other words, the slope indicates how much value of products and services a person on average in the respective country can produce depending on his or her energy use. Thereby, the steeper the slope, the higher the energy efficiency. On the one hand, countries such as Switzerland or Luxembourg, where the tertiary sector of the economy (e.g. banking, real estate, insurance) plays a significant role, exhibit a high energy efficiency. On the other hand, countries with a large manufacturing sector and high fossil fuel deposits trifle usually more lavishly with their energy, represented by a flat slope. However, the negative impact of the energy production and usage on the environment cannot be overlooked. For instance, the energy consumption is directly linked to the CO<sub>2</sub> emissions, which are indicated in the graph as third dimension (bubble size). This is because the world's energy consumption is mainly based on coal, natural gas, and oil.[8] As fossil fuels are basically fixed in amount due to millions of years of formation, their reserves will deplete sooner or later even though more sophisticated extracting techniques such as off-shore drilling and fracking are increasing the exhaustion time of the reserves. In nature, organisms have specialized in sequestering the aforementioned gaseous released CO<sub>2</sub>. However, since decades, anthropogenic greenhouse gases such as CO<sub>2</sub>, CO and NO have been rising steadily, and a great amount thereof cannot be sequestered (CO<sub>2</sub>: from 280-300 ppmv in the 18<sup>th</sup> century to almost 400 ppmv today).[2, 9, 10] Hence, if the trend of higher energy consumption, further population growth, and increased greenhouse gases continues – what is expected – further ecological, political and social problems will arise. Therefore, the need for regeneratively and sustainably produced energy carriers is still omnipresent, satisfying the energy hunger by circumventing CO<sub>2</sub> emissions.

Different strategies have been developed in order to tackle this energy challenge. Some are based on simple procedures such as changing lifestyle and behavior. A rather near future approach lies in addressing the efficiency of existing power stations or engines. The automotive industry for instance is addressing this problem by manufacturing low-weight cars, recuperation of brake energy, decreasing air resistivity etc. However, these solutions are not designed to diminish greenhouse gases completely. In this context, one approach is based on using no carbon at all – the hydrogen economy.<sup>1</sup>

## **1.2 Hydrogen fuels**

Hydrogen is already used on a large industrial scale, mainly in the *Haber-Bosch process* for the preparation of fertilizers as well as in crude oil refining, and takes around 3% of the global energy consumption.[11] As the world population is steadily rising, the demand for fertilizers to feed the world will even increase in the future along with further need for hydrogen. Nowadays, the primary route to obtain hydrogen encompasses the use of natural gas or other hydrocarbons making the promise of reduced CO<sub>x</sub> emissions redundant. The idea of using regeneratively produced hydrogen as energy storage material has brought up high hopes and promises: hydrogen is a non-toxic gas, possesses the highest heating value per unit mass due to its low weight, and no greenhouse gases are emitted when used as fuel. It can be transported, stored and used directly in non-stationary fuel cells or in combustion engines. However, still facing challenges in finding a proper storage medium due to hydrogen's high diffusivity, low energy density per volume and its wide range of flammability (cf. Hindenburg dilemma) have to be addressed.[12] For stationary

---

<sup>1</sup> *It is believed that different factors are decisive for future years and not only one solution has to be considered but rather many energy storage systems have to be kept in mind.*

---

applications, hydrogen has to stand the competition between grid electricity with much lower energy losses. In daily life, directly used hydrogen is still rather non-existent but in recent years more and more concepts e.g. in cars, bicycles or as portable device charger have been proposed and substantialized. For mobile applications, the hydrogen fuel cell – combining hydrogen and oxygen – is probably the most familiar type of fuel cell. Even though the efficiency of fuel cells using hydrogen and oxygen as fuel lies higher than that of internal combustion engines, the installation costs are still high. Nevertheless, fuel cells can be used in a modular fashion – as e.g. in computers – where facility parts can be adjusted depending on the load. Another advantage over combustion engines is the non-existent emission of carbon dioxide.<sup>11</sup> Non-stationary fuel cells are especially interesting for the transport sector where well-known automotive companies such as GM, Volkswagen, BMW, Toyota and Hyundai are working on different fuel cell concepts.[13] Specifically, a total grid-to-wheel efficiency of slightly less than 30% can be achieved when assuming an electrolyzer efficiency of 70% and a fuel cell efficiency of 40%.[14, 15] In contrast, the efficiency of the best internal combustion engines ranges nowadays between 28% and 32%.[16] However, the latter carries an immense time and development advantage since the automotive industry is pushing the efficiency limits further and further. In 1894, the efficiency of internal combustion engines was no more than 10% as stated by Wilhelm Ostwald. In the same speech, he revealed his ability to think outside the box once more proposing electrochemically converted energy to solve the future energy challenge:

*“what an incomplete thing ... I refer to the steam engine. We obtain no more than 10% ... of the energy of the burning coal in form of mechanical work...”*

---

<sup>11</sup> No carbon dioxide emission is only true when hydrogen is produced from regenerative energy sources. Carbon dioxide emissions from storage and transport processes after production are not considered.

---

*...The way how to solve that biggest of all technical problems, the procurement of cheap energy, this way has to be found through electrochemistry” – Wilhelm Ostwald, 1894*

At this time, he proposed the usage of coal and oxygen as fuel which was too difficult to achieve due to coal's solid character and the accompanied low reactivity.[17] Therefore, gaseous or liquid fuels are preferred in practical fuel cells.

Beside using hydrogen directly, other approaches encompass hydrogen as intermediate for the production of more practical fuels such as methanol, methane, ethylene, diesel or gasoline via *reverse water gas shift* and *Fischer Tropsch*. [18] Hereby, first, syngas is produced at elevated temperatures and converted in a second step into usable hydrocarbons. These platform chemicals can be employed as well in conventional chemical processes for industrial manufacturing. The necessary infrastructure is already in existence so that expenditures for transport, storage and consummation may be reduced. A CO<sub>2</sub> neutral balance can be achieved when using CO<sub>2</sub> for instance from biogas. In Germany, the first industrial plant emerged turning CO<sub>2</sub> from biogas into methane with the help of electrocatalytically won hydrogen. Hereby, the necessary energy is obtained from renewable energy sources such as wind or solar power and turned into hydrogen from water electrolysis. The catalyzed CO<sub>2</sub> reduction yield natural gas that can be fed into the natural gas grid or used directly in cars. [19] Additionally, up to 15% of hydrogen can be directly injected into the natural gas grid circumventing the additional reduction step of CO<sub>2</sub>. [20] Hereby, pure hydrogen can be delivered directly through existing natural gas pipelines defraying the costs for additional infrastructure. Additional use of hydrogen lies in hydrogenation reactions of biomass which can be converted into useful building blocks. Nevertheless, the focus should lie rather in the usage of industrial by-products instead of propelling the competition between food and fuel. Biomass waste such as

for instance lignin from paper industry consist of polymeric fragments rich in aromatic units that can be potentially converted into useful chemicals.[21] In this manner, greenhouse gases are circumvented and waste quantities are substantially reduced. However, hydrogen is obtained mostly from natural gases, even though innovative production paths display interesting alternatives. In the *Kvaerner process* for instance, the problem of CO<sub>x</sub> emissions is circumvented creating only carbon black and hydrogen from hydrocarbons.[22]

### 1.3 The water splitting reaction

Another promising route encompasses the use of electrocatalytically produced hydrogen in combination with renewable energy sources such as wind or solar energy (“*power-to-gas*”). Hydrogen is hereby one of the most promising choices. As basis, water embodies a promising starting material due to its abundance, reasonably high hydrogen content and non-existent carbon content. By now, electrocatalytically won hydrogen has a market share of around 5% (especially in combination with the *chloralkali process*).[8] This is due to the fact that the costs of hydrogen produced by electrolysis are directly linked to the costs for electricity. It becomes obvious that countries with surplus electricity such as Egypt, Norway or Canada with high hydroelectric potential have a need for proper saving methods. When using renewable energy sources such as wind or solar radiation, the surplus of energy produced in off-peak times can be stored in chemical bonds and used in busy peak times.

#### 1.3.1 Fundamentals

When considering the hydrogen production from water, one has to be aware that the H-O bonds in water are strong bonds and their separation requires considerable amount of energy. The total water splitting reaction ( $2H_2O(l) \rightarrow 2H_2 + O_2$ ) can be divided into the hydrogen evolution reaction (HER;  $2H_2O + 2e^- \rightarrow H_2 + 2OH^-$  in

alkaline,  $2H^+ + 2e^- \rightarrow H_2$  in acidic medium) and the oxygen evolution reaction (OER;  $4OH^- \rightarrow 2H_2O + 4e^- + O_2$  in alkaline,  $2H_2O \rightarrow 4e^- + 4H^+ + O_2$  in acidic medium). By definition, the standard potential of the HER lies at 0 V vs. reversible hydrogen electrode (RHE) whereas the OER takes place 1.23 V vs. RHE. The potential difference of both reaction corresponds to a Gibbs free energy of  $\Delta G = -nFE_0 = 237.2 \text{ kJ mol}^{-1}$  at 25 °C where F displays Faraday's constant, n the number of electrons transferred and  $E_0$  the standard electron potential. The minimum potential of 1.23 V is dictated by thermodynamics but in practice, the reaction will proceed at much higher applied voltages due to a not to be underestimated kinetic term decreasing the total efficiency (Equation 1.1).

$$E_{tot} = E_0 + \eta_A + \eta_C + iR \quad 1.1$$

where  $\eta_A$  and  $\eta_C$  correspond to the anodic and cathodic overpotential and i to the circulating current. Additionally, further resistances (R) due to e.g. bubble formation and blocking of catalyst surface, bad electrical wiring or solution resistances have to be taken into account. These resistances can be reduced by clever engineering through e.g. cell optimization or forced convection. In electrocatalysis, the same principles as in classical heterogeneous catalysis apply, namely, to catalyze a specific reaction with the help of a solid surface. The catalyst plays a critical role due to diffusion of educts towards the catalyst surface, its adsorption and dissociation. The emerged intermediates recombine followed by desorption and subsequent diffusion away from the catalyst. Hereby, microscopic understanding is necessary in order to understand the greater picture of surface catalysis. For the hydrogen evolution, the elementary steps will be elaborated further. Contrarily to outer sphere reactions, the hydrogen evolution occurs directly on the surface of the catalyst and is highly dependent on the material characteristics. Hereby, two different reaction pathways exist and are illustrated in Table 1: the *Volmer-Tafel* and the *Volmer-Heyrovski* path. The *Volmer-Tafel* reaction pathway follows a *Langmuir-Hinshelwood* mechanism

where first a proton (from  $H^+$  in acid,  $H_2O$  in base) will be reduced in order to form a catalyst bound intermediate  $H_{ad}$  (*Volmer* step). Subsequently, two  $H_{ad}$  recombine in a homolytic bond making fashion to form  $H_2$  (*Tafel* step).

Reaction step	Reaction	Solution	Equation
Volmer	$H^+ + e^- \rightarrow H_{ad}$	acid	1.2
	$H_2O + e^- \rightarrow H_{ad} + OH^-$	base	
Tafel	$2H_{ad} \rightarrow H_2$	acid/base	1.3
Heyrovski	$H_{ad} + H^+ + e^- \rightarrow H_2$	acid	1.4
	$H_{ad} + H_2O + e^- \rightarrow OH^- + H_2$	base	

Table 1: Possible elemental steps in the two electron involved hydrogen evolution reaction.

The *Volmer-Heyrovski* pathway follows an *Eley-Rideal* mechanism in a heterolytic bond making fashion. The first step comprises – as before – the adsorption of hydrogen followed by recombination of  $H_{ad}$  and a proton ( $H^+$  in acid,  $H_2O$  in base) from solution.

In order to reduce the kinetic hindrances, active materials are used, catalyzing the HER or OER at low overpotentials with high exchange current densities. These last two mentioned parameters are part of the *Butler-Volmer equation* (BVE) used as base for the treatment of electrochemical kinetics. For a certain (back and forth) reaction, the BVE is characterized by an anodic and a cathodic term as indicated in equation 1.5.

$$i = i_0 \left[ \underbrace{\exp\left(\frac{\alpha_a n F \eta}{RT}\right)}_{\text{anodic part}} - \underbrace{\exp\left(\frac{\alpha_c n F \eta}{RT}\right)}_{\text{cathodic part}} \right] \quad 1.5$$

where  $i$  corresponds to the current density,  $i_0$  to the exchange current density,  $n$  to the number of electrons transferred,  $\alpha$  to the transfer coefficient (anodic or cathodic),  $F$  to Faraday's constant ( $96,485 \text{ C mol}^{-1}$ ),  $\eta = (E - E_{\text{equil}})$  to the necessary overpotential,  $R$  to the gas constant and  $T$  to the temperature.

The activation overpotential includes energy losses related to activation energies of a certain reaction. At higher overpotentials, either the anodic or the cathodic term becomes negligible with respect to the other and the whole term can be simplified to the so-called *Tafel equation*. Equation 1.6 and 1.7 show the *Tafel equation* for the anodic and the cathodic term, respectively.

$$i_a = i_0 \exp\left(\frac{\eta}{b}\right) \quad 1.6$$

$$i_c = i_0 \exp\left(-\frac{\eta}{b}\right) \quad 1.7$$

where  $b$  corresponds to the *Tafel slope*. The current density  $i_{c/a}$  in logarithmic form can be plotted as a function of overpotential, thus, providing information about two important parameters, the *Tafel slope*  $b$  and the exchange current density  $i_0$ . Ideally, when comparing catalytic performances, the *Tafel equation* can supply profound insights in e.g. reaction mechanisms and the rate determining step (RDS) for a certain reaction. Under real life conditions, however, other factors such as mass transport effects and the existence of other adsorbates may play a role and have to be considered. The *Tafel slope* is usually expressed in  $\text{mV dec}^{-1}$  and should be as small as possible whereas  $i_0$  is usually expressed in  $\text{mA cm}^{-2}$  and should be as large as possible. However, this generalization holds not always exactly true. In photoelectrocatalysis for instance, the limiting factor is determined by the incoming flux of photons from the sun and less current densities (up to  $20 \text{ mA cm}^{-2}$ ) are required. Here, the *Tafel slopes* plays only a secondary role since a logarithmic increase in current density is of less repercussion than in industrial electrolyzers where much higher current densities

are needed. The delicate relationship between *Tafel slope* and exchange current density is displayed in Figure 3. Even though catalyst A demonstrates a small *Tafel slope*, the exchange current density is also small compared to B. Therefore, catalyst A, not active at low overpotentials, becomes alluring at high potentials indicated by the intersection of the two current voltage lines.

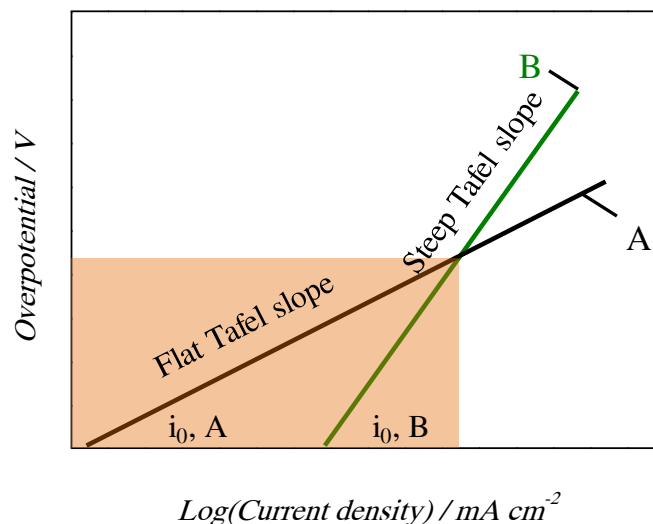


Figure 3: Schematic relationship of Tafel slope and exchange current densities of two different catalysts A and B. Adapted from [23].

Even though the catalytic activity is one of the most important factors for catalysis research, a universal determination method does not exist. Many methods are described in literature with their respective advantages and disadvantages. One way of evaluating the catalytic activity is using the exchange current density through extrapolation of the *Tafel equation*. However, despite all efforts, various groups obtained considerably differing results in exchange current densities depending on the experimental environment. For instance, exchange current densities for platinum have been found to differ several orders of magnitude when measuring conditions were changed.[24, 25] Additionally, the exchange current density displays an extensive quality and is therefore dependent on the apparent surface area.

Furthermore, the comparison of exchange currents may be misleading as the *Tafel slope* plays a critical role. Alteration in mechanism at higher overpotentials leads to changed *Tafel slopes* and therefore to changed exchange current densities. Secondly, when using porous materials, non-linear *Tafel plots* arise, and the determination of  $i_0$  is not trustworthy.[26] Despite all theoretical discussions, one should keep in mind that the purpose of a catalyst is to operate at practical current densities keeping the overpotential as small as possible. In this manner, a more practical way to report catalytic performance consists in reporting overpotentials at certain current densities such as e.g.  $1 \text{ mA cm}^{-2}$ ,  $10 \text{ mA cm}^{-2}$ , or  $100 \text{ mA cm}^{-2}$ . [27] In commercial electrocatalysis, anode and cathode materials are held at high potentials in order to achieve high current densities up to  $10 \text{ A cm}^{-2}$ . Hereby, the kinetic losses are immense. However, industry hazards the consequences since increased current density means size reduction of the electrolyzer thereby saving investment costs. The cathodic side of the water splitting reaction also plays a great role in the *chloralkali process* where chlorine evolves on one electrode and hydrogen/ $\text{OH}^-$  on the other. As the *chloralkali process* constitutes the main “modus operandi” to produce sodium hydroxide, immense amounts of electricity are needed. In the same fashion as in the water splitting reaction, cost-efficient catalysts demonstrating low overpotentials are wished for.[28]

#### **1.4 The famous Volcano plot**

Different approaches have been tried in order to understand the catalytic performance of different materials correlating the catalytic activity with the work function, lattice constants, potential of zero charge, or even electronegativity.[29] Ultimately, only a few remain, namely those related to the free energy of adsorption  $\Delta G$  of a hydrogen atom to the surface.[30] With the raise of computational power in recent years, the descriptor  $\Delta G$  can be theoretically calculated indicating how well  $\text{H}_{\text{ad}}$

---

binds to a certain surface. A graphic depiction of  $\Delta G$  vs. catalytic activity results in a volcano plot. Volcano plots in electrochemistry have been a useful tool in order to predict catalytic activity only by taking into account the adsorption energy of the intermediates  $\Delta G$ . These considerations are based on the Sabatier principle stating that neither too tightly bonded (endothermic) nor too weakly bonded (exothermic) intermediates will result in a good catalyst. For a multi-electron reaction such as e.g. the OER, it is much more difficult to predict due to the great amount of possible intermediates than for a two-step reaction where the reaction invariably involves one adsorbed intermediate. Trasatti's version of the Volcano plot from 1972 for the hydrogen evolution in acidic environment is shown in Figure 4. Due to lack of data at this time, the energy for hydride formation was used instead of using adsorption energies.

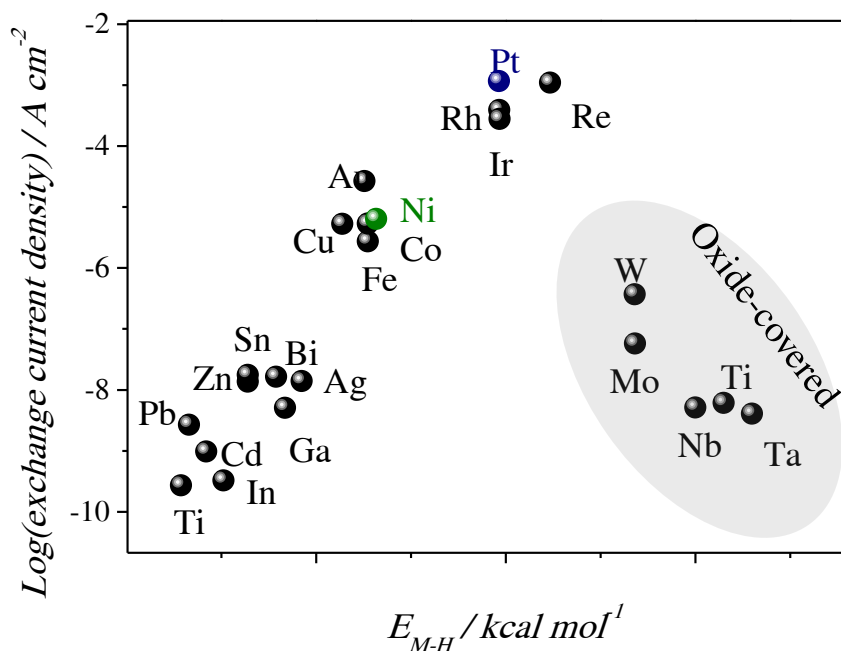


Figure 4: Volcano plot from Trasatti and coworkers for the HER. Nickel and platinum are encountered throughout the entire thesis and are marked respectively. Data taken from [31].

There is still some dispute even in recent literature about the exact position of certain metals on the Volcano.[32, 33] However, in more recent plots, the adsorption energies are displayed on the x-axis whereas the catalytic activity (e.g. in form of exchange current density) is plotted on the y-axis. The vertex of the graph displays the optimum binding energy ( $\Delta G = 0$ ) proposed by Parsons in 1958.[34] The ascending branch ( $\Delta G > 0$ ) indicates hindered adsorption of the intermediates whereas the descending branch ( $\Delta G < 0$ ) indicates too tightly bonded intermediates, blocking the active surface area. As indicated in Figure 4, the left branch of the volcano is populated with transition metals such as nickel, iron or cobalt. The best performing materials are situated on top including platinum and iridium. The right branch of the volcano was composed of metal oxides, not known at the time when Trasatti and coworkers were compiling the described plot. As experimental values were based on oxide covered surfaces, not on pristine surfaces, a non-existence of the descending branch for pristine metals was assumed.[33] Interestingly, composite materials with non-metals in their structure as molybdenum sulfide or metal phosphides can also be found on the opposite branch than their pristine metal congeners.[35, 36] Hereby, new adsorption sites arise due to more complex crystal structures.  $\text{MoS}_2$  for instance, adopts a hexagonal structure and belongs to the layered transition metal dichalcogenides. In the basal plane of the layered structure, either sulfur or molybdenum is surface terminating and it was found that this plane was rather inactive for the HER. Additionally, the observed activity towards the HER was much higher than theoretically predicted due to more active edge sites perpendicular to the layered structure.[37] By now, however, systematic studies of the heteroatom influence on the hydrogen adsorption are still pending and will be addressed in the following work.

## 1.5 Approaches towards active electrocatalysts

In general, the prerequisites of a competitive and well working catalyst are cost-efficiency, durability and efficiency. However, very often, an all-in-one solution is difficult to obtain due to the complex requirements. Nevertheless, in the following, strategies are presented how to improve every single mentioned aspect.

### 1.5.1 Efficiency

As a general rule, small *Tafel slopes* and high exchange current densities are desired. Expressed in a more practical way, catalysts demonstrating high current densities at a low overpotential are sought after. Hereby, noble metals as platinum or iridium are the most efficient hydrogen evolution catalysts. Their intrinsic properties make them thereby the state-of-the-art catalysts towards the hydrogen evolution.

#### 1.5.1.1 Catalytically active sites: electronic or rather geometric?

However, basically two strategies exist in order to increase the catalytic performance, namely: altering the inherent properties of a catalyst or increasing the number of active sites. First, strategies how to alter the intrinsic properties are presented. The Volcano plot can be taken thereby as guideline for the conception of advanced catalysts as it is based on the inherent properties of a material. Pristine metals are located on a fixed and not adjustable position on the volcano making it difficult to disclose superior performing materials. In this context, the possibility exists that new materials with altered inherent properties evolve when pure metals are alloyed with each other.[38] Miles proposed in 1975 that the combination of two metals, one from the ascending and one from the descending branch of the volcano, may result in platinum mimicking behavior.[39] When the right metals are chosen, the electronic properties are positively changed resulting in optimized intermediate adsorption. For instance, nickel in combination with molybdenum has shown higher activity for the synthesis of ammonia than pristine metals.[40] The hydrogenolysis of aryl ethers was

---

promoted using binary Ni/TiN composite materials.[41] Also in fuel cells, combinatorial approaches led to improved catalysts where activity goes in line with alloy composition.[42] With the rise of technology, Edisonian research became more and more convenient where theoretical calculations of hundreds of alloys in a high throughput fashion can determine the best catalyst.[43] Moreover, many powerful catalysts evolved through fine tuning of morphology or shape and designing catalysts with specific crystallographic facets.[37, 44] Other approaches comprise the incorporation of non-metals into the metallic structure altering the structure and thereby the chemical and physical properties. In this context, ceramic materials such as carbides, nitrides, sulfides and phosphides have shown high corrosion resistance, activity, electric conductivity and long-term stability at much lower cost.[45, 46, 47, 48, 49, 50] Additionally, these material classes are still rather unexplored towards the HER and OER despite their unique properties. However, the first attempts to enhance activity by altering the crystal environment were already rendered in 1964.[51] Hereby, activation of electrocatalytically active materials was achieved by non-metal incorporation as arsenic, sulfur, tellurium or antimony. As for each transition metal, several crystal structures exist – depending on the heteroatom – there is still room to ascertain the optimum catalyst. In nature, the core-structures of hydrogenase are composed of transition metals such as iron or nickel building metal-sulfur clusters that are able to catalyze the HER near the thermodynamic limit.[52] However, in strong basic and acidic environment, their performance typically drops rapidly due to decomposition of the protein structure. Another reason why enzymes are not directly used for industrial electrocatalysis lies in their bulky structure and low amount of catalytic sites per area making them rather impractical for e.g. portable devices. Inspired by nature, a series of metal sulfides such as  $W_2S$  or  $MoS_2$  have been demonstrated to be viable counterparts to noble metals in the water reduction reaction.[37, 53] In this context, molybdenum was already used relatively early as HER

catalyst but rather in combination with nickel and sulfur than as pristine metal.[54, 55] Furthermore, earlier work did not observe high activity of MoS<sub>2</sub> due to the reduced amount of active sites and its comparatively low electric conductivity perpendicular to the layered structure. Nanostructuring allowed isolating electrocatalytically active edge sites where inactive basal planes were reduced in amount.[37]

In the previous paragraph, the attention was focused on intrinsic properties of a catalyst to enhance its activity. Another, rather simple approach encompasses the maximization of active sites by enhancing surface area and porosity. Hereby, the turnover of reactants is directly correlated to the amount of active sites available. This goal can be achieved on the one hand by preparation of nanoparticles or clusters with high surface to volume ratio. Subsequently, active catalyst can be anchored onto inert, high surface area support with optimized porosity. On the other hand, the design of pores inside catalytically active materials tailored towards specific reactions and reactants propel higher catalytic rates. For instance, the fabrication of pores with higher surface area than its bulk counterpart is used for instance in zeolites or porous carbons.[56, 57] In this context, nanostructuring helps reactant and product transportation thereby providing increased diffusion pathways along with increased surface areas and high amount of active sites.

### **1.5.2 Cost-efficiency**

Despite all efforts in recent years, platinum is still the most efficient hydrogen evolution catalyst by now. Nevertheless, it belongs also to the most expensive metals. Different strategies have been employed in order to reduce the catalyst's costs. One approach lies in reducing the noble metal amount by alloying it with low cost metals such as bismuth, copper or nickel.[43, 58, 59] In this manner, only a fraction of costly noble metals is necessary but yet keeping its high performance. Another route

towards cost-efficient catalysts encompasses the use of ceramic materials as carbides, phosphides, sulfides or nitrides that are assimilating platinum performances in many heterogeneous reactions.[60, 61] In addition, the costs for sulfur, phosphorus, carbon or nitrogen (depending on the precursor) are only a fractional part to the one of platinum.[62] However, it should be kept in mind that the electrocatalyst is only one part of the full system and the investment costs of the whole electrolyzer has to be taken into account.

### **1.5.3 Stability**

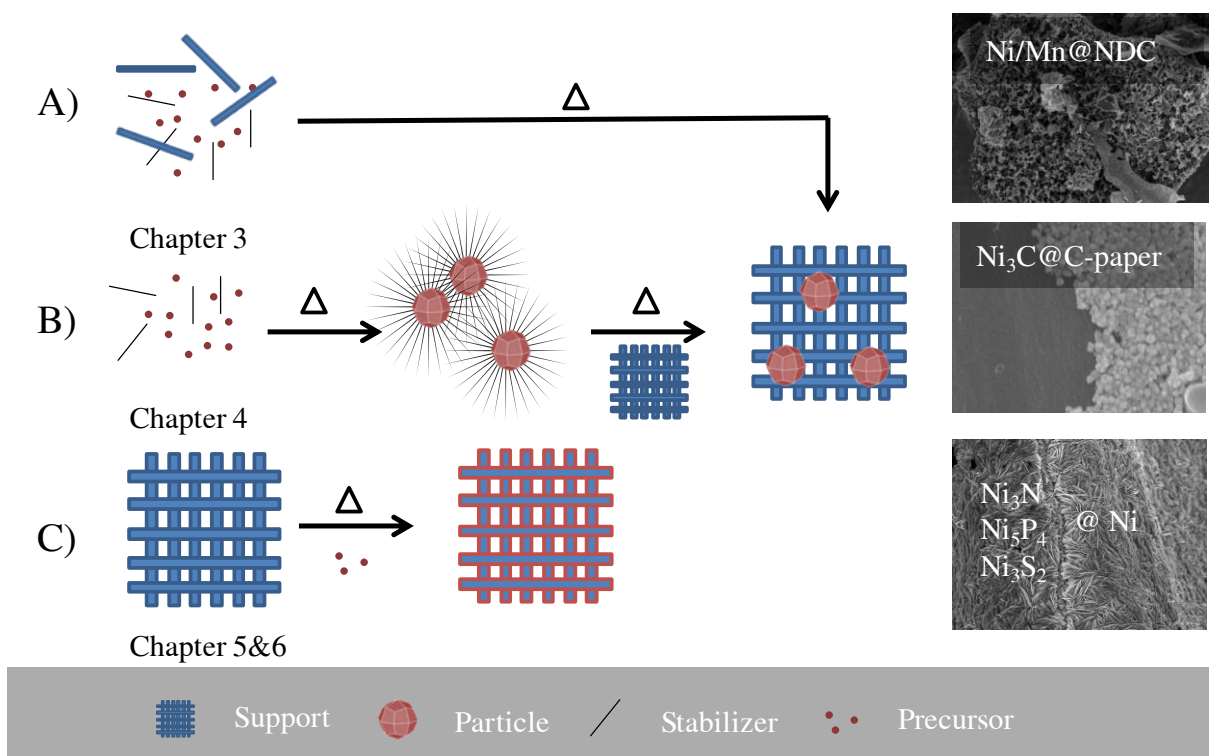
In industrial electrolyzers, high electrolyte conductivities are necessary since ohmic losses scale directly with current density. These losses can be minimized using concentrated electrolytes predicted by *Kohlrausch's law*. [63] In this manner,  $H^+$  and  $OH^-$  are often used due to their high conductivity and electrocatalytic testing is often performed at highly acidic or basic conditions. Therefore, materials bearding these harsh conditions are crucial, and only a few materials have proven to accept this challenge. Noble metals as Pt, Ir or Ru are not only employed due to its high efficiency but also due to their high corrosion resistance and stability in acidic medium. Nevertheless, other materials demonstrated also high corrosion resistance in the past. Tungsten for instance displays resistivity against corrosion especially in nonoxidating acids.[64] However, its hydrogen evolution performance is rather mediocre. Nevertheless, when mixed with carbon to form tungsten carbide – a material known for its hardness - high performance towards the HER was observed while keeping its stability.[65] Another prominent example displays  $MoS_2$  demonstrating high stability in acidic solution (cf. chapter 1.5.1).[66] Mostly, material's corrosion resistance is tested towards a certain reaction. However, from a practical point of view, corrosion at open circuit has to be taken into account. Nickel for instance can be used as catalyst for the HER in acidic solution. Nevertheless, when the electrolyzer is shut down for technical service, unforeseen power shutdown, etc.

and the electrode is not cathodically polarized, dissolution of the electrode cannot be detained.[67] Assessing the material's corrosion resistance at open circuit conditions is therefore critical.

## 2 Outline

---

Climate destabilizing carbon emissions, soaring energy demands and depleting fossil fuels. The energy economy has lost its bearing and is therefore seeking alternative technologies that will rise up to this challenge. Electrocatalytically won hydrogen is hereby one of the most promising routes for sustainable energy storage. However, the separation of the strong O-H bond requires considerable amount of energy and by now, rare noble metals are performing best. For this task, advanced catalysts are necessary, preferentially made from earth abundant materials, with high performances and high selectivity in order to reduce negative environmental impact. Research groups all over the world are ardently working on the development of new classes of catalysts. In this thesis, new catalysts based on pristine metals and ceramic materials such as nitrides, carbides, sulfides and phosphides are introduced contributing to the challenge of enhanced performance and stability at low costs. As basis, nickel was chosen for further modification as it is wildly used in industrial processes such as hydrotreating of crude oil, methanation, steam reforming, or the hydrogenation of vegetable oil.[68] The attentive reader will have noticed the involvement of hydrogen in all of the mentioned processes. In addition, nickel as 3d transition metal is relatively abundant and approximately 4,000 times less expensive than e.g. platinum (on a per mole basis) with less susceptibility to supply fluctuations.[69] In the same manner, heteroatoms as sulfur, phosphorus, carbon and nitrogen are relatively cost-efficient depending on the precursor. In this context, the *Sabatier principle* will be a constant companion throughout this thesis and will be used as guideline for the design of advanced catalysts.



*Scheme 1: Schematic depiction of employed synthesis strategies outlined in this thesis. The first synthesis route (A) encompasses the transformation/modification of already existing support into catalytically active material. In this manner, Ni<sub>3</sub>S<sub>2</sub>, Ni<sub>3</sub>P<sub>4</sub> and Ni<sub>3</sub>N are synthesized. In the second route (B), nanoparticles (Ni<sub>3</sub>C) are synthesized and brought onto high surface area carbon support. The last strategy (C) is based on the simultaneous formation of catalyst (Ni/Mn) and support in a one-pot ionothermal synthesis.*

The employed synthesis strategies are introduced in Scheme 1. Route A encompasses a one-pot ionothermal synthesis strategy and offers the advantage of less synthesis steps involved where high surface area support is formed simultaneously with the active catalyst anchored onto the support material (chapter 3). Route B consists of nanoparticle (Ni<sub>3</sub>C) preparation with high surface areas using stabilizing agents. It will be shown that understanding of the formation mechanism and occurring phase transformations is obtained. Its electrocatalytic behavior towards the HER will be accentuated. This synthesis route has the advantage of precise tuning of every preparation step (chapter 4). Route C shows the direct conversion of support material forming the active catalyst on top. Based on nickel perforated plates that are used in industrial electrolyzers, the presented route is therefore rather industry-friendly where already existing electrodes can easily be modulated.[70]

High performance can be achieved when using high surface area substrates such as e.g. foams. However, not only the increased number of sites results in the high performance but also the change of intrinsic properties evaluated by theoretical calculations. Hereby, profound insights into the intrinsic properties of sulfides, nitrides and phosphides as catalysts towards the HER will be obtained (chapter 5 & 6). Despite the fact that the presented synthesis strategies differ drastically from each other (gas phase reactions, ionothermal preparation, or wet chemistry in organic solvents), they are united by one goal pursued in this thesis: to understand the driving mechanism of growth behind. As the formation mechanism of these materials is particularly important for further enhancement, detailed insights in how these materials are formed are given. Furthermore, strategies in order to reduce necessary overpotentials are discussed. The fundamental steps taking place during the HER and OER on the catalyst's surface are pinpointed and deeper understanding on the mechanism is obtained.

### **3 Nickel and manganese based materials embedded into highly porous nitrogen-doped carbon for the tunable electrocatalysis of HER and OER**

---

#### **3.1 Background**

In this chapter, the facile preparation of metallic nanoparticles embedded into highly porous carbon support with high surface area is highlighted. As nanoparticles are often unstable and prone to surface oxidation due to their high surface energy, they are e.g. imbedded inside of pores, anchored on support materials or stabilized by structural promoters. Typical supports enclose alumina (steam reforming, water gas shift reaction, hydrogenation reaction), titania (selective catalytic reduction/DeNO<sub>x</sub>) or carbon (hydrogenation reaction).[68] Certainly, carbon supports are highly competitive due to the low weight, high abundance of carbon, chemical/mechanical stability and their electrical conductivity.[71, 72] For carbon based supports, removal of templates can be challenging – especially in industrial process – and conventional methods as hard and soft templating suffer from the use of e.g. hazardous chemicals. Thus, greater practical relevance is highly desirable. Antonietti and coworkers employed molten salts as concurrent template and reaction medium. Hereby, it was possible to obtain tailored N-, B-, or O-doped carbons with high porosities depending on the carbon precursor and the salt melt composition.[73, 74, 75] In this manner, the formation of pores is mechanistically initiated by enclosing of salt clusters by the polymerizing organic matrix. Thus, the prerequisite is the molten state of the salt and sound miscibility of salt and precursor. In industrial processes, molten salts have been employed as reaction medium for instance in the *Hall-Héroult process* for smelting aluminum. Hereby, pristine alumina with a melting point over 2,000 °C is mixed with

---

cryolite, a low melting aluminum salt and the molten state can be reached already close to 1000 °C.[76] A vast range of properties as synergy effects to the precursor or melting temperature exist depending on the utilized salt mélange. Thereby, the salts composition can be tuned ranging from ionic alkali metal halides to salts with more covalent character as borates or silicates. The versatility and high potential of salt melts as reaction medium was demonstrated for the preparation of e.g. metal borides, silicon carbide or boron carbon nitride nanostructures.[77, 78, 79] Furthermore, the (usually) low price, non-toxicity and easy removal make salt melts highly competitive for the synthesis of hierarchical micro and mesoporous support material. In general, the preparation of the support itself can be laborious and challenging and often contains hazardous chemicals.

To vanquish this aspect, catalyst and support were synthesized simultaneously in a one-pot ionothermal synthesis. The advantages clearly lie in circumventing long-lasting separation procedures and purification of intermediates saving resources and time. Hereby, an advanced approach towards the synthesis of highly porous carbons is presented where nickel/manganese particles are formed *in-situ* in their corresponding metal halide melt. Furthermore, high metal loadings and surface areas up to 1,000 m<sup>2</sup> g<sup>-1</sup> were attained. It will be shown that manganese incorporation will increase the performance towards the HER predicted by *Sabatier's principle*. Furthermore, tailoring of electrocatalytic properties of the material towards the HER and OER will be delineated through simple surface oxidation. Careful characterization of morphology, composition and surface characteristics will be given by powder X-ray diffraction (PXRD), scanning electron microscopy (SEM), high resolution transmission electron microscopy (HR-TEM), high angle annular dark field - scanning transmission electron microscopy (HAADF-STEM), electron energy loss spectroscopy (EELS), thermal gravimetric analysis (TGA), nitrogen sorption measurements, elemental analysis (EA) and inductively coupled plasma optical emission spectrometry (ICP-OES)

---

measurements. The catalytic behavior towards OER and HER will be copiously evaluated by linear sweep voltammetry (LSV), chronopotentiometry (CP) and cyclic voltammetry (CV) measurements.

### 3.2 Preparation and characterization

Drawing upon the mentioned concept of ionothermal synthesis, a facile and straightforward synthesis strategy for manganese incorporation into the high surface area structure was developed. As precursor, dicyanodiamide (DCDA) was chosen due to its two-fold function as building block of the nitrogen-doped (N-doped) carbon matrix and its reduction ability releasing  $N_2$ . Furthermore, LiCl,  $NiCl_2$  and  $MnCl_2$  were not solely selected as templates but also as catalyst precursors (Figure 5). The combination of LiCl,  $NiCl_2$  and DCDA was successfully employed by Shalom and coworkers who gave chapter and verse for the catalytic relevance of high surface area materials for the hydrogenation reaction of nitrobenzene to aniline.[80] The used molar ratio of each component can be found in Table S1. The sample denotation is designed as  $Mn_xNi_y$  where X and Y display the molar ratio of the indicated metal used as starting material where the DCDA and LiCl amount was kept constant. Among these salts, LiCl possesses the lowest melting point of 610 °C, followed by manganese chloride (650 °C) and nickel chloride (1030 °C).[81]

Depending on the salt melt ratio, a reduced melting point can be achieved. Moreover, it is known that metals can dissolve in their own molten halide salt and homogeneous distribution of metal on nitrogen-doped carbon (NDC) is therefore imaginable.[82] For instance, it has been reported that more than 9 mol% of pristine nickel can dissolve in its own chloride salt at 977 °C.[81] The salt templating effect was evaluated by comparing the surface area before and after washing (Figure S2). The surface area increased more than fifty times after salt removal with surface areas of almost 1000

$\text{m}^2 \text{g}^{-1}$  and average pore size diameters in the mesoporous dimensions (Table S2). When the pores were released from embedded salt, nickel/manganese nanoparticles embedded into nitrogen-doped carbon were obtained.

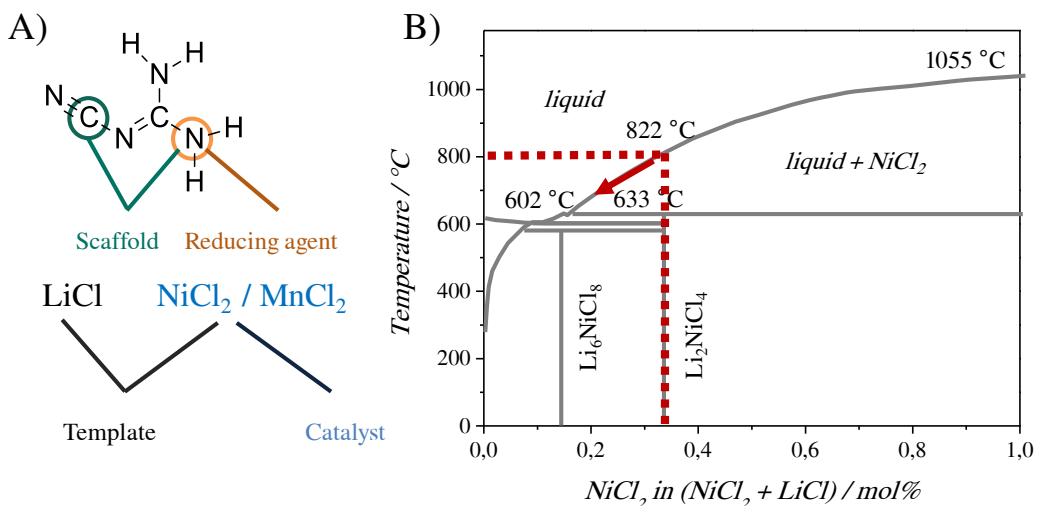


Figure 5: A) Multifunctional precursor in the synthesis of Ni/Mn containing nitrogen-doped carbon. B) Phase diagram of NiCl<sub>2</sub>/LiCl. The dashed line indicates the ratio of NiCl<sub>2</sub>/LiCl used in the starting materials. The phase diagram was adapted from [83].

As shown later, nickel chloride plays a crucial role in the structure formation of high surface area carbon. Therefore, the simplified system NiCl<sub>2</sub>/LiCl/DCDA (Mn<sub>0</sub>Ni<sub>1</sub>) was studied in more detail. The phase diagram of NiCl<sub>2</sub> and LiCl is shown in Figure 5. The dashed line indicates the molar ratio of the used salts. Temperature studies revealed formation of crystalline Ni(NCN) at 500 °C along with low surface area (Figure 6). The nitrogen to carbon ratio drops from 2:1 to 1.4:1 (close to carbon nitride - C<sub>3</sub>N<sub>4</sub>, 1.33) and nickel can still be found as Ni(II). In the starting mixture, the salt ratio was chosen not to melt exactly at the eutectic point but rather contain higher amounts of NiCl<sub>2</sub>. Since the latter reacts with the organic precursor to form Ni<sub>x</sub>N<sub>y</sub>C<sub>z</sub>, NiCl<sub>2</sub> diminishes and the NiCl<sub>2</sub>/LiCl salt ratio converges towards a lower melting point (red arrow in Figure 5). At 600 °C, the transformation towards hexagonal Ni<sub>3</sub>C/Ni<sub>3</sub>N was observed from PXRD along with increased surface area (Figure 6). It was demonstrated that

nitrogen acts as reducing agent for nickel – comparable to a carbothermal reduction – as the reduction of Ni(II) to Ni(I) is accompanied by a N to C ratio drop of almost 50%. As N<sub>2</sub> also embodies the leaving group, it could possibly bear the ability to act as pneumatogen – foaming agent – thereby initiating porosity. The surface area, however, increases the most between 700 °C and 800 °C where the melting process is set in motion and the nitrogen content is already relatively low. It is therefore concluded that activation in form of nitrogen release is not the substantial driving force in building up porosity but rather the molten state of the salt. At 700 °C, the hexagonal structure of Ni<sub>3</sub>C/Ni<sub>3</sub>N vanished and structural dense cubic nickel evolved. The isotherm at 500 °C corresponds to type V, characteristic for missing micropores, rather weak adsorbent-adsorbate interactions and distinct hysteresis (H3) with missing limiting adsorption at high  $p^*p_0^{-1}$  (Figure 6). TEM/SAED images (Figure 6) are in line with PXRD results where Ni(NCN) evolved at 500 °C followed by the subsequent transformation into Ni<sub>3</sub>N/Ni<sub>3</sub>C at 600 °C. At  $T \geq 600$  °C, the isotherm changes to type IV where Mn<sub>0</sub>Ni<sub>1</sub> adsorbs more and more in the microporous region. This is well in line with the alteration of hysteresis type from H3 at 500 °C and 600 °C to type H4 at higher temperatures indicating the formation of slit pores.[84] Due to partial melting of the salt mixture, carbonization around not melted salt cluster occurred at 700 °C. After washing with water, sphere-like structures around the salt clusters were observed from TEM (Figure 6). Furthermore, full melting of the salt mélange with increasing temperature led to smaller pore sizes. The pore size distribution narrowed, calculated by non-local density functional theory (NLDFT, slit pores) along with structural reinforcement of the carbon matrix (Figure 6). Only recently, also Pampel and Fellingner demonstrated that high porosity can be gained when working not exactly at the eutectic point. Moreover, porosity could be accurately tuned when moving away from the eutectic point and pore sizes, pore volume and surface area could be tailored towards platinum resembling ORR activity.[85]

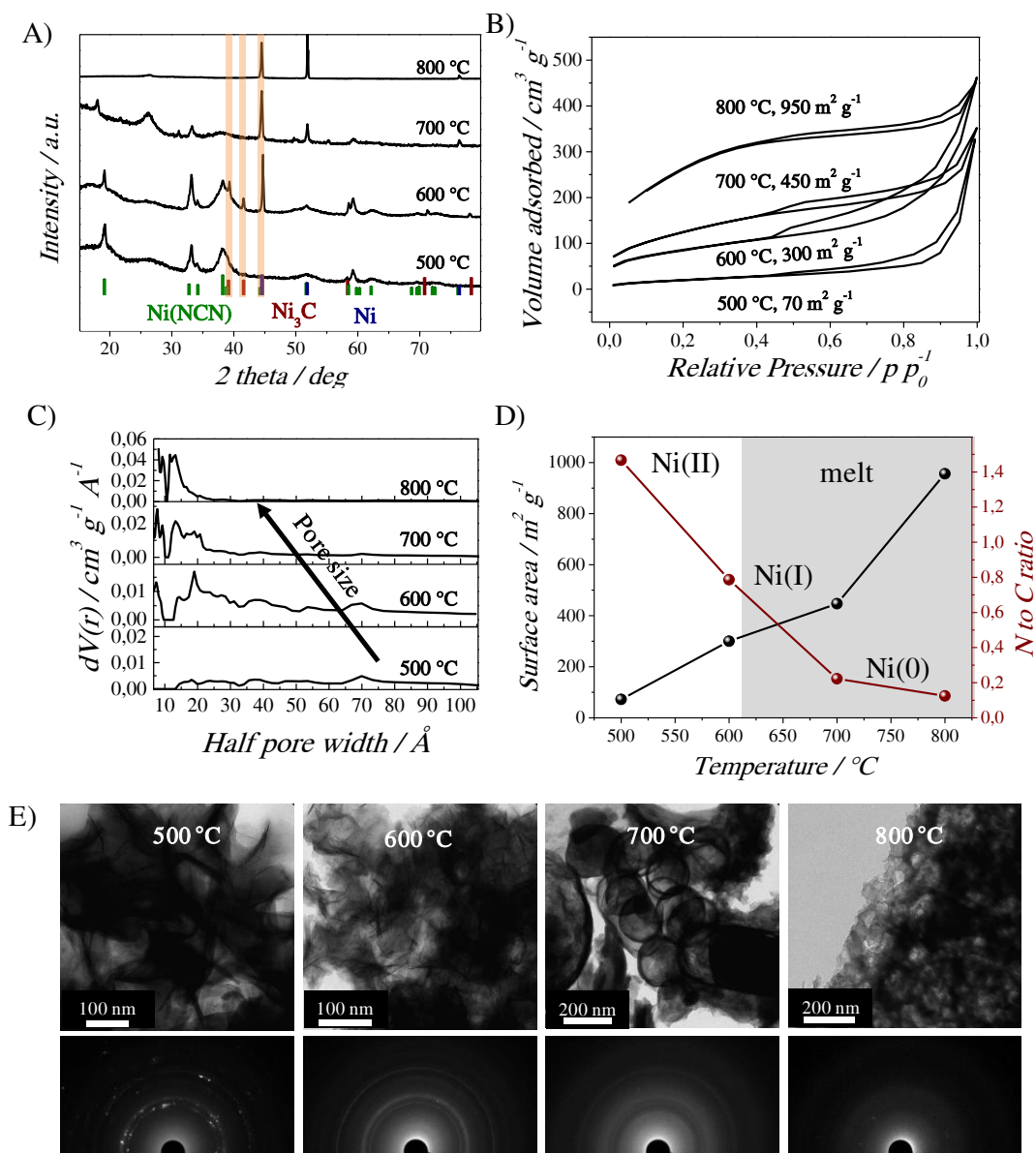


Figure 6: Temperatures studies based on  $Mn_0Ni_1$ . A) PXRD with  $Ni(NCN)$  (ICDD: 04-016-9769),  $Ni_3C$  (ICDD: 00-004-0853) and  $Ni$  (ICDD: 04-008-845) as reference pattern. B) Nitrogen sorption isotherms and the corresponding pore size distribution (C). D) Temperature dependence of surface area obtained from nitrogen sorption analysis and N/C ratio obtained from elemental analysis. E) TEM and SAED of  $Mn_0Ni_1$  at different temperatures after washing.

Hereby, a larger amount of micropores was found when working directly at the eutectic point presumably due to sound miscibility of carbon precursor in the molten salt. However, mesopores are not less important especially when considering transport of reactants and products to/from the active catalyst.

The heating process of  $\text{NiCl}_2/\text{LiCl}/\text{DCDA}$  ( $\text{Mn}_0\text{Ni}_1$ ) was monitored by means of a high temperature heating mantel where temperatures up to  $615\text{ }^\circ\text{C}$  could be reached. Thereby, the transformation during temperature increase was directly monitored through a transparent quartz flask. First, partial sublimation of organic precursor (white/pale yellow) was observed below  $500\text{ }^\circ\text{C}$ , presumably an antecedent of carbon nitride due to condensation reactions of DCDA.[86] Subsequently, the content of the flask darkened with increased temperature speaking for carbonization. However, melting was not observed at  $615\text{ }^\circ\text{C}$ . This is in line with nitrogen sorption results where lower surface areas were obtained at  $500\text{ }^\circ\text{C}$  and  $600\text{ }^\circ\text{C}$  compared to higher temperatures. The phase diagram also predicts partial melting at  $\sim 633\text{ }^\circ\text{C}$  when taking only the starting salt mixture into account. However, as mentioned before, nickel chloride diminished with increasing temperature forming  $\text{Ni}_x\text{N}_y\text{C}_z$ . As direct consequence, the  $\text{LiCl}$  to  $\text{NiCl}_2$  ratio rises leading to a shift in melting point to a lower temperature as indicated in Figure 5. Between  $600\text{ }^\circ\text{C}$  and  $700\text{ }^\circ\text{C}$ , the salt (partially) melted accompanied with the formation of micropores and an increase in surface area. Full melting was assumed between  $700\text{ }^\circ\text{C}$  and  $800\text{ }^\circ\text{C}$  where the surface area increased by almost 100%. From TEM images (Figure 6), it was concluded that the structure still rearranged after  $700\text{ }^\circ\text{C}$  due to the disappearance of the sphere-like structures speaking for full melting of the solid salt remains and reconstruction of the nitrogen-doped carbon matrix.

When nickel was used in excess in the starting materials ( $\text{Mn}_x\text{Ni}_y$ ;  $Y > 0.1$ ), cubic nickel reflections were observed while no and low amount of nickel led to mixtures of  $\text{Mn}_x\text{O}_y$  and unidentified reflections (PXRD, Figure 7). Hereby, a shift of the  $d(111)$ ,  $2\Theta = 44.5\text{ }^\circ$  reflection is attributed to larger manganese atoms incorporated into the cubic nickel structure resulting in unit cell adaptation as demonstrated before ( $\text{Mn}_{0.018}\text{Ni}_{0.982}$  – ICDD: 04–011–9057,  $\text{Mn}_{0.22}\text{Ni}_{0.78}$  – ICDD: 04–003–2244,  $\text{Mn}_{0.5}\text{Ni}_{0.5}$  – ICDD: 04–004–8458).[87] Figure 7 shows  $\text{Mn}_1\text{Ni}_1$  after synthesis at  $800\text{ }^\circ\text{C}$  under the influence of a

magnetic field. Hereby, the entire sample is drawn to the magnet indicating high nickel loading inside/on the carbon/nitrogen matrix. ICP-OES underpins the obtained results where high amount of nickel precursor in the starting materials led to low amounts of manganese (~1-2%, Table 2).

Sample	C [wt%]	N [wt%]	Mn [wt%]	Ni [wt%]
Mn <sub>0</sub> Ni <sub>1</sub>	40	5	-	19
Mn <sub>0.1</sub> Ni <sub>1</sub>	39	3	0.6	22
Mn <sub>0.5</sub> Ni <sub>1</sub>	37	5	0.8	18
Mn <sub>1</sub> Ni <sub>1</sub>	40	4	1.6	19
Mn <sub>1</sub> Ni <sub>0.5</sub>	35	4	1.8	21
Mn <sub>1</sub> Ni <sub>0.1</sub>	38	2	12	19
Mn <sub>1</sub> Ni <sub>0</sub>	10	7	20	-

*Table 2: Nitrogen and carbon content obtained from elemental analysis, manganese and nickel content measured via ICP-OES.*

Up to 12 wt% (Mn<sub>1</sub>Ni<sub>0.1</sub>) and 20 wt% (Mn<sub>1</sub>Ni<sub>0</sub>) of manganese was found when the manganese/nickel ratio was increased. Presumably, due to the high surface area, oxides form during the washing/storing process accounting for the residual mass (together with not washed-out salt). The necessity of nickel chloride for the formation of pores was revealed by nitrogen sorption analysis comparing nickel chloride with other transition metal chlorides (Mn, Fe, Co). In the absence of NiCl<sub>2</sub>, only low surface areas were observed even though the melting points lie at lower temperatures for all three systems (Figure 7).[88] From the isotherms, almost no adsorption in the micropore/early mesopore region was found for iron, cobalt and manganese. This finding accentuates the necessity of miscibility and interaction of carbon precursor with the chosen salts. Presumably, the increased phase separation led to less

interaction of salt and precursor and therefore to low surface area. Moreover, the morphology changed from an open pore structure and high interconnectivity for high nickel to manganese ratios ( $Mn_xNi_y$  for  $Y > 0.1$ ) to a flower like structure ( $Mn_1Ni_{0.1}$ ) when using smaller ratios (Figure S1). Primary particles in the size of  $\sim 100$  nm were observed when no nickel was used in the starting material (Figure S3,  $Mn_1Ni_0$ ). Exemplarily, the SEM image of  $Mn_0Ni_1$  is shown in Figure 7.

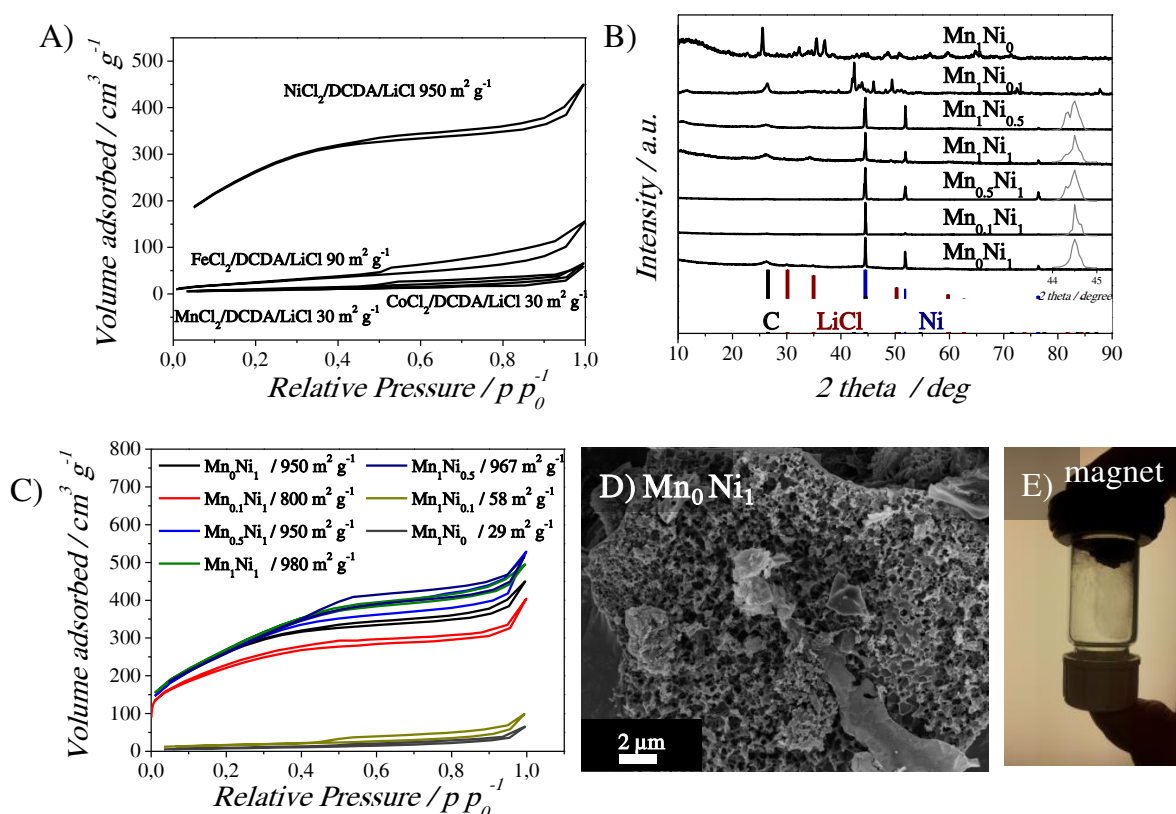


Figure 7: A) Nitrogen sorption isotherms replacing nickel chloride by iron, cobalt and manganese chloride as precursor and the corresponding surface areas. B) PXRD pattern of  $Mn_xNi_y$  samples and C) the corresponding nitrogen sorption data. D) SEM image of  $Mn_0Ni_1$ . E)  $Mn_1Ni_1$  after synthesis at  $800\text{ }^\circ\text{C}$  with a magnet on top demonstrating the high nickel loading.

### 3.3 Electrocatalytic water reduction and oxidation

The influence of alloyed materials based on nickel and manganese is already known for the oxygen reduction reaction.[89] However, the influence of manganese-doped nickel towards the HER and OER is – to the best of the author’s knowledge – not

reported. This is not startling since theoretically obtained hydrogen adsorption energies on manganese are still very limited. However, when taking mechanistic studies into account, conclusions on the nature of the binding state can be drawn. For manganese, it has been proposed that the first step of hydrogen adsorption (*Volmer* step) is rate determining under acidic conditions.[90] Therefore, the binding of hydrogen on manganese is expected to be rather loose and only low coverages are expected. Nickel on the other hand binds hydrogen ( $H_{ad}$ ) rather tight (cf. chapter 6.3) and the combination of these two materials may result in higher electrochemical performances towards the HER than pristine nickel (or manganese) as proposed by Miles and others.[39, 43] In line with the drawn expectations, manganese doping into the nickel structure resulted in lower overpotential with higher current densities compared to pristine nickel ( $Mn_0Ni_1$ ). Figure 8 shows that the best catalyst possesses 1.6 wt% of manganese ( $Mn_1Ni_1$ ) along with a small HER onset and an overpotential of 0.36 V at  $-10 \text{ mA cm}^{-2}$ .

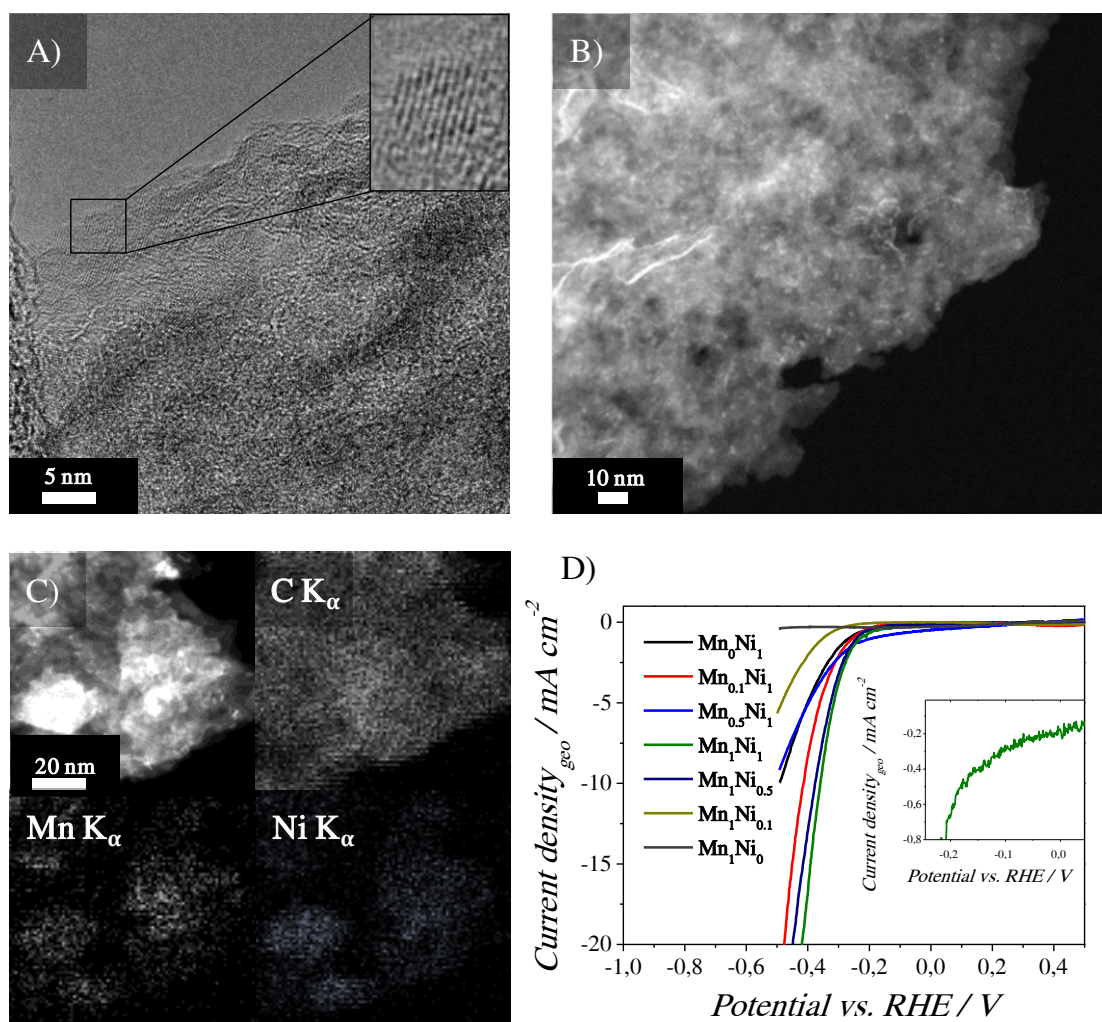


Figure 8: A) HRTEM, B) HAADF-STEM and C) EDX measurements of  $Mn_1Ni$  – the best HER catalyst<sub>1</sub>. D) Current voltage characteristics of  $Mn_xNi_y$  measured in 0.1 M KOH at 400 rpm. The inset shows the low overpotential below 0.2 V for  $Mn_1Ni_1$ .

A possible explanation of the enhanced activity lies in the adsorption of hydrogen at the nearby nickel surface ( $H \leftrightarrow Ni-H_{ad}$ ) and recombination from another  $H_{ad}$  (*Tafel step*) or from  $H_2O_{sol}$  (*Heyrovski step*) takes place at manganese to form  $H_2$ . Another explanation could lie in the promotion of water dissociation ( $H_2O + e^- \leftrightarrow H+OH^-$ ) at the manganese surface since the HER is usually inferior in alkaline solution compared to acidic environment.[91] Moreover, electron donating from one metal to the other may change physical properties resulting in altered hydrogen evolution rates.[92, 93] In favor of the proposition of embedded metal nanoparticles, the distribution of

manganese and nickel investigated by high angle annular dark field-scanning transmission electron microscopy (HAADF-STEM) suggested small particles (brightest area) embedded into the amorphous NDC matrix (Figure 8). However, from Scherrer's equation applied to the Ni, d(111) peak,  $2\Theta = 44.5^\circ$ , particles over 50 nm were expected. It was therefore conjectured that smaller particles coexist with bigger particles. Additionally, EDX elemental mapping revealed nickel and manganese in close vicinity speaking for probable incorporation of manganese into the nickel structure (Figure 8). EELS (Figure S4) underpinned a high carbon to nitrogen ratio and higher amount of nickel compared to manganese. The Mn/Ni ratio determined by EELS exceeded two times the ratio obtained from ICP-OES which can be explained by the smaller probe size of EELS and a not fully homogeneous particles distribution. From the carbon peaks, it was concluded that mainly amorphous nitrogen-doped carbon formed with some graphitic carbon (287 eV) in accordance with PXRD where a small d(002),  $2\Theta = 26^\circ$  reflection from graphitic carbon was observed (Figure 6). It is noted that  $Mn_1Ni_1$  showed an increase in performance after activation treatment (100 cycles between 0.4 V and -0.4 V vs. RHE, not shown here). Possible reasons are reduction of surrounding oxide layers during cycling or removal of carbon either from the particles directly or by creating diffusion pathways through the NDC matrix.

### **3.4 Material optimization for water oxidation**

As pointed out earlier, nickel based materials are acclaimed and well-known as anode materials in non-noble metal based electrolyzers.[67, 94] In the oxygen evolution catalyzed on metal surfaces, the reaction takes place at the metal oxide surface since the dissociation energy of the  $O_2$  bonds is weaker than the M-O bond strength. In this context, *Pourbaix diagrams* are highly helpful, revealing the dependency of pH, potential and present species. The *Pourbaix diagram* for nickel is illustrated in Figure 9.[95] At the conditions worked at – indicated as orange line in Figure 9 – the active

---

catalyst for the HER is based on pristine nickel whereas the active catalyst for the OER consists of higher nickel oxides. To be more precise, first, nickel hydroxides ( $\text{Ni}(\text{OH})_2$ ) are formed followed by nickel oxyhydroxide ( $\text{NiOOH}$ ) formation during OER. However,  $\text{Ni}/\text{Mn}@/\text{NDC}$  exhibited only moderate performance towards the OER in alkaline medium. Moreover, a decrease in performance was observed with increasing incorporated manganese amount expressing the tighter binding of oxygen on manganese (Figure S5).[96] It is noted that the OER may not only be dependent on active metal centers but also on nitrogen-doped carbon acting as active catalyst as described recently.[97] The high performance was ascribed to easy adsorption of  $\text{OH}^-$  on the positive carbon centers and the subsequent recombination of two adsorbed oxygen species. However, vast differences were found in catalytic performances compared to the ones described later in chapter 5 for nickel phosphide (Figure 9). One reason for the low activity may lie in surrounding carbon layers preventing the formation of active catalyst. Corroboration of this conjecture was given by electrochemical aging experiments. For pure nickel with free access to active centers, electrochemical cycling accelerates the formation of active catalyst in the form of nickel oxyhydroxides. In the case discussed here, however, repetitive cycling in the range of 1.05 - 1.80 V vs. RHE did not increase the performance significantly as observed for pristine nickel (Figure 9). Therefore, a rather straightforward approach was selected encompassing the activation of nickel/manganese particles to form oxides and to remove (partially) their surrounding carbon shell by post-annealing. Thus, the challenge was to maintain the NDC scaffold and subsequently activate the embedded/anchored metals. The temperature was selected according to TGA revealing no material loss below 300 °C (Figure S5). The respective metal oxide formation during benign annealing treatment at 300 °C for 10 h was assessed by PXRD (Figure S6). The morphology remained principally the same confirming the preservation of NDC during annealing (Figure S1). Nevertheless, the catalytic activity

in the HER and OER differed considerably after oxidation. The performance towards the OER improved notably, lowering the necessary overpotential along with increased current densities (including the slope, Figure 9). For the HER, the converse effect eventuated after oxidation (Figure 9). An explanation for the decreased performance on the HER side may lie in the favored cleavage of the H-OH bond on metal oxide while the conversion of  $H_{ad}$  to  $H_2$  is impaired.[98, 99] Another aspect that should not be forgotten is the poor electrical conductivity of NiO contributing to the low HER activity.[100]

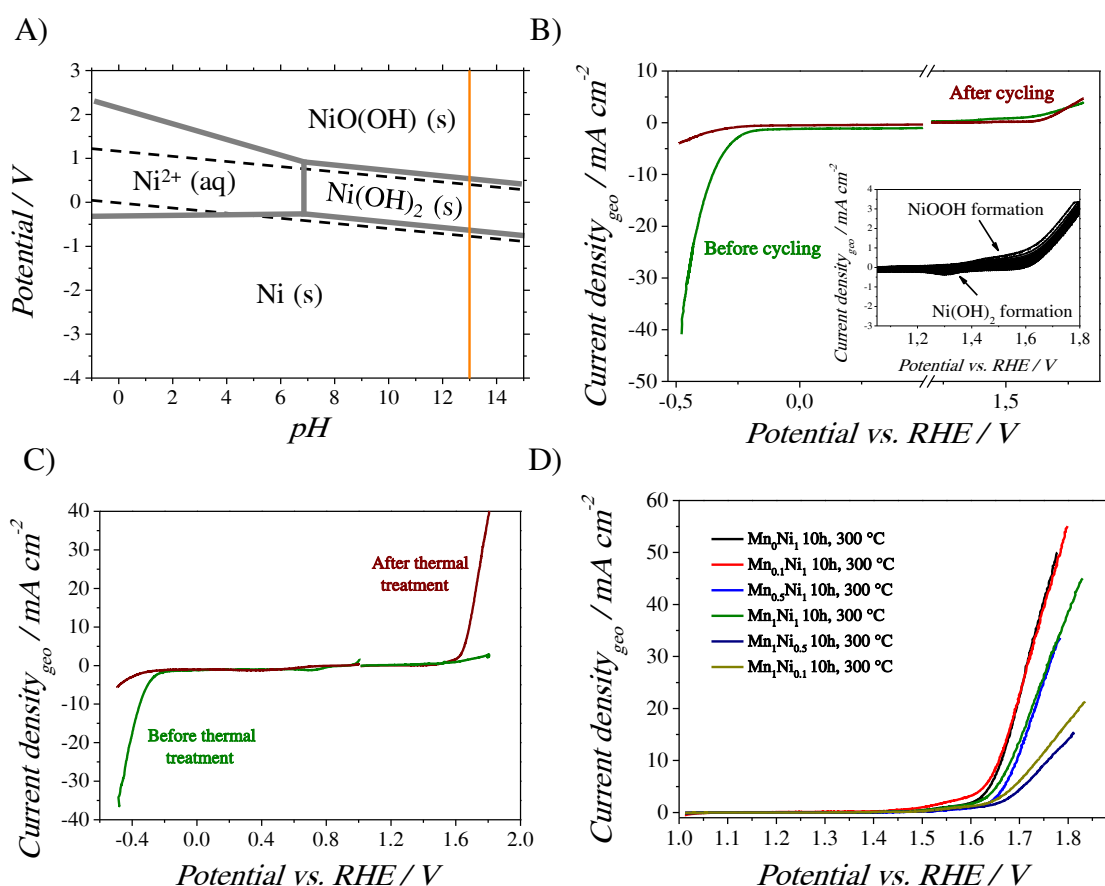


Figure 9: A) Pourbaix diagram of nickel displaying the dependency of pH and applied potential on the present specimen. The orange line represents the pH worked at in this chapter.[95] B) Electrochemical performance of  $Mn_1Ni_1$  before (green) and after (red) electrochemical cycling (500 cycles, 1.05 - 1.8 V vs. RHE, inset). C) LSV of  $Mn_1Ni_1$  before (green) and after (red) oxidation at 300 °C for 10 h. D) Oxygen evolution reaction of  $Mn_xNi_y$  after air oxidation at 300 °C for 10 h. All curves are  $iR$  corrected.

The most active OER catalyst ( $\text{Mn}_{0.1}\text{Ni}_1$ ) was studied more in detail varying the annealing time between 0 h and 15 h at 300 °C (Figure 9). From PXRD, distinctive NiO reflections evolved after 10 h (Figure S7). When the sample was heated for 15 h, the carbon and nitrogen content dropped drastically and the pore structure collapsed leading to low surface area along with low catalytic performance (Figure 9, Table S3). These changes were also observed by electron microscopy (Figure S8). While structure and morphology were substantially maintained at low oxidation times (0 h – 10 h, 300 °C), longer oxidation times (15 h) supported the disintegration of the material. The heating time directly influenced the electrochemical activity towards the OER. The best catalyst evolved after 10 h heating time with an onset overpotential of  $\sim 0.36$  V and current densities of  $10 \text{ mA cm}^{-2}$  at  $\sim 0.42$  V overpotential. Consequently, the surface area was preserved while NiO was sufficiently formed. When the structure collapsed after 15 h, only small current densities were monitored. Figure 10 displays the correlation of surface area and electrocatalytic performance. At first, the catalytic performance augmented with increasing annealing time and even higher surface areas were obtained presumably due to the liberation of small amounts of carbon in form of  $\text{CO}_x$  (cf. activated carbon).

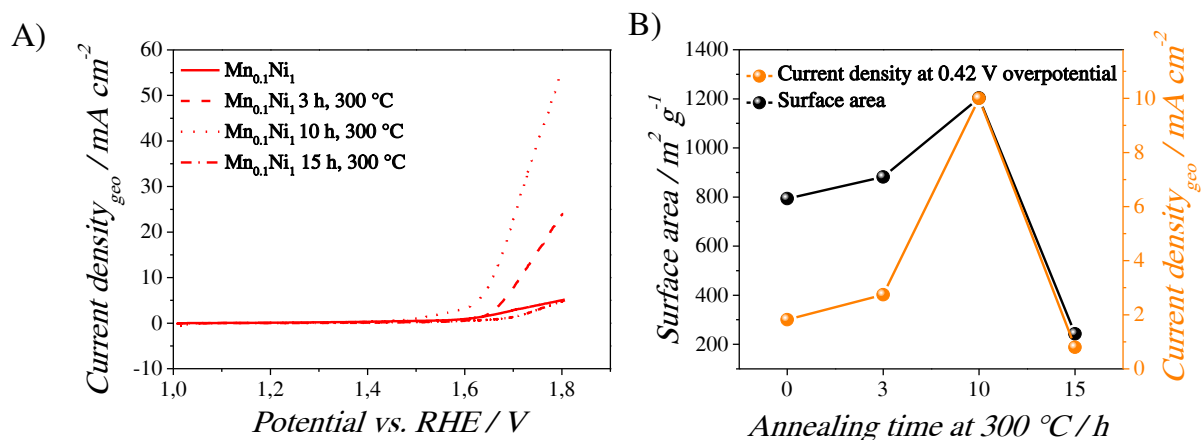


Figure 10: A) Fine tuning of oxidation time of  $\text{Mn}_{0.1}\text{Ni}_1$  at 300 °C. B) Dependency of oxidation time at 300 °C on the surface area and catalytic performance of  $\text{Mn}_{0.1}\text{Ni}_1$ .

After 15 h, the performance and surface area attenuated notably. The catalyst exhibited analogous current densities before and after oxidation treatment for 15 h while the surface area decreased more than fourfold. It is therefore proposed that surface area and nickel oxide formation have a synergetic effect on the electrocatalytic performance towards the OER.

### 3.5 Summary

In this chapter, the preparation of highly porous composite materials with high surface areas and high metal loadings was demonstrated. By using multifunctional precursors, nitrogen-doped carbon as support material was formed *in-situ* along with embedded manganese-doped nickel particles. The activity towards the HER was directly affected by the amount of manganese incorporated into the structure resulting in low onset potentials (< 0.2 V). While a low performance was observed in the OER for  $Mn_xNi_y$  directly after synthesis, benign oxidation led to substantial increase of the oxygen evolution rate. It is therefore suggested that a synergetic effect of surface area and metal oxidation led to an increased performance towards the OER. Thereby, surface areas up to  $1,200 \text{ m}^2 \text{ g}^{-1}$  were constituted while simultaneously removing surrounding carbon layers and forming nickel oxide. By dividing the thermodynamically predefined cell potential (1.23 V) by the onset potential necessary to govern full water splitting, a total voltage efficiency of 70% was obtained. Expectantly, the portrayed materials are alluring candidates for other hydrogen involving reactions such as e.g. methanation,  $\text{CO}_2$  reduction, steam reforming or, in general, hydrogenation reactions. The facile tailoring of electrocatalytic properties towards water oxidation and reduction offers new synthetic possibilities for other metal/oxide based materials especially for energy related applications.

## 4 Ni<sub>3</sub>C nanoparticle formation and its electrochemical performance towards the hydrogen evolution reaction

---

### 4.1 Background

In this chapter, the preparation and growth of Ni<sub>3</sub>C nanoparticles will be highlighted. It will be shown how these nanoparticles evolve from thermodynamically unstable phases followed by recrystallization and incorporation of carbon. It will be demonstrated that the synthesis - following a temperature ramping pathway - results in homogeneous nanoparticles with low size distribution despite a not obvious burst of nucleation as for instance in the hot injection approach. Hereby, direct experimental support of the briefly sketched *Ostward's rule of stages* of Ni<sub>3</sub>C nanoparticle formation will be given. On the basis of *Pearson's hard and soft acid and basis* concept, strategies are proposed towards further size-tuning by adequate choice of ligands. To round up, surveying kinetic parameters in the HER will shed light onto the reaction mechanism and additional application potential in other energy-related areas will be discussed.

In the water splitting reaction, nanoparticles such as e.g. MoS<sub>2</sub>,<sup>[101]</sup> Mo<sub>2</sub>C, Mo<sub>2</sub>N,<sup>[46]</sup> or NiSe<sup>[102]</sup> have evolved as highly attractive materials for electrocatalysis due to their high surface area to volume ratio and their conspicuous electronic and catalytic properties. However, their high surface area makes them thermodynamically unstable and thereby prone to agglomeration. Stabilization in form of stabilizers as organic ligands or solid support is therefore needed. As demonstrated later in this work, theoretical calculations and experimental observations unraveled high

---

electrocatalytic performance towards the HER for  $\text{Ni}_3\text{N}$  due to distinct hydrogen adsorption sites not present in its pure metal congener (chapter 6). Nickel nitride's isotopic counterpart  $\text{Ni}_3\text{C}$  consists of interstitial carbon filling the spaces in the octahedral holes of the formerly face-centered cubic lattice of nickel. Thus, it is highly likely that  $\text{Ni}_3\text{C}$  behaves in a similar manner than  $\text{Ni}_3\text{N}$ . Nevertheless,  $\text{Ni}_3\text{C}$  exhibits higher lattice dilation due to an increased atom radius of carbon (0.76 Å) in comparison to nitrogen (0.71 Å) and similar but noticeable performance towards the HER is therefore expected.

Previously, nickel carbide was synthesized by ballmilling[103], chemical vapor deposition[104] or in classical colloidal routes.[105, 106, 107, 108] Due to the high dependency on reducing conditions and temperature, metal or mixed composites were often obtained.[109, 110, 111] Colloidal routes in high boiling solvents (200-320 °C) are based on the reduction of soluble  $\text{Ni}^{n+}$  salts in the presence of surfactants stabilizing the nanoparticles. By using reactive carbon precursors in the starting materials, carbon can be incorporated into the nickel structure. In literature, some discrepancy about the exact structure exists.[112, 113, 114, 115] To be more specific, it is still under debate whether the formed crystals are hexagonal  $\text{Ni}_3\text{C}$  or rather hexagonal nickel. For pristine nickel, two different crystal configurations can be found in literature, a face centered cubic (fcc) and a hexagonal closed pack (hcp) structure. The thermodynamic more stable form is hereby cubic nickel. Different groups have interpreted their formed crystals as hexagonal nickel, with similar crystal structures as  $\text{Ni}_3\text{C}$ . However, the synthesis of hexagonal nickel is often accompanied using carbon containing starting materials and it is still under debate if metastable hexagonal nickel is not always misinterpreted with  $\text{Ni}_3\text{C}_x$  ( $X \leq 1$ ). Further light will be therefore shed onto this aspect during the following discussion.

## 4.2 Preparation and growth

Drawing upon the aforementioned colloidal synthesis routes, nickel(II) acetylacetonate ( $\text{Ni}(\text{acac})_2$ ), oleylamine (OA) and 1-octadecene (ODC) were used as precursors.[107] The synthesis was realized at a temperature of 320 °C with 1-octadecene as high temperature boiling solvent and oleylamine as organic stabilizer, solvent and reducing agent.[116].  $\text{Ni}(\text{acac})_2$  was selected as nickel precursor due to its relatively high decomposition point decomposing in acetone at around 200 °C and  $\text{CO}_2$  at around 270 °C.[117]. The reaction time of  $\text{Ni}_3\text{C}$  nanoparticle growth was varied constantly from 3 min to 60 min. By immediate quenching of the solution from 320 °C to room temperature (RT) within a few seconds, the growth was interrupted and the intermediates analyzed. This was realized by applying an overpressure to the closed system where the only way out was through a metal tube connected to another flask through a septum. The aliquot was intercepted and stored under nitrogen atmosphere. Direct determination of size, crystallinity and crystal structure was achieved using TEM/SAED measurements. Understanding the growth processes is crucial in order to improve and adapt existing synthesis strategies. The rapid growth of these particles is elucidated in Figure 11. The nanoparticles in the beginning are rather amorphous ( $< 5 \text{ nm}$ ). With the passage of time, cubic nickel reflections evolve ( $5 \text{ nm} \geq \text{crystal size} \leq 15 \text{ nm}$ ) with reduced grain numbers that are susceptible to phase transformation (Figure 11). These findings are in line with classical metal nanoparticle synthesis where nickel ions are reduced to yield nickel monomers.[118, 119] With increasing reaction time, the crystallinity rises and carbon can be incorporated into the nickel structure forming  $\text{Ni}_3\text{C}$ . After 10 min, cubic nickel is completely converted into hexagonal  $\text{Ni}_3\text{C}$  (SAED, Figure 11). Carbon is thereby already incorporated during the growth. From a mechanistic point of view, these observations can be explained by the *Ostwald rule of stages*, stating that the initial least dense species will form first and through intermediary steps, increase gradually in density and usually in

stability.[120] In line with the proposed mechanism, amorphous, metastable spherical nanoparticles in the size range of ~3 nm were observed in the beginning. Interestingly, thermodynamically favored and denser cubic nickel emerged first suggesting indirectly that the hexagonal structure evolves through incorporation of carbon. The formation mechanism buttress thereby previous reports stating that hexagonal nickel most likely possesses incorporated carbon, nitrogen or hydrogen in its structure.[107, 121]

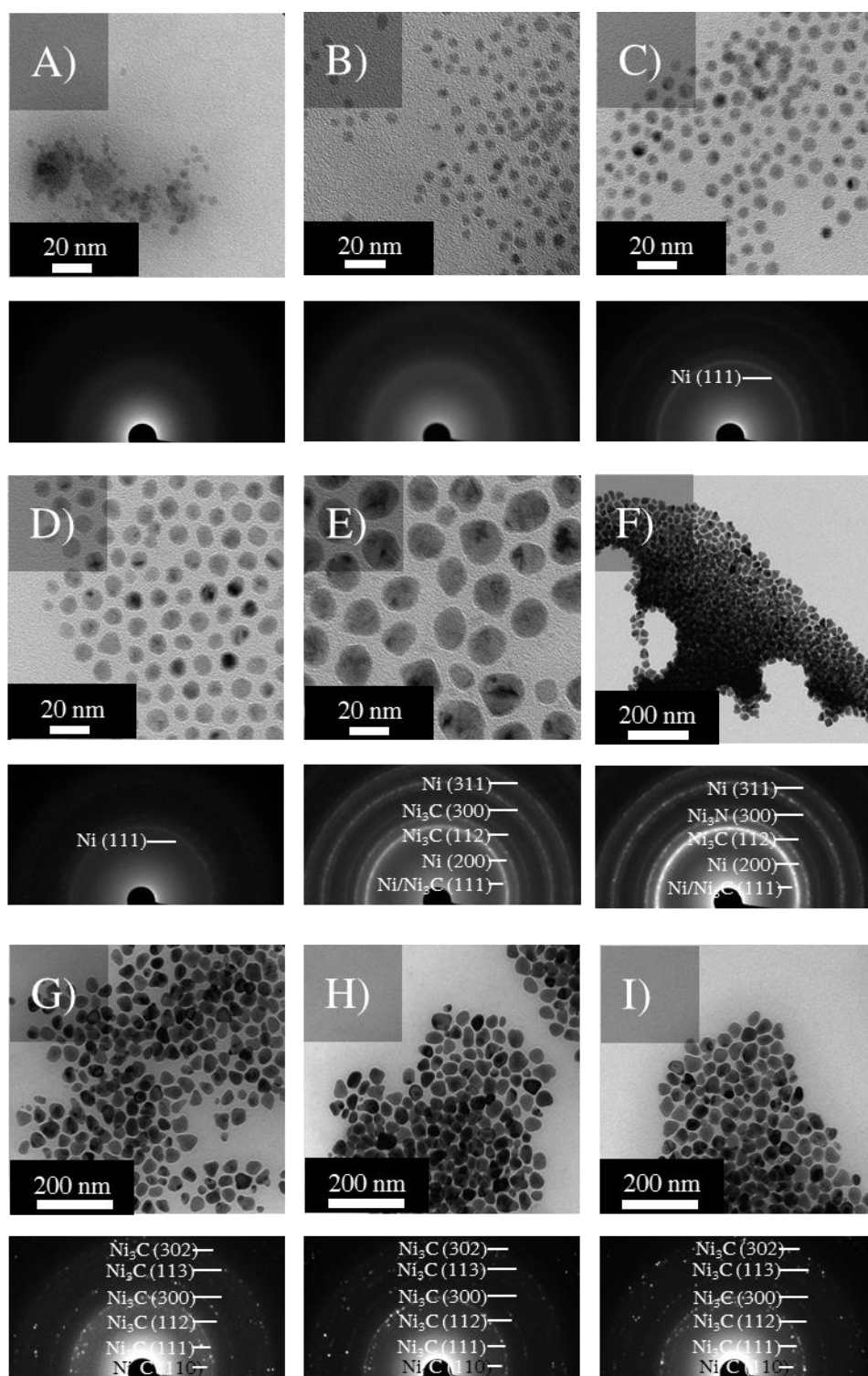


Figure 11: Growth of Ni/Ni<sub>3</sub>C nanoparticles after different growth times. (A: 3 min, B: 3 min 20 s C: 3 min 30 s D: 4 min; E: 4 min 30 s; F: 6 min; G: 10 min; H: 20 min, I: 40 min) with the corresponding SAED patterns below.

As time passes, the crystallinity increases and with the formation of  $\text{Ni}_3\text{C}$ , certain facets are preferred leading to an anisotropic growth of polyhedrons. The high surface to volume ratio dictates a high impact of the surface energy to the total free energy and therefore on the morphology of the nanoparticles. As particles are striving for a decrease in surface free energy, spherical particles are preferred in the beginning due to their minimum ratio of surface area to volume. The growth of nanoparticles was monitored by FT-IR after different growth times and is displayed in Figure 12.

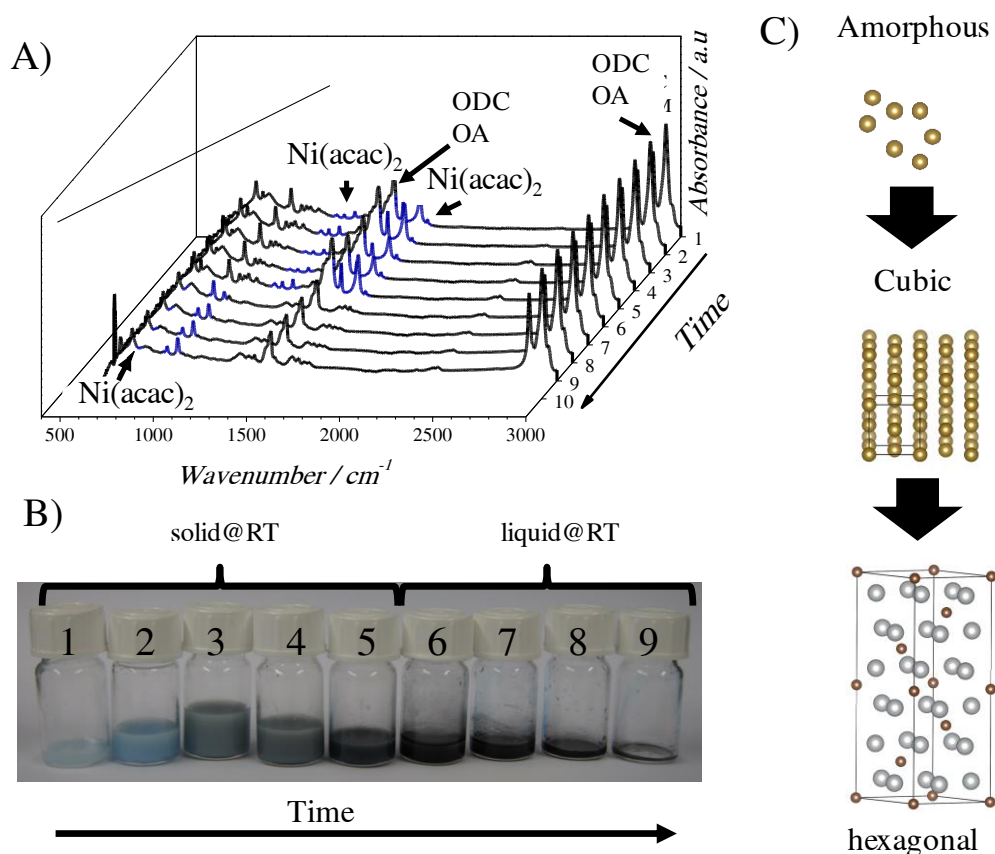


Figure 12: A) Ex-situ FT-IR spectrum of  $\text{Ni}_3\text{C}$  growth after 1) 1 min 10s, 2) 1 min 40 s, 3) 3 min 30 s, 4) 4 min, 5) 4 min 30 s, 6) 5 min 10 s, 7) 5 min 50 s, 8) 6 min 40 s, 9) 7 min 10 s and B) the corresponding macroscopic images of the samples. C) Schematic depiction of phase transformation from amorphous materials over cubic nickel to hexagonal  $\text{Ni}_3\text{C}$  during synthesis.

In the beginning, the characteristic peaks from oleylamine, 1-octadecene and acetylacetonate were observed. With progressing time, peaks at  $1,600\text{ cm}^{-1}$  ( $\nu(\text{C}=\text{O})$ ),

$\nu(\text{C}=\text{C})$ ),  $1,508\text{ cm}^{-1}$  ( $\nu(\text{C}=\text{O})$ ,  $\delta(\text{CH})$ )  $1,420\text{ cm}^{-1}$  ( $\delta(\text{CH}_3)$ ),  $1,263\text{ cm}^{-1}$  ( $\nu(\text{C}-\text{C})$ ,  $\nu(\text{C}-\text{CH}_3)$ ) and  $1,154\text{ cm}^{-1}$  ( $\delta(\text{CH}_3)_{\text{rock}}$ ) that are characteristic for  $\text{Ni}(\text{acac})_2$  disappear presumably accompanied by  $\text{CO}_2$  evolution.[122, 123]  $\text{NH}_2$  bending modes at  $910\text{ cm}^{-1}$  and  $990\text{ cm}^{-1}$  indicative for primary amines were observed throughout the entire growth. However, a shift in vibrational energy due to binding of oleylamine to  $\text{Ni}_3\text{C}$  nanoparticles were not observed, presumably due to excess of oleylamine in solution and the associated superimposition. The peak at  $720\text{ cm}^{-1}$  was assigned to  $\text{CH}_2$  rocking from oleylamine and 1-octadecene. Bands at  $2,854\text{ cm}^{-1}$  and  $2,929\text{ cm}^{-1}$  are characteristic for symmetric and asymmetric C-H vibrational modes from oleylamine and 1-octadecene.[124] Figure 12 shows the macroscopic changes of the samples where oleylamine, 1-octadecene and  $\text{Ni}(\text{acac})_2$  form rather a solid while with subsequent time,  $\text{Ni}(\text{acac})_2$  decomposes and the formation of a dark liquid can be observed, thus, indicating colloidal particle formation. Through the monitoring of  $\text{Ni}(\text{acac})_2$  decomposition by FT-IR and the subsequent formation of amorphous nickel particles (TEM), the foundation for further understanding of the growth process has been laid. From TEM, the time dependency on the particle size can be determined shown in Figure 13. The diameter increases rapidly with  $\sim 6\text{ nm min}^{-1}$  at an early stage in a reaction controlled manner and reaches a plateau at around ten minutes due to decreased monomer concentration and stabilization of bigger nanoparticles. Contrast darkening with time suggests a 3-dimensional growth where each nanoparticle is increasing in diameter (Figure 11). The standard deviation (from  $\sim 50$  nanoparticles) is considered relatively small in the beginning whereas increased standard deviation can be observed as time proceeds (Figure 11). After ten minutes, the anisotropic growth leads to elongated nanoparticles with average dimensions of  $40\text{ nm}$  in length and  $30\text{ nm}$  in width and multiple facets.

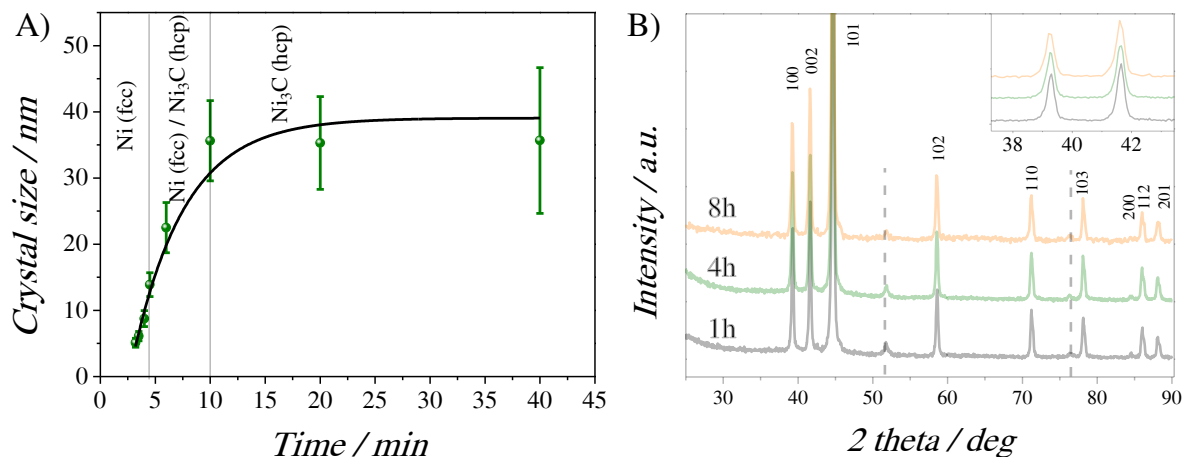


Figure 13: A) Particle size dependency on the growth time and the formed phases. The nanoparticle size was determined with “ImageJ” from TEM images and the curve was fitted asymptotically converging to a nanoparticle size of  $\sim 39$  nm. The time was set to zero when heating from  $120$  °C was started in a temperature ramping fashion. B) PXRD of Ni<sub>3</sub>C formed after 1 h, 4 h and 8 h. The inset shows the enlarged region of the 100 and 002 reflections indicating no change/carbon incorporation during the prolonged heating time. The dashed line indicates reflections from pristine, unreacted nickel (ICDD: 04-008-845).

The position of the reflections in the PXRD pattern coincide well with reference peaks from Ni<sub>3</sub>C (Figure 13). After one hour, the particle size obtained from Scherrer’s equation corresponded to  $\sim 30$  nm (d(100), d(002)). Despite the slightly smaller crystallite size obtained from PXRD, the compendious results indicate monocrystalline nanoparticles. It is not uncommon that smaller crystallite sizes are obtained from PXRD since other parameters such as instrumental factors, microstrain or defects play not negligible roles in peak broadening. Extended reaction time did not lead to an increase in particle size (TEM) and a shift in reflections (PXRD) speaking for successful stabilization of Ni<sub>3</sub>C by oleylamine and inhibited carbon incorporation with time.

However, another question still to be answered is why these particles are relatively small and homogeneous even though a burst of nucleation is not deliberately evoked. Kwon and Hyeon reported decomposition of Fe(CO)<sub>5</sub> to atomic Fe(0) in the presence of oleic acid and its subsequent stabilization through iron complexes.[125] Presumably, the same mechanism applies here. Ni(0) was stabilized through oleylamine ligands deferring the nucleation event. At higher temperatures, burst

nucleation led to relatively small nanoparticles and due to sterically stabilizing oleylamine linkers to a homogeneous size distribution. The burst nucleation can be compared to the hot injection method described first by Murray, Norris, and Bawendi in their breakthrough work towards nearly monodispersed nanoparticles.[126] The interaction of ligands with metal atoms after reduction is therefore crucial to form monodispersed small particles. Hereby, oleylamine is considered as hard base and atomic nickel as soft acid according to *Pearson's hard and soft acids and bases concept*. [127] Therefore, soft bases such as phosphines, thiols or arsenides should lead to better stabilization and therefore to smaller particle size. Consequently, an adapted synthesis strategy was used with trioctylphosphine (TOP) as soft base in the starting material. In this context, it has been shown before that TOP acts as phosphorous precursor for the transformation of pristine metals into transition metal phosphides.[128, 129] However, no conclusions about the ligand influence on the phosphide or carbide particle size have been drawn by now. The ratio of oleylamine and 1-octadecene was kept constant along with the Ni(acac)<sub>2</sub> amount ensuring comparable results. The resulting TEM and PXRD patterns are displayed in Figure 14. Similar to Ni<sub>3</sub>C where nickel is formed first followed by the transformation into nickel carbide, TOP acts as phosphorous source that can stabilize and react with formed nickel nanoparticles. Indeed, small nanoparticles of Ni<sub>2</sub>P were observed after 1 h at 320 °C in the size range of 10.7 nm ± 1.8 nm consistent with the proposed reaction mechanism. When Scherrer's equation is applied on the 2 $\bar{1}0$  and 201 *Bragg reflection*, a smaller mean crystallite size of 7.5 nm compared to TEM was obtained. As elaborated before, it is not uncommon to obtain smaller crystallite sizes by PXRD in comparison to TEM, still suggesting monocrystalline nanoparticles.

During synthesis, elemental nickel is formed first, followed by void formation due to quicker, outwards directed core diffusion than inward diffusion of reactive material. This effect is known as *Kirkendall effect*. [128, 130, 131] In Ni<sub>3</sub>C, this effect was not

observed speaking for a  $\text{Ni}_3\text{C}/\text{C}$  diffusion rate smaller or equal to pristine nickel. A schematic illustration of the growth mechanism and the influence of the ligands can be found in Figure 14. Further studies have to reveal whether other soft bases such as thiols or arsenides lead to the same observed effect of size reduction and whether nickel sulfides, selenides or arsenides can be formed in the same manner.

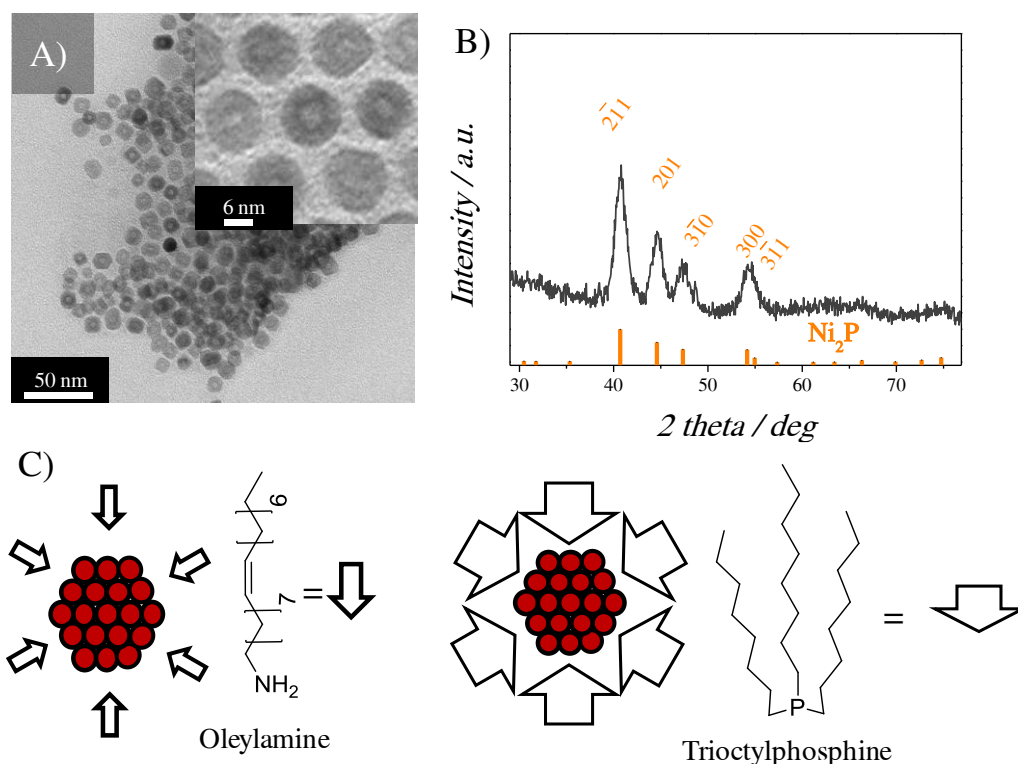


Figure 14: A) SEM images of  $\text{Ni}_2\text{P}$  nanoparticles obtained after 1 h at 320 °C and B) the corresponding PXRD pattern with indicated  $\text{Ni}_2\text{P}$  reflections as reference ( $\text{Ni}_2\text{P}$ : ICDD: 04-005-5698). C) Schematic illustration of nickel (red) surrounded by oleylamine and trioctylphosphine ligands. The large arrows display the proposed strong interaction of TOP with the nanoparticles.

### 4.3 $\text{Ni}_3\text{C}$ and its water reduction abilities

$\text{Ni}_3\text{C}$  is – similarly to  $\text{Ni}_3\text{N}$  – not well explored towards the hydrogen evolution reaction. Concurrent to the here described work, Guo and coworkers reported  $\text{Ni}_3\text{C}$  embedded into graphene nanoribbons with promising catalytic behavior towards the HER in acidic solution.[104] However, what was not mentioned is the increased

oxidation aspiration of Ni<sub>3</sub>C in comparison to nickel which is expressed in dissolution in acidic environment when no load is applied. For instance, the standard electrode potential for the reaction  $Ni^{2+} + 2e^- \rightleftharpoons Ni(s)$  comes to -0.25 V. For the reaction  $3 Ni^{2+} + 6e^- + C \rightleftharpoons Ni_3C(s)$ , an equilibrium potential of -0.34 V can be attained.[132] Therefore, when only taking thermodynamics into account, Ni<sub>3</sub>C can be oxidized much easier compared to its pristine metal congener. It is hereby possible that Raney related coatings (washing out of aluminum/carbon/sulfur) evolve as observed for Ni<sub>3</sub>S<sub>2</sub> in acidic environment accounting for the observed activity.[62, 133, 134, 135] In the same manner, Ni<sub>3</sub>C is presumably oxidized first, when no load is applied followed by the dissolution of its ions. At sufficient negative potentials, the reduction of Ni<sup>2+</sup> ions takes place to form a rough and uneven Ni(0) surface.

Nevertheless, as results on the hydrogen evolution performance of Ni<sub>3</sub>C nanoparticles in alkaline environment are still pending, all measurements were performed in alkaline solutions (1 M KOH). Furthermore, surrounding carbon layers may block catalytically active sites reducing the activity of Ni<sub>3</sub>C as observed in the previous chapter for Mn/Ni@NDC. Therefore, detailed pre- and post-catalytic characterization of Ni<sub>3</sub>C along with kinetic measurements are presented. The first step encloses the choice of support material since inadequate materials could favor transport limitation, instability or contamination. Initially, Ni<sub>3</sub>C nanoparticles were dispersed in hexane, drop casted onto a pristine nickel substrate and heated 4 h at 350 °C in H<sub>2</sub>/Argon (5/95) in order to remove surrounding ligands. However, weak bonding to the substrate and consequent detachment during HER measurement was experienced. In the end, high temperature treated carbon fibres provided enough Ni<sub>3</sub>C anchor sites accompanied with high conductivity, strength, surface area and stability towards the hydrogen evolution reaction. For the sake of simplicity, Ni<sub>3</sub>C on carbon paper will be denominated as Ni<sub>3</sub>C@C. The resulting SEM image of loaded Ni<sub>3</sub>C@C is shown in Figure 15 indicating homogeneous coverage. The surrounding

oleylamine ligands were removed in H<sub>2</sub>/Argon (5/95) at 350 °C for 4 h. The removal of oleylamine was verified by FT-IR. Figure 15 shows the FT-IR spectrum of Ni<sub>3</sub>C@C before and after H<sub>2</sub>/Ar treatment and pristine carbon paper as reference. Hereby, characteristic bands of oleylamine were found after drop-casting of Ni<sub>3</sub>C on carbon paper. In the range of 2,850-2,960 cm<sup>-1</sup>, symmetric and asymmetric C-H stretching vibrations were found.

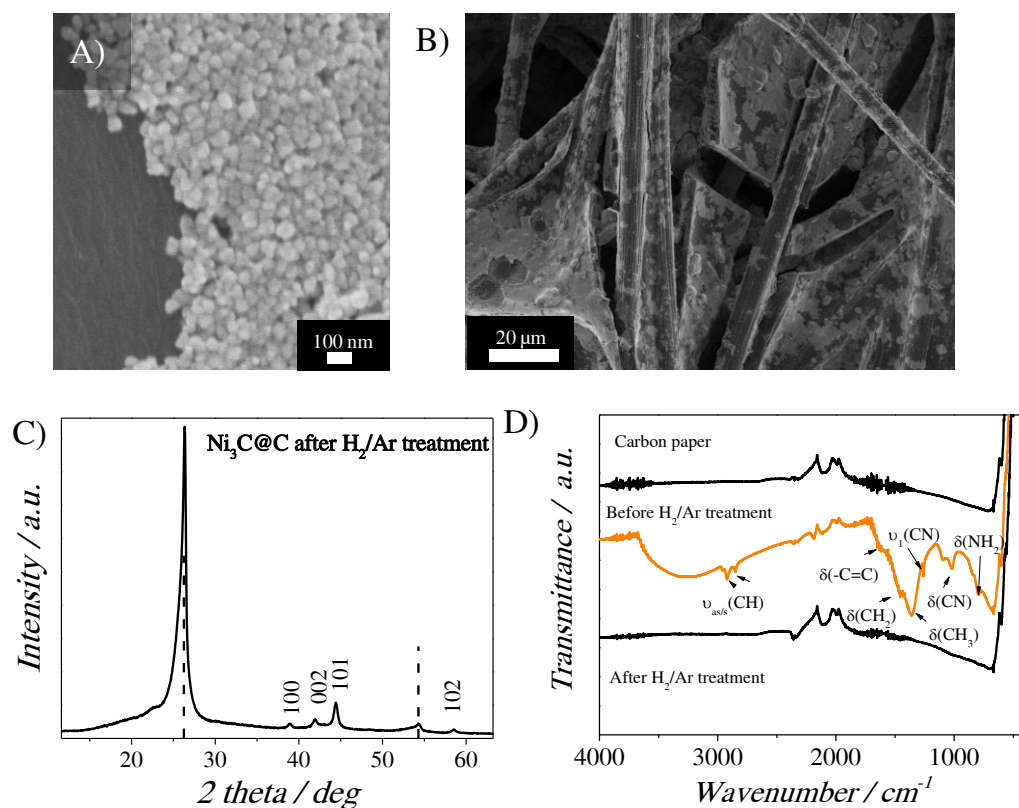


Figure 15: A) High and B) low magnification SEM images of Ni<sub>3</sub>C on carbon paper with loading of 5.6 mg cm<sup>-2</sup>. The particle size corresponds well to the TEM determined one. C) PXRD confirms that Ni<sub>3</sub>C is still present after H<sub>2</sub>/Ar treatment at 350 °C. The characteristic reflections from Ni<sub>3</sub>C are indicated. The dashed lines represent reflections from carbon paper. D) FT-IR spectrum of pristine carbon paper, carbon paper loaded with oleylamine capped Ni<sub>3</sub>C nanoparticles and after H<sub>2</sub>/Ar treatment. About the bands at 2,100 cm<sup>-2</sup> from carbon paper can be only speculated. Presumably, carbon is bound in a double or triple bonding fashion to O/N characteristic for this wavenumber range.

The vibrations at 1,450 cm<sup>-1</sup> were ascribed to CH<sub>2</sub> bending vibrations, the one at 1,650 cm<sup>-1</sup> to -C=C deformation. At 1,370 cm<sup>-1</sup>, symmetric deformation from CH<sub>3</sub> can be detected. The band at 1,260 cm<sup>-1</sup> was assigned to C-N vibrational modes. As the

H<sub>2</sub>/Argon atmosphere is highly reductive, one could argue that Ni<sub>3</sub>C might be reduced to Ni(0) at 350 °C. However, the not occurring reduction of Ni<sub>3</sub>C to pristine nickel was excluded by PXRD where only Ni<sub>3</sub>C reflections were observed after treatment (Figure 15).

Figure 16 displays the current voltage characteristics of Ni<sub>3</sub>C in 1 M KOH on carbon paper with Ni<sub>3</sub>C loading of 5.6 mg cm<sup>-2</sup>. In order to reduce capacitive currents, chronoamperometric measurements were performed holding a certain potential for 60 s. By moving the potential in 10 mV steps towards more negative values (0.07 V – -0.2 V vs. RHE) the corresponding current voltage curve in Figure 16 was obtained. Ni<sub>3</sub>C shows high activity towards the hydrogen evolution in strong alkaline medium with current densities close to 100 mA cm<sup>-2</sup> with a necessary overpotential of ~0.2 V. The *Tafel slope* of ~116 mV dec<sup>-1</sup> at moderate currents suggests a *Volmer-Heyrovski* or *Volmer-Tafel* mechanism whereby the first discharging step is rate determining.[136] At higher current densities, a larger *Tafel slope* was experienced presumably due to mass transport limitations or nucleation/accumulation of hydrogen bubbles on the electrode surface.

High activity is only useful in combination with long-term durability. Therefore, long-term stability testing was performed keeping the current density constant at -10 mA cm<sup>-2</sup> for 20 h (Figure 16). In contrast to directly modified support as in Ni<sub>5</sub>P<sub>4</sub> or Ni<sub>3</sub>N (cf. chapter 5), higher degree of destabilization during the 20 h test was observed. The reasons may lie in nanoparticle agglomeration or loss of active surface area due to higher level of detachment from the support (Figure 16). It is believed that by further control of nanoparticle distribution and stabilization, Ni<sub>3</sub>C will increase in stability and performance.

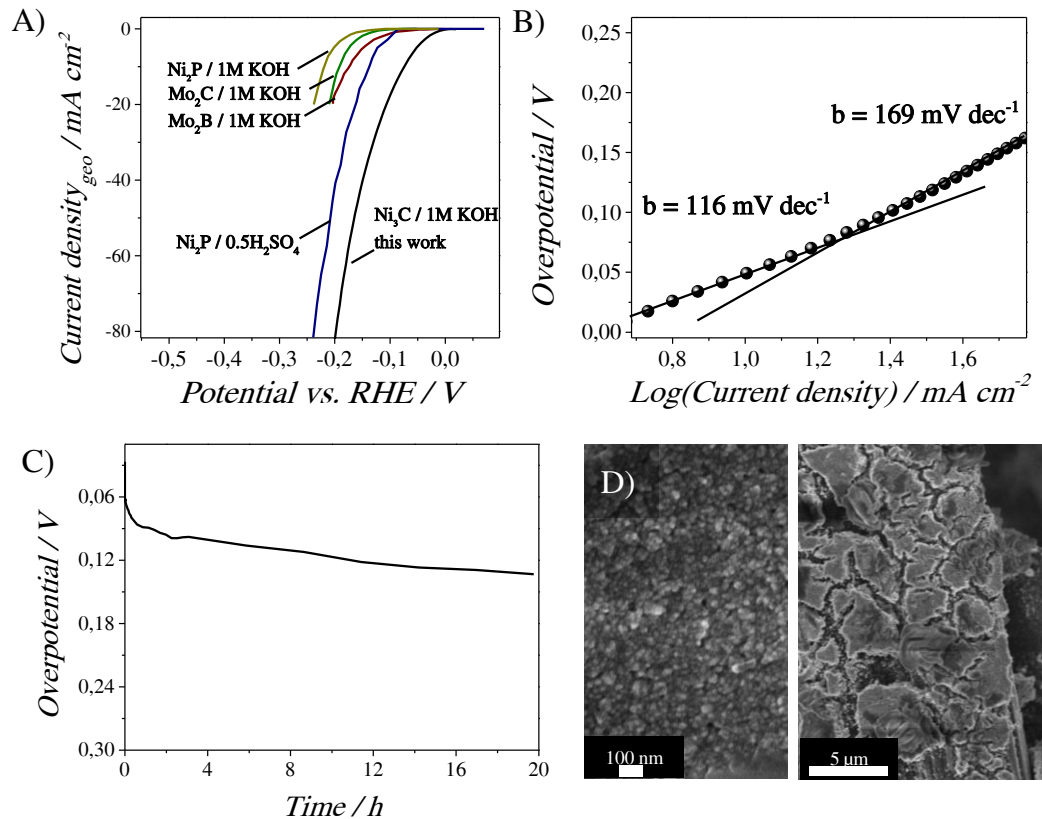


Figure 16: A) Current voltage characteristics of Ni<sub>3</sub>C on carbon paper in 1 M KOH, rotating the working electrode at 2,000 rpm compared to selected state-of-the-art catalysts. Ni<sub>2</sub>P (0.5 H<sub>2</sub>SO<sub>4</sub>)[137], Mo<sub>2</sub>C[138], Mo<sub>2</sub>B[138], Ni<sub>2</sub>P[129] (1 M KOH). B) Tafel analysis of Ni<sub>3</sub>C with two distinct Tafel slopes. C) Long-term stability at -10 mA cm<sup>-2</sup> over 20 h in 1 M KOH, rotating the working electrode at 2,000 rpm and the corresponding post-catalytic recorded SEM images with high and low magnification (D).

#### 4.4 Summary

The growth of Ni<sub>3</sub>C nanoparticles was thoroughly examined. Hereby, the growth proceeds through the formation of amorphous nickel, followed by the incorporation of carbon into the structure resulting in the formation of crystalline, hexagonal Ni<sub>3</sub>C nanoparticles. In this manner, the size could be accurately controlled and reaction time dependent phases were obtained. Small nanoparticles were attained by stabilization of nickel atoms by oleylamine and trioctylphosphine ligands, delaying nucleation. Subsequently, these nickel nanoparticles are transformed into the corresponding nickel phosphides and carbides. As high electrocatalytic performance

from its isostructural counterpart,  $\text{Ni}_3\text{N}$ , was theoretically predicted and experimentally demonstrated (cf. chapter 6), similar activity was expected.

Indeed, by choosing an adequate support material, high electrocatalytic performance was achieved with current densities over  $100 \text{ mA cm}^{-2}$  at overpotentials close to 0.2 V. Furthermore, the temperature ramping synthesis strategy offers more applicability for industrial implantation, thus, reducing potential hazards and less cautious handling is mandatory. Furthermore, the fairly large *Tafel slope* of  $116 \text{ mV dec}^{-1}$  offers applicability in the field of photoelectrolysis where smaller currents densities ( $10\text{-}20 \text{ mA cm}^{-2}$ ) are utilized and a smaller logarithmic improvement of current density is of less consequences than in pure electrolyzers with high current densities. The  $\text{Ni}_3\text{C}$  nanoparticle size can be accurately tailored and the amount of active catalyst adjusted using less concentrated dispersions. This approach therefore offers the physical prerequisites for further use in photocatalysis. As the used synthesis strategy is derived in analogy from semiconductor quantum dots synthesis[139], combination of both, the photosensitizer and (co-)catalyst could be feasible: a quantum dot – nanoparticle interplay. The linkage could be provided by e.g. conductive, conjugated thiol linkers.[140] However, this idea is still in its infancy. Nevertheless, current research is ongoing combining  $\text{Ni}_3\text{C}$  nanoparticles with low-cost semiconductors such as carbon nitride[141] to convert sunlight directly into practical energy forms.

# 5 Evolution of nanostructured Ni<sub>5</sub>P<sub>4</sub> and its use as cost-efficient bifunctional electrocatalyst towards the HER and OER

---

## 5.1 Background

In the previous chapter, the growth and synthesis of nickel carbide were elaborated with notable performance towards the HER. However, the preparation of the final catalyst comprised several steps beginning with the catalyst preparation, the anchoring onto existing support and removal of stabilizers. In the following, the support material was modified directly, making multi-step preparation methods redundant. Moreover, this chapter is dedicated to the introduction of a new type of hydrogen and oxygen evolution catalyst, namely Ni<sub>5</sub>P<sub>4</sub>. Additionally, light will be shed onto the formation mechanism of the protruding nanoplate morphology. The influence of heating time and spatial confinement during synthesis will be explored.

The first studies of metal phosphides as catalysts for hydrogenation reactions are dating back to 1980 reported by Nozaki.[142, 143] Thenceforth, metal phosphides have witnessed an abiding rise of attention not only in hydrogenation reactions but also as HER catalyst with high stability in acidic and basic solution.[48] Amid them, FeP[144, 145], Co<sub>2</sub>P[146], CoP[147], Ni<sub>2</sub>P[129, 148], Ni<sub>12</sub>P<sub>5</sub>[149] and Mo<sub>3</sub>P[150] belong to the best known HER catalysts with low onset potentials and fast reaction kinetics. By combining metallic and ceramic properties, metal-rich phosphides become excellent materials for high performance electrodes. For instance, metal-rich phosphides show low electrical resistivity, high thermal conductivity, high melting

---

points and high chemical stability.[151, 152] Due to the prerequisite of high electric conductivity, only metal-rich and monophosphides ( $M/P \geq 1$ ) have found their way into the field of electrocatalysis. Furthermore, it has been found that corrosion resistance scales directly with the amount of phosphorous ( $Ni_2P > Ni_{12}P_5$ ) inside the structure.[153] Therefore, nickel phosphides with high phosphorous content are auspicious while keeping its metallic conductivity. Most of the aforementioned synthesis routes of metal (Fe, Co, Mo, Ni) phosphides result in colloidal nanoparticles, synthesized e.g. by bottom up approaches. Concurrent to the described work here,  $Ni_5P_4$  nanoparticles have been reported as HER catalyst.[154] The advantages of these synthesis strategies are their high controllability towards monodispersity and small crystal sizes (cf. chapter 4). However, these catalysts entail disadvantages such as residual templates, uncontrolled agglomeration, high series resistance, and facile oxidation. Heterogeneity and poor dispersibility of synthesized particles foster non-reproducible results. The use of stabilizers potentially results in blocking of the active surface area. In addition, polymer binders (e.g. Nafion<sup>®</sup>) are frequently present during catalytic testing leading to possible blockage of active sites or diffusion pathways and high serial resistance, thereby reducing the catalysts apparent activity.[155, 156] Following these cornerstones, a straightforward, binder and ligand free synthesis of nickel phosphide ( $Ni_5P_4$ ) on nickel substrate was introduced, thus, avoiding impurities through templating. By directly modifying the support material, strong mechanical adhesion and electrical conductivity were ensured with potentially less serial resistance.[157, 158] The modified support has high application potential in e.g. electrolyzers, electrodes in solar cells or artificial leaves.

## **5.2 Synthesis, growth and characterization of nickel phosphide**

Other groups also recognized the potential of modifying the support directly to form  $Ni_2P$ [137, 159],  $CoP$ [49, 160, 161] or  $NiO$ [162] which have then been applied in

---

catalysis and as supercapacitors. According to the phase diagram of nickel and phosphorous, eight different nickel phosphides exist, ranging from phosphorous to metal-rich:  $\text{NiP}_3$ ,  $\text{NiP}_2$ ,  $\text{NiP}$ ,  $\text{Ni}_5\text{P}_4$ ,  $\text{Ni}_2\text{P}$ ,  $\text{Ni}_{12}\text{P}_5$ ,  $\text{Ni}_5\text{P}_2$ ,  $\text{Ni}_3\text{P}$ . [163] The difficulty herein persists in obtaining the desired phase despite non-stoichiometric reaction partners. [164] Even though only a handful of synthesis routes towards  $\text{Ni}_5\text{P}_4$  exist, researchers have circumvented the problem making use of eutectic mixtures at high temperatures and long heating times (e.g.  $> 800\text{ }^\circ\text{C}$ , 20 days). [164, 165, 166] In this work, a more forthright preparation strategy was chosen by direct phosphidation of pristine nickel at  $550\text{ }^\circ\text{C}$  for one hour resulting in a layered structure with  $\text{Ni}_5\text{P}_4$  plates protruding from the surface.

The evolution of nickel phosphide on nickel foil was monitored for different growth periods by keeping the temperature constant at  $550\text{ }^\circ\text{C}$  as displayed in Figure 17. The relatively low temperature was chosen in order to minimize phase diversity. The on-top lying phosphorous after synthesis was amorphous with no reflections (PXRD not shown here). In Figure 17 (A-C), the characteristic striation pattern from the fabrication process of nickel foil can be observed. During growth, the pattern vanished due to thickening of the phosphide film. The first step comprises the adsorption of phosphorus on the metal surface similar to metal oxide formation at high temperatures. As liquid eutectics are formed only over  $850\text{ }^\circ\text{C}$ , the reaction takes place in a classical contact conversion fashion. [165]

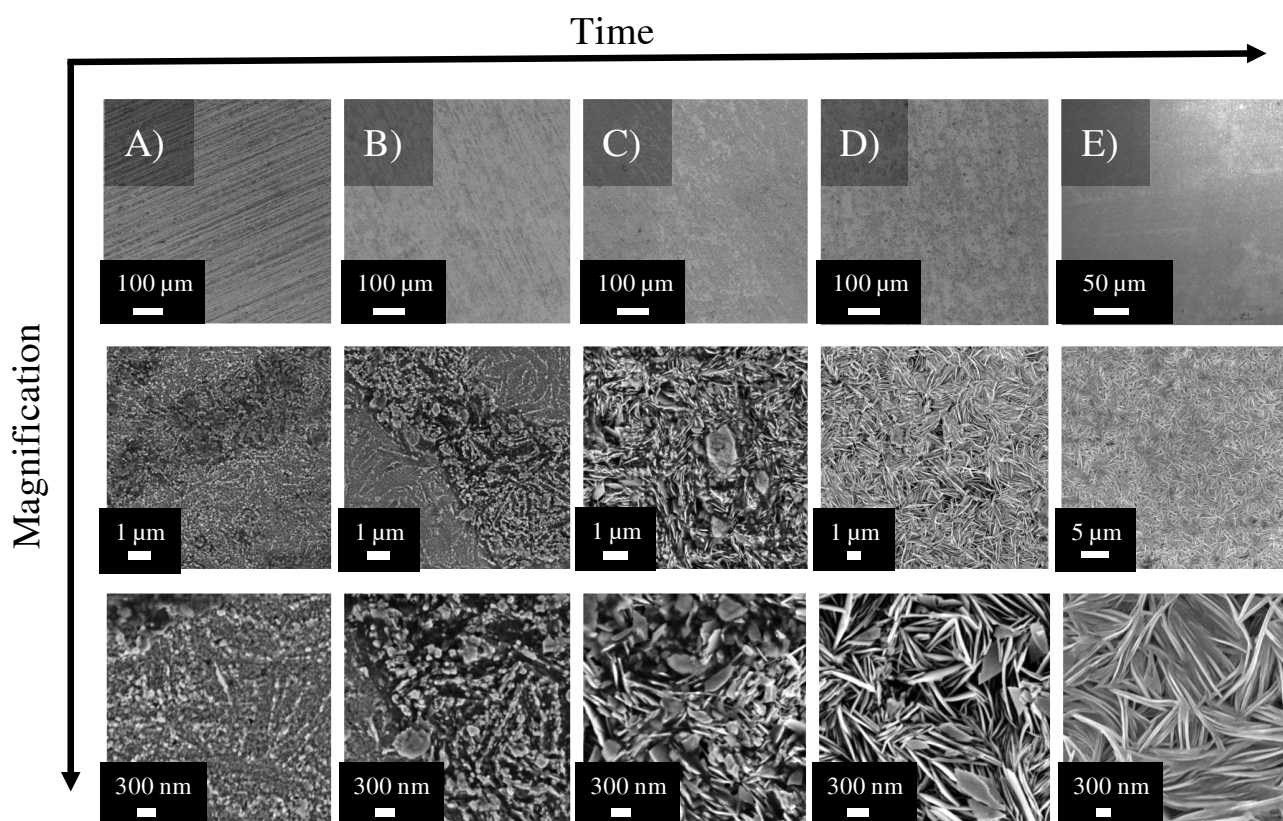


Figure 17: SEM morphology evolution of  $\text{Ni}_x\text{P}_y$  with respect to growth time. A) 7 min, B) 8 min, C) 8 min 30 s, D) 9 min and E) 12 min.

Presumably, the initial step encompasses the formation of small amorphous nanoparticles acting as seed layer for the followed anisotropic crystal growth. During the early stage of growth, less ordered structures evolved minimizing their surface energy while after thirty minutes, preferential crystal growth was observed. The formation of nickel phosphide islands in the beginning of the reaction can be evaluated in Figure S11.

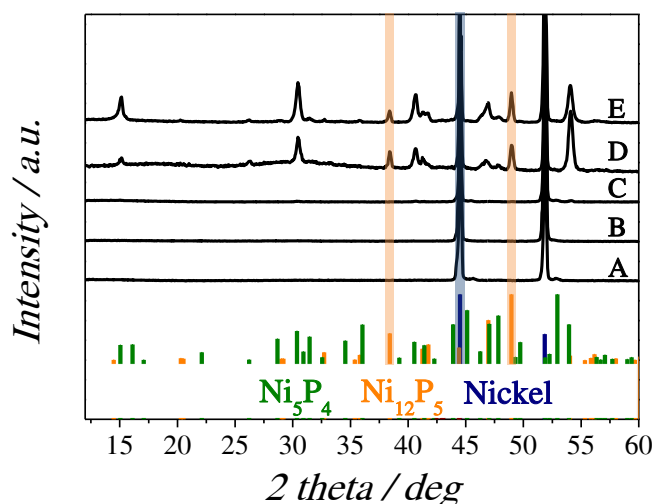


Figure 18: XRD analyses of  $Ni_xP_y$  after different growth intervals (A-E). The corresponding SEM images can be found in Figure 17.

The preferred growth direction led to fused nanoplates growing perpendicularly to the surface (C). From XRD analyses, cubic nickel reflections were observed in (A, B) from the nickel support (Figure 18). With prolonged time,  $Ni_5P_4$  reflections evolved (C) whereas pronounced  $Ni_5P_4$  and  $Ni_{12}P_5$  reflections were observed (D, E) towards the end of the time sequence. Attributable to concentration gradients present, nickel-rich  $Ni_{12}P_5$  (tetragonal) evolved close to the nickel interface during the isothermal reaction. Interestingly, the two other nickel-rich phosphide phases ( $Ni_3P$  and  $Ni_2P$ ) could not be observed in XRD. In literature, it has been shown that  $Ni_{12}P_5$  is kinetically preferred over  $Ni_2P$  which is in line with the here obtained results where  $Ni_2P$  was observed after nine hours (Figure S9).[167] Moreover, after nine hours, other nickel-poor phosphide species evolved speaking for densifying of the scale. After the first layers of nickel phosphide were formed, the crystallites grew most likely due to diffusion of phosphorus through the nickel phosphide layer. Thereby, it is theoretically possible that nickel ions can diffuse to the surface through e.g. lattice defects. However, due to the relatively low temperature used, this is unlikely as predicted by *Tammann's rule*. [168] As diffusion coefficients are increasing with temperature and even more rapidly when close to the melting point, diffusion of

nickel ( $M_p = 1450 \text{ }^\circ\text{C}$ ) would be only expected to happen close to  $1000 \text{ }^\circ\text{C}$  ( $\sim \frac{2}{3}$  of the melting point). However, it is noted that *Tammann's rule* only results from experimental observation and can differ for the given system. After one hour, exclusively  $\text{Ni}_5\text{P}_4$  reflections were detected from PXRD (Figure 19) with mean plate thicknesses of  $85 \pm 8.5 \text{ nm}$  (determination from SEM, Figure 19). The experimental and reference reflections coincide well but a preferentially orientated growth on the substrate leads to divergent reflection intensities compared to the reference pattern. The diffraction peaks from the  $(10\bar{1}0)$  plane are much more pronounced, indicating a preferential growth in  $[10\bar{1}0]$  direction. In contrast, reflections from the  $(0001)$  plane do almost not exist, indicative for a perpendicular orientation of the hexagons to the substrate as displayed in Figure 19. Presumably, the highly anisotropic unit cell of  $\text{Ni}_5\text{P}_4$  favors the platelet crystal shape. It is furthermore imaginable that the underlying nickel foil favors the epitaxial growth of nickel phosphide. EDX (five samples, same synthesis route) and ICP-OES analysis of the formed nickel phosphide layer coincide properly with the theoretical value of nickel to phosphorus ratio of  $\text{Ni}_5\text{P}_4$  ( $\text{Ni}/\text{P}_{\text{theo}} = 1.25$ ;  $\text{Ni}/\text{P}_{\text{ICP}} = 1.16$ ;  $\text{Ni}/\text{P}_{\text{EDX}} = 1.28 \pm 0.11$ ). Figure 19 represents a typical TEM image of a single crystal plate with polygonal shape with adjacent angles of  $120^\circ$  and  $60^\circ$ , respectively. The resulting SAED emphasizes the high degree of crystallinity and confirms the monocrystalline nature of the  $\text{Ni}_5\text{P}_4$  plate.

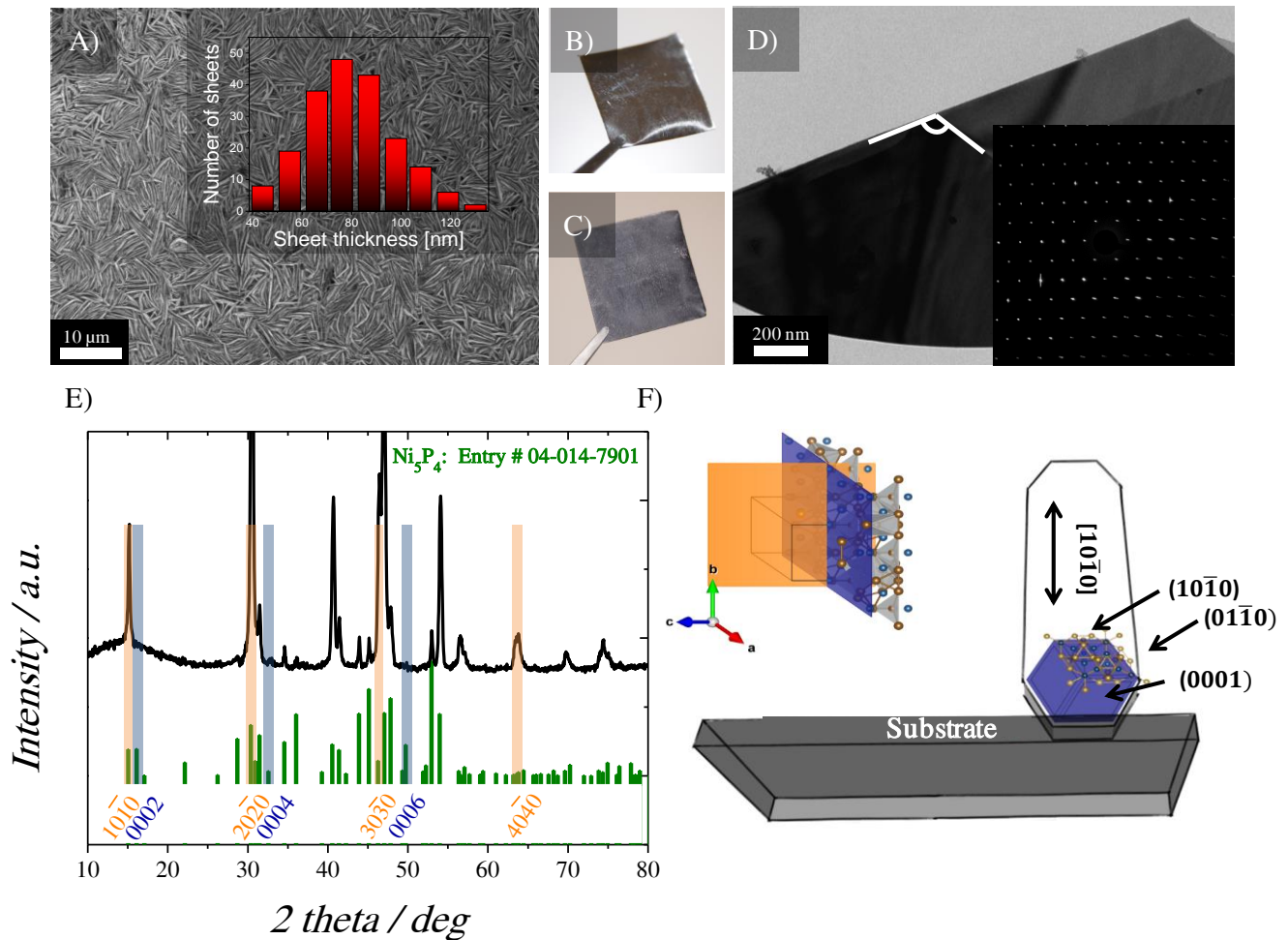


Figure 19: Characteristics of  $\text{Ni}_5\text{P}_4$  after one hour at  $550\text{ }^\circ\text{C}$ . A) SEM images of  $\text{Ni}_5\text{P}_4$  and the corresponding plate diameter distribution. Before synthesis (B), nickel foil exhibit typical metallic shine while after synthesis, (C) nickel phosphide appears rather black. TEM image (D) and the corresponding SAED of a monocrystalline  $\text{Ni}_5\text{P}_4$  plate scraped off the surface. E) Experimentally obtained PXRD pattern (black) and the corresponding reference pattern of  $\text{Ni}_5\text{P}_4$  (olive, ICDD 04-014-7901) with selected  $hkl$  values. F) Schematic illustration of hexagonal  $\text{Ni}_5\text{P}_4$  ( $P63mc$ ) with the hexagon forming plane (0001) (blue) with  $(10\bar{1}0)$  (orange) and  $(01\bar{1}0)$  planes standing upright forming the hexagonal side wall. The result is preferential growth of  $\text{Ni}_5\text{P}_4$  along the  $[10\bar{1}0]$  direction with the (0001) plane standing perpendicular to the substrate.

When investigating the cross-section of nickel phosphide grown after one hour by SEM/EDX, an underlying layer with higher Ni/P ratio in comparison to the upper layer can be observed (Figure 20). The underlying layer was proven by PXRD to be  $\text{Ni}_{12}\text{P}_5$  after removing the nickel phosphide film from nickel foil and grinding the powder thoroughly (Figure 20). The fact that mostly  $\text{Ni}_5\text{P}_4$  is formed speaks for a high diffusion rate through the material resulting in a poor protective scale. When increasing the reaction time to three hours and nine hours, respectively, phosphorus-rich phases appear ( $\text{NiP}_2$ ). The plate-like morphology observed from  $\text{Ni}_5\text{P}_4$  after nine hours was

still present but with much higher surface roughness (Figure 18). Presumably, the mechanism of phosphide growth resembles the one of nickel oxide at low temperatures where grain boundary diffusion has much higher contribution than lattice diffusion (cf. *Wagner's theory*).<sup>[169]</sup> Nevertheless, it is advised to keep the preparation  $\leq 1$  h in order to foster low amounts of crystal phases. As diffusion slows down with increasing scale thickness, multiple phases appear in form of phosphorous-rich phases when heated longer. The observed preferential growth speaks for high spatial competition where the crystals with hexagons arranged perpendicularly to the surface have improved chances to grow longer. The proposed mechanism of phosphide growth is displayed in Figure 21. In the beginning, the growth direction of the crystals is determined by the orientation of the seed crystals formed by early phosphidation. When alignment of the fast growing direction perpendicular to the substrate occurs, the growth is not hindered in this direction resulting in the observed nanoplate morphology. Differently oriented crystals are experiencing impingement into adjacent plates limiting their growth. Apparently, inward transport of molecular phosphorus is promoted, presumably due to the plate morphology where microchannels form along oriented grain boundaries during growth.

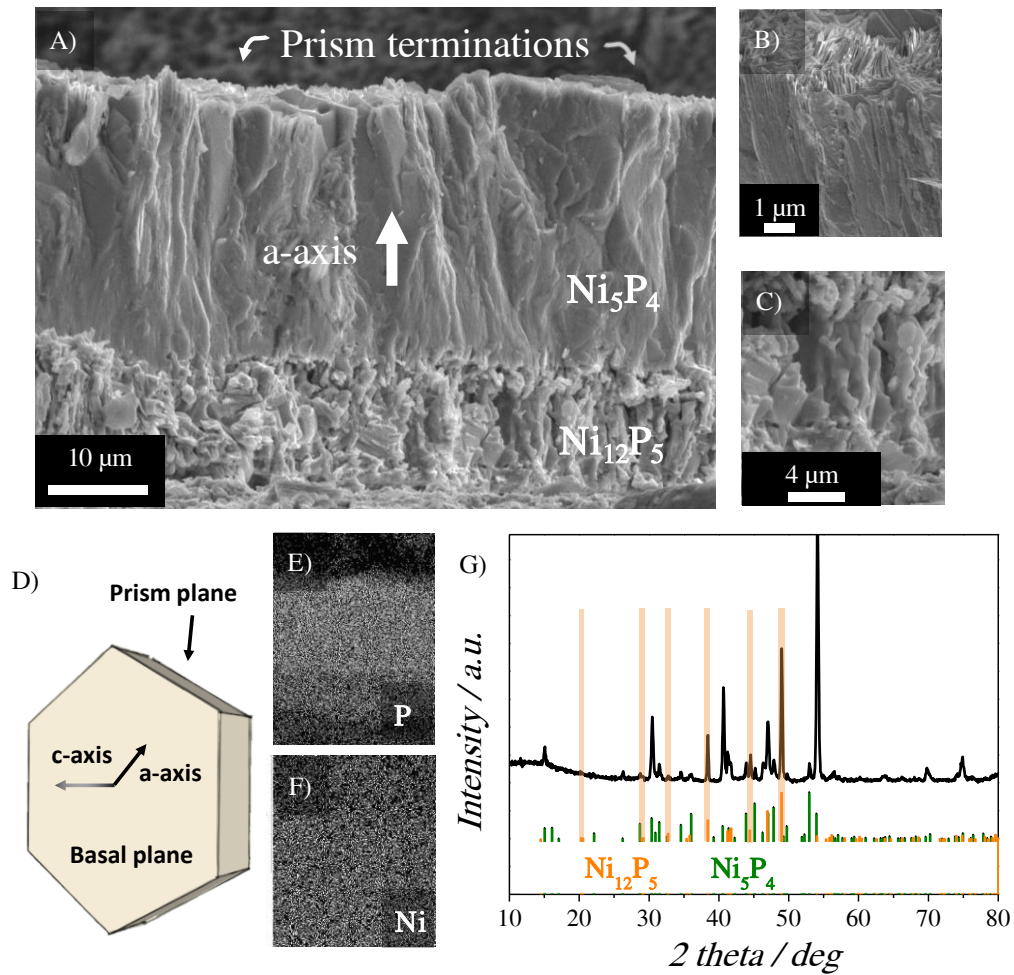


Figure 20: Cross-section SEM image of nickel phosphide after one hour reaction time in low (A) and high magnification mode (B, C). The indicated planes are illustrated in D. The corresponding phosphorus and nickel distribution of A obtained by EDX mapping (E, F). PXRD pattern of nickel phosphide after one hour reveals  $\text{Ni}_5\text{P}_4$  (olive) and  $\text{Ni}_{12}\text{P}_5$  reflections (orange) when the phosphide layer was removed from the underlying nickel foil and grinded thoroughly (G).

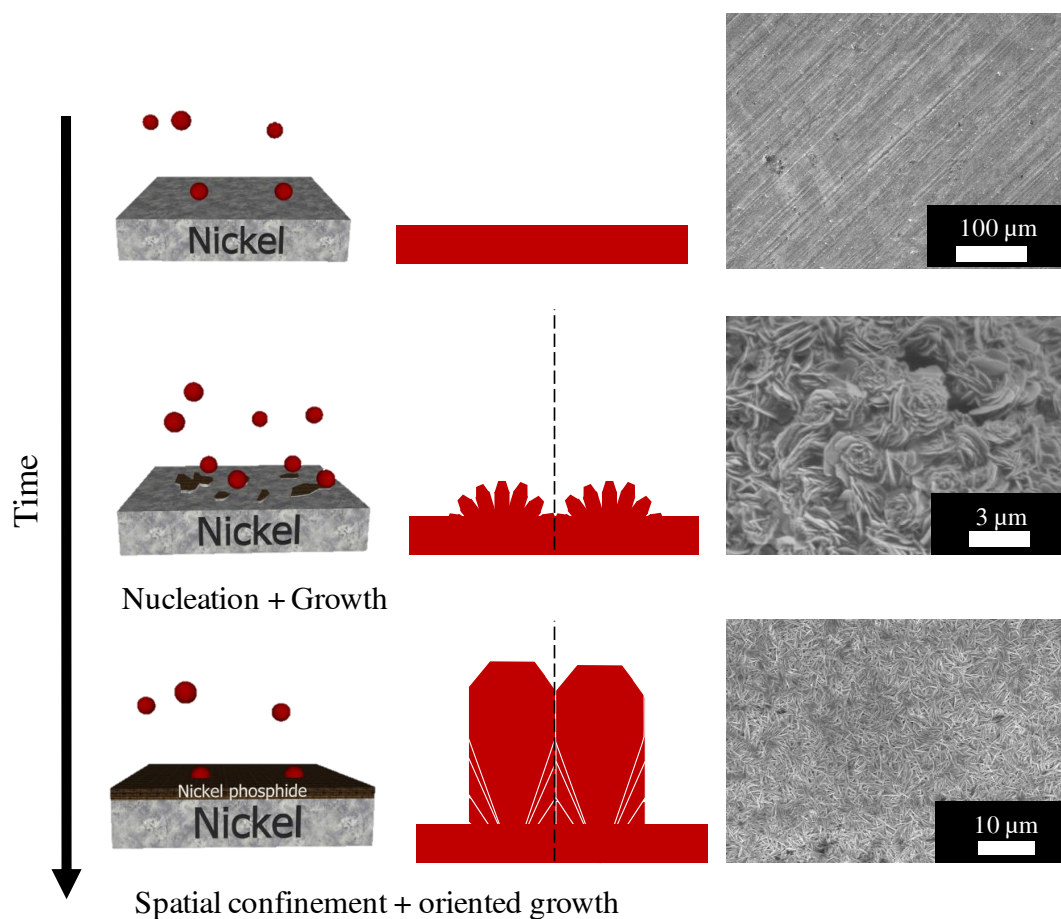


Figure 21: Simplified growth mechanism of  $Ni_5P_4$  nanoplates. In the beginning, phosphorus is reacting with pristine nickel foil. The anisotropic unit cell leads to growth of hexagons perpendicular to the surface. After random nucleation, the crystallites grow in different direction. As they are confined in space, the only available space is upwards. The resulting structure is a plate-like morphology. The first SEM image on the top displays pristine nickel foil. The second SEM image from the top is taken from phosphidation of nickel foam after 10 minutes. The third SEM image from the top displays phosphidation of nickel foil after 12 min.

As the showed results are based on bulk studies, *ex-situ* XPS analysis was undertaken in order to understand further the surface of the presented material. XPS measurements were realized by Sandra Krick-Calderón, Dr. Christian Papp and Prof. Dr. Hans-Peter Steinrück from the Friedrich-Alexander University Erlangen-Nürnberg and the full characterization can be found in [170]. XPS measurements indicate a signal at 857.5 eV along with a satellite peak at 862.6 eV in the characteristic Ni 2p region (Figure 22). After removal of impurities (1,000 K, 10 min) due to exposure to ambient conditions, a peak shift towards smaller binding energies was observed

(853.6 eV and 859.7 eV). The peak shift corresponds to the transformation of nickel phosphate to phosphidic/metallic nickel and is in line with previously reported Ni-P alloys with binding energies of 853.6 eV (phosphide) and 857.5 eV (phosphate).[171] It is noted that Ni(OH)<sub>2</sub> might be present displaying similar binding energies.[172] The results for the Ni 2P region are harmonious with the P 2p region with signals at 130.0 eV and 134.1 eV (Figure 22). The former is similar to black (130.45 eV) and red phosphorus (130.65 eV) and is assigned to nickel phosphide whereas the latter was assigned to nickel phosphate.[173] The P 2p signals comprise 2p<sub>1/2</sub> and 2p<sub>3/2</sub> doublets due to spin-orbit splitting. By heating in ultra-high vacuum, the phosphate layer was (partially) removed and nickel phosphide was identified which is in line with “bulk” techniques described before. The fact that both oxidation states of phosphorus are detected in the P 2p region but mainly phosphidic nickel in the Ni 2p region can be explained by the diverging information depth of both core levels. The P 2p is less sensitive to the surface compared to Ni 2p core levels due to the higher inelastic mean free path of the photoelectrons giving information also about the bulk material. It is noted that despite storing the samples in argon atmosphere, water, oxygen and other impurities could have interacted with the sample during transport or infiltration into the instrument.

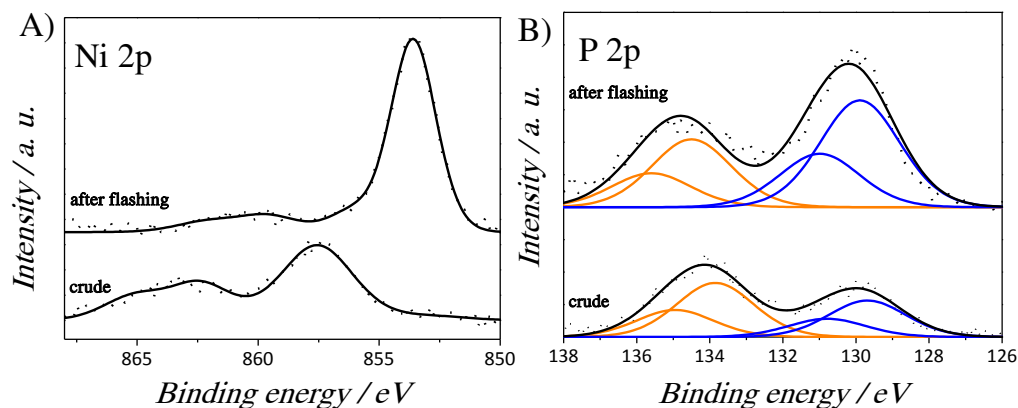


Figure 22: The experimentally obtained XPS Ni 2p (A) and P 2p (B) spectra of  $\text{Ni}_5\text{P}_4$  after one hour of phosphidation. The lower part of each spectrum shows the crude sample, the upper part the samples after flashing to 1,000 K in ultra-high vacuum.

### 5.3 Electrocatalytic water splitting reaction

$\text{Ni}_5\text{P}_4$  is of special interest for electrocatalysis due to the fact that no metal atoms are surrounded by phosphorus atoms resulting in free electron pathways through the material and metallic conductivity.[174] Furthermore, high stability was expected since a scaling relationship between phosphorous content and stability was found, namely, the higher the phosphorous content, the higher the stability.[153]

#### 5.3.1 Hydrogen evolution reaction

The electrocatalytic activity of  $\text{Ni}_5\text{P}_4$  in comparison to pristine nickel and platinum was investigated in a typical three electrode setup using a saturated calomel electrode (SCE) (in base) or Ag/AgCl (in acid) as reference electrode. A platinum wire served as counter electrode. When evaluating the catalytic activity of  $\text{Ni}_5\text{P}_4$  for the HER in 1 M KOH and 0.5 M  $\text{H}_2\text{SO}_4$ , the potential was swept from positive to negative (0.1 V to -0.5 V vs. RHE) using a scan rate of  $10 \text{ mV s}^{-1}$  (Figure 23).

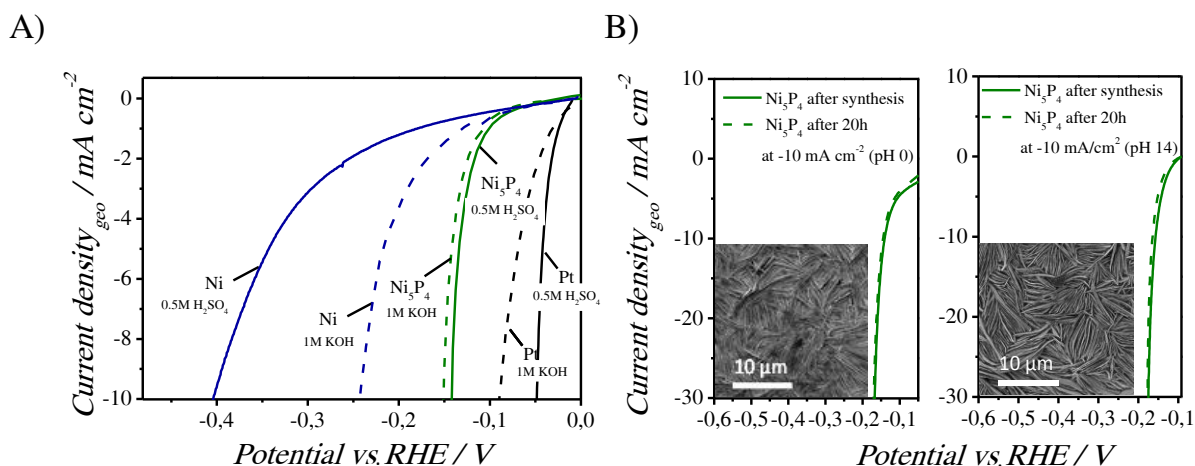


Figure 23: Linear sweep voltammograms in base (1 M KOH) and acid (0.5 M H<sub>2</sub>SO<sub>4</sub>) were recorded using a scan rate of 10 mV s<sup>-1</sup> rotating the working electrode at 2,000 rpm. b) LSV curves before and after long-term measurements at -10 mA cm<sup>-2</sup> for 20 h rotating the working electrode at 2,000 rpm using a scan rate of 5 mV s<sup>-1</sup>.

Ni<sub>5</sub>P<sub>4</sub> is hereby, not only gracious to the eye due to its symmetric nanoplate morphology but also highly active towards the hydrogen and oxygen evolution reaction. The catalytic activity of Ni<sub>5</sub>P<sub>4</sub> is much higher compared to pristine nickel with overpotentials of ~0.14 V in acid and ~0.15 V in base at -10 mA cm<sup>-2</sup>. Due to the direct correlation of hydrogen cost and lifetime of the catalyst, long-term stability tests were performed at pH 14 and pH 0, keeping the current density constant at -10 mA cm<sup>-2</sup> for 20 h. Thereby, linear sweep voltammetry curves and SEM images before and after reveal only minor changes in morphology and in catalytic activity (Figure 23). The corresponding chronopotentiometry data in base and in acid can be found in Figure S10. Especially in H<sub>2</sub>SO<sub>4</sub> where conventional catalysts as platinum are easily poisoned by sulfate ions, Ni<sub>5</sub>P<sub>4</sub> offers a new alternative as cathode material for acid electrolyzers.[175] A comparison of state-of-the-art catalysts for the HER can be found in Table S4. Interestingly, the catalytic performance in acid and base does not differ drastically. For platinum, different discharge mechanisms were found depending on the pH. In alkaline, discharge of water instead of H<sup>+</sup> in acid to form H<sub>ad</sub> was attributed as main reason for the reduced activity.[91] Another reason mentioned

in literature is alkali metal ion deposition on the surface in alkaline environment.[176, 177] For  $\text{Ni}_5\text{P}_4$ , comparable activity indicates that the first dissociation step in alkaline medium is not adding a further energy barrier. A more detailed reaction kinetic analysis follows. Furthermore, PXRD reveals no change of crystalline phases neither in alkaline nor in acidic solution after 20 h of stability testing (Figure 30). The advantage clearly lies in the corrosion resistance of  $\text{Ni}_5\text{P}_4$  in acidic medium as many transition metals are prone to dissolution indicated by their low standard electrode potential. The high phosphorus content is stabilizing the material against corrosion in acidic solution. By using nickel foam as substrate for the formation of nickel phosphide, the electrocatalytic performance could be even augmented reaching  $-200 \text{ mA cm}^{-2}$  below 200 mV revealing its high potential for real application purposes. Figure 24 (A-C) displays the SEM images of  $\text{Ni}_5\text{P}_4$  on high surface area nickel foam with homogeneous covering of  $\text{Ni}_5\text{P}_4$  in high and low magnification mode where single hexagonal plates can be observed growing perpendicular to the surface (C). As the bonding in binary phosphide materials is not pure metallic anymore, the malleable character of the erstwhile pristine nickel foam can be lost depending on the phosphidation degree and careful handling is mandatory.

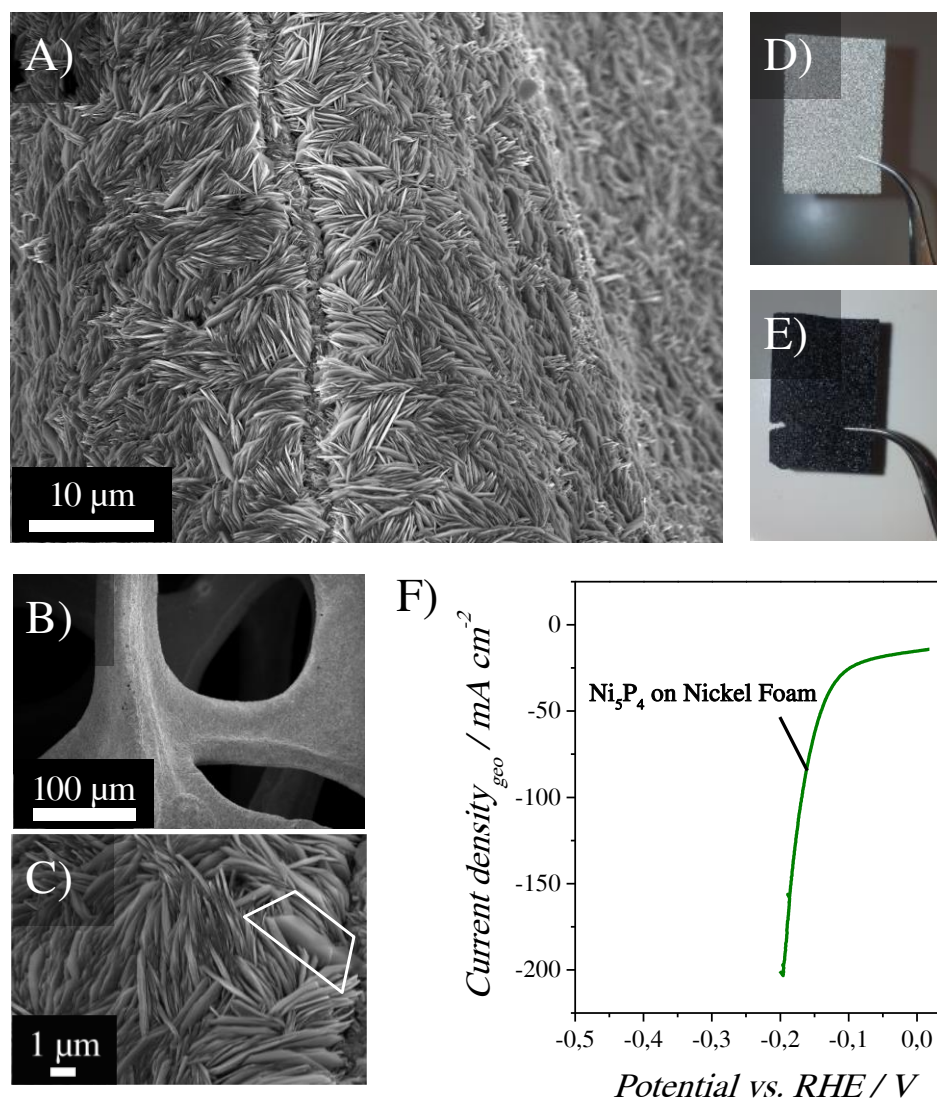


Figure 24: High and low magnification SEM-images of nickel foam directly modified with Ni<sub>5</sub>P<sub>4</sub> (A, B, C) with plates growing perpendicular to the surface. The a priori change in macroscopic appearance before (D) and after phosphidation (E). F) Ni<sub>5</sub>P<sub>4</sub> on nickel foam was measured in 0.5 M H<sub>2</sub>SO<sub>4</sub> rotating the working electrode at 2,000 rpm using a scan rate of 10 mV s<sup>-1</sup>.

### 5.3.1.1 Reaction kinetics

The kinetic parameters of Ni<sub>5</sub>P<sub>4</sub> towards the HER were carefully studied using chronoamperometric measurements in 10 mV steps scanning from positive to negative potential whereby each potential was held for 60 s. After steady state conditions were reached, the last point was used to construct *Tafel plots* as shown in Figure 25. A *Tafel slope* of ~53 mV dec<sup>-1</sup> in alkaline and ~40 mV dec<sup>-1</sup> in acidic solution were found for Ni<sub>5</sub>P<sub>4</sub> indicative for a *Volmer-Heyrovski* mechanism with the *Heyrovski*

step as rate determining step (RDS).[136] Compared to other nickel-rich phosphides, the *Tafel* parameter is comparatively small (63 mV dec<sup>-1</sup> for Ni<sub>12</sub>P<sub>5</sub> in acid;[149] 100 mV dec<sup>-1</sup> for Ni<sub>2</sub>P in base, 87 mV dec<sup>-1</sup> in acid;[148] 81 mV dec<sup>-1</sup> for Ni<sub>2</sub>P in acid,[129]) In this context, smaller *Tafel slopes* mean higher increase in hydrogen evolution rates and are therefore desired. The *Tafel slopes* of nickel and platinum are in line with literature values indicating the *Tafel step* as RDS for polycrystalline platinum (~30 mV dec<sup>-1</sup>) and a *Volmer step* as RDS for Nickel (~121 mV dec<sup>-1</sup>).[63, 178, 179]

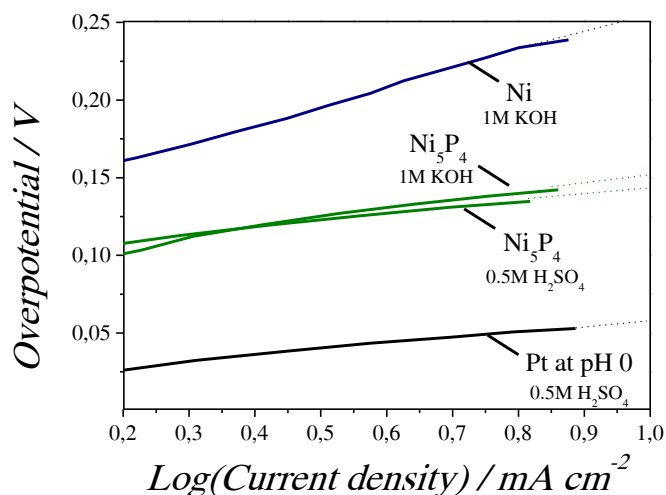


Figure 25: Steady state Tafel analysis (log (current density) vs. overpotential) of Ni<sub>5</sub>P<sub>4</sub>, Pt and Ni in 0.5 M H<sub>2</sub>SO<sub>4</sub> and 1 M KOH. The potential was altered in 10 mV steps towards more negative values holding each potential for 60 s.

### 5.3.1.2 Ex-situ XPS after the hydrogen evolution reaction

Ex-situ XPS was recorded after chronopotentiometry measurements for 20 h at -10 mA cm<sup>-2</sup> in either alkaline (1 M KOH) or acidic conditions (0.5 M H<sub>2</sub>SO<sub>4</sub>).

### After HER in alkaline environment

In the Ni 2p region, a signal at 857.0 eV was detected accompanied by a satellite peak at 862.3 eV (Figure 26). The peak shift of 3.5 eV compared to the nickel phosphide peak is very alike to the phosphate peak observed from the as synthesized Ni<sub>5</sub>P<sub>4</sub> sample. However, it might rather be interpreted as formation of Ni(OH)<sub>2</sub> since no phosphorus signal were observed in the P 2p region.[172] After flashing, nickel hydroxide was replaced by nickel phosphide since the Ni 2p<sub>2/3</sub> signal at 857.0 vanished and the emergence of metallic/phosphidic nickel at 853.6 eV (satellite peak at 859.8 eV) was observed instead. Moreover, the appearance of phosphidic P 2p peaks are in line with this explanation. However, these results have to be treated with caution since the catalyst was kept at open circuit in alkaline solution and reduction to the respective metallic compound might be possible at these low potentials applied.

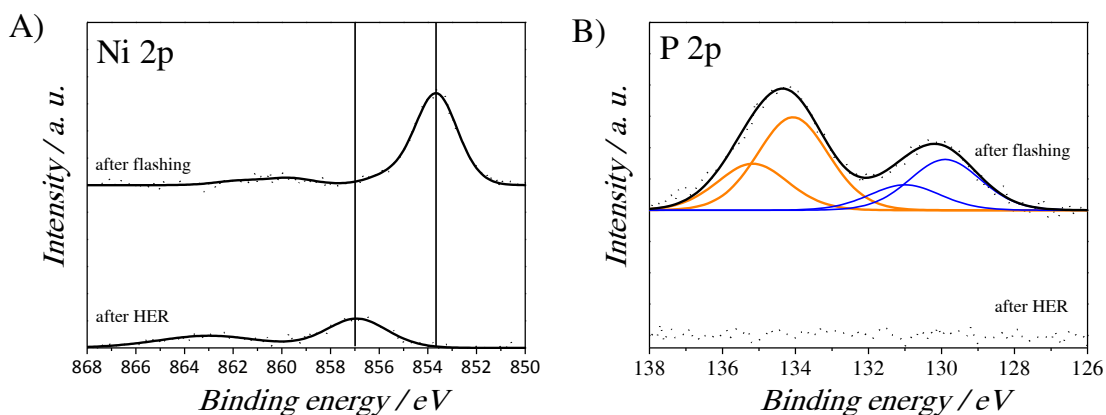


Figure 26: Ex-situ XPS for the Ni 2p (A) and P 2p (B) region after stability testing for 20 h at  $-10 \text{ mA cm}^{-2}$  in 1 M KOH before and after heat treatment to 1,000 K in ultra-high vacuum.

### After HER in acidic environment

After stability testing for 20 h at  $-10 \text{ mA cm}^{-2}$  in 0.5 M H<sub>2</sub>SO<sub>4</sub>, similar peaks to the as prepared Ni<sub>5</sub>P<sub>4</sub> sample were observed (Figure 27). Apparently, mainly nickel phosphide and phosphate can be found during electrocatalytic testing in acidic

solution. However, it cannot be excluded that during the electrocatalytic reaction, phosphate peaks are reduced to its phosphidic counterpart.

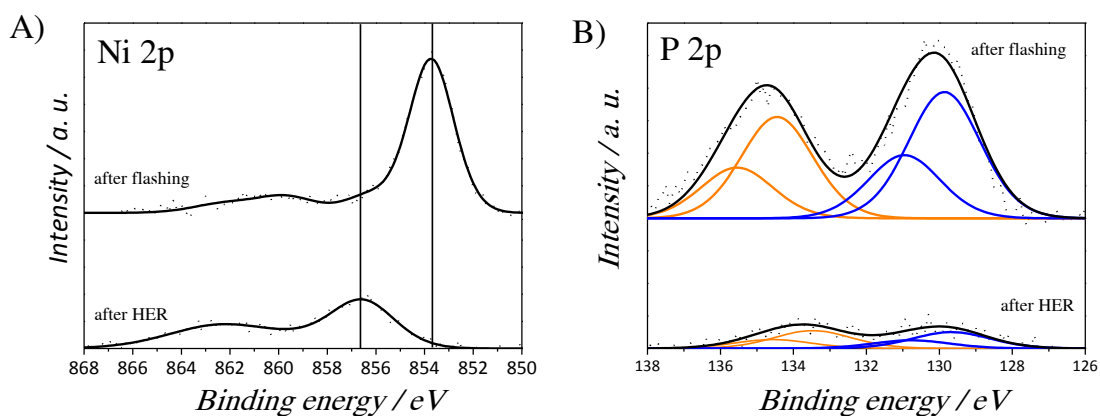


Figure 27: Ex-situ XPS for the Ni 2p (A) and P 2p (B) region after stability testing for 20 h at  $-10 \text{ mA cm}^{-2}$  in  $0.5 \text{ M H}_2\text{SO}_4$  before and after heat treatment to 1000 K in ultra-high vacuum.

### 5.3.2 Oxygen evolution reaction

The oxygen evolution reaction is considered the bottleneck of the total water splitting reaction due to sluggish kinetics in the four electron transfer reaction. In the following pages, *in-situ* preparation of amorphous nickel oxide descending from  $\text{Ni}_5\text{P}_4$  is highlighted and the active catalyst is pinpointed. Hitherto, ample efforts have been directed towards further understanding of nickel and its oxides (including nickel oxyhydroxides ( $\text{NiOOH}$ ) and nickel hydroxides  $\text{Ni}(\text{OH})_2$ ) in the OER, but research of alloyed nickel materials as phosphides, nitrides, or carbides is very scarce. Only recently, oxygen evolution catalysts can be found in literature ranging from metal alloys with non-metals incorporated into the structure as sulphur, selenium, nitrogen or phosphorus with e.g. proposed  $\text{NiSOH}$  or  $\text{Ni}_3\text{N}$  as active species.[180, 181, 182, 183, 184] However, post-determination of their structure and morphology are in most cases missing and rather ambiguous explanations for their activity can be found. In general, formation of new surface species has to be taken into account during the anodic reaction and cannot be ignored. Thermodynamically, even most oxides as NiO

or  $\text{Co}_3\text{O}_4$  are not stable during the oxygen evolution reaction which can be illustrated by *Pourbaix diagrams* as presented in chapter 3.4.[95] Due to the lack of literature concerning the oxygen evolution of  $\text{Ni}_5\text{P}_4$ , the processes taking place were prudently investigated. When comparing cyclic voltammetry curves of  $\text{Ni}_5\text{P}_4$ , Ni, Pt and Ir@C (Figure 28), it becomes obvious that  $\text{Ni}_5\text{P}_4$  performs superior with a steep increase of current density at low overpotentials, surpassing even Ir@C in the OER. In the OER, Iridium is considered to be one of the state-of-the-art catalyst. The onset potential of the oxygen evolution is often determined in literature by extrapolation of current voltage curves. In our case, due to the vast overlapping of the  $\text{Ni}(\text{OH})_2$  to  $\text{NiOOH}$  oxidation peak (Ni(II)/Ni(III)), preceding the oxygen evolution reaction, it was easy to make mistakes. Consequently, the exact onset potential of the oxygen evolution reaction was determined by non-invasive oxygen probe measurements in combination with a classical three electrode setup (Figure 28). In particular, the potential was scanned every 60 s in 5 mV steps to more positive potentials starting from 1.2 V vs. RHE while monitoring the oxygen content in solution. Hereby, a low onset potential of 0.25 V was found, belonging to the best known OER catalysts. A comparison of state-of-the-art catalysts for the OER can be found in Table S5.

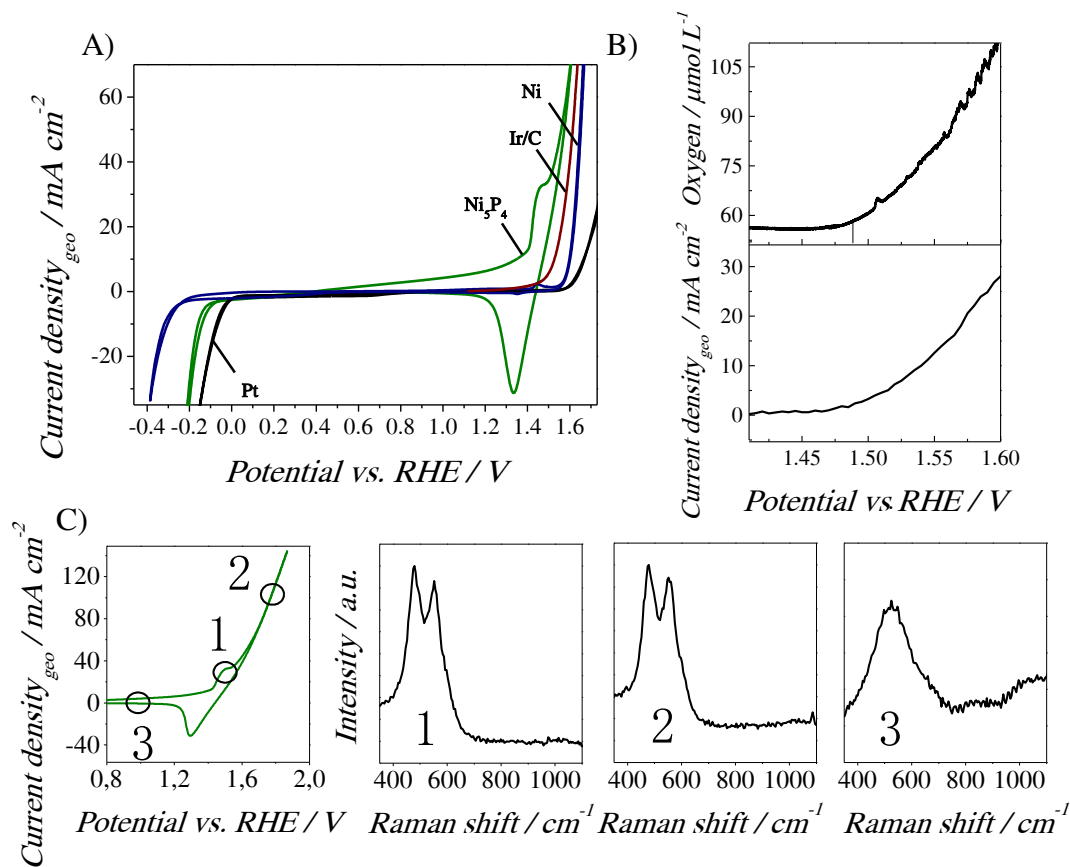


Figure 28: A) Cyclic voltammogram measurement of Ni, Pt,  $\text{Ni}_5\text{P}_4$  and Ir/C in 1 M KOH using a scan rate of  $40 \text{ mV s}^{-1}$  while rotating the working electrode at 2,000 rpm (iR corrected). B) Determination of onset potential measured in a typical three electrode setup (bottom) while consequently monitoring the oxygen content with an oxygen probe (top). C) Current voltage curves of the first cycle of  $\text{Ni}_5\text{P}_4$  illustrating key potentials indicated by #1, 2, 3 that were held constant for 10 h and the subsequent ex-situ Raman spectra of the samples.

It is even more striking when knowing that the binding of  $-\text{OH}^*$ ,  $-\text{O}^*$  and  $-\text{OOH}^*$  (the star indicates the adsorbed state) intermediates are connected in a scaling relationship, meaning when adsorption of one of these specimens is energetically favored, another is automatically disfavored leading to an onset overpotential of at least 0.2 V - 0.4 V.[96, 185, 186] This means the described catalyst works already close to the predicted limit. With increased overpotential ( $< 1.55 \text{ V vs. RHE}$ ), gaseous oxygen can be detected resulting in agitated curve progression in Figure 28. For  $\text{Ni}_5\text{P}_4$ , a continuous oxidation relatively early between 0.3 V - 1.4 V vs. RHE was observed (Figure 28) and continued reaching a plateau at  $\sim 1.5 \text{ V vs. RHE}$ . Directly afterwards

starts the water oxidation. When cycling back to reducing currents, a strong reduction peak can be observed. Similar to Bode and coworkers who observed the preceding formation of active material on pristine nickel electrodes in the OER[187, 188], also  $\text{Ni}_5\text{P}_4$  undergoes oxidation before the OER. For Nickel, when working in strong alkaline solution it is agreed on that very few  $\text{Ni}(\text{OH})_2$  layers instantaneously form on the nickel surface.[189, 190, 191, 192] This could be also confirmed for  $\text{Ni}_5\text{P}_4$  from ex-situ XPS data after electrochemical testing in alkaline environment (cf. Figure 26). The sensitivity of Raman spectroscopy towards the Ni-O-H vibrations from the hydroxide and oxyhydroxide phases makes it an excellent tool for determining indirectly the oxidation state of the active material. Vibrational modes from ex-situ Raman analysis indicates that the oxidation peak at around 1.4 V vs. RHE corresponds to the formation of  $\text{NiOOH}$  whereas the reductive current at  $\sim 1.25$  V vs. RHE results in the reduction of  $\text{NiOOH}$  to  $\text{Ni}(\text{OH})_2$  ( $\text{Ni}(\text{III})/\text{Ni}(\text{II})$  redox couple). The first cycle of  $\text{Ni}_5\text{P}_4$  during the OER is displayed in Figure 28. In order to get more insights about the potential dependency on  $\text{Ni}_5\text{P}_4$ , selected potentials denoted as # 1, 2, 3 were chosen for further analysis. Thereby, a selected potential was held constant for 10 h and the samples were subsequently investigated by ex-situ Raman spectroscopy. At a potential of 1.47 V vs. RHE (# 1) - the exact potential where the oxidation peak reaches its maximum - Ni-O vibrations from  $\text{NiOOH}$  ( $\nu_1 = 470 \text{ cm}^{-1}$ ,  $\nu_2 = 550 \text{ cm}^{-1}$ ) can be observed.[193, 194] These peaks have been assigned to a layered structure with  $\text{NiO}_2$  units of edge sharing  $\text{NiO}_6$  octahedra where protons are highly mobile. The peak at  $550 \text{ cm}^{-1}$  was assigned to  $\text{NiO}_6$  octahedral lattice modes.[195] The missing Ni-OH band at  $450 \text{ cm}^{-1}$  is indicative for the dehydrated form with vibration of Ni-O, not Ni-OH.[194] In principle, two forms of  $\text{NiOOH}$  exist, the  $\beta$  and  $\gamma$ -form. Due to the similarity of  $\beta$ - $\text{NiOOH}$  and  $\gamma$ - $\text{NiOOH}$ , it is not easy to make an exact determination of the corresponding phase. However, the higher peak intensities ratio at  $470 \text{ cm}^{-1}$  and  $549 \text{ cm}^{-1}$  ( $I_{470}/I_{550}$ ) speaks rather for the looser  $\gamma$ -structure than the closer packed  $\beta$ -specie.[196] At higher

potentials ( $E = 1.77$  V vs. RHE, 10 h, # 2), the same NiOOH peaks can be observed, indicating no phase transition at higher potentials. When doing first the conversion to NiOOH (10 h, 1.77 V vs. RHE) and afterwards the subsequent reduction at a potential of 1.07 V vs. RHE for 10 h, the typical Raman features of Ni(OH)<sub>2</sub> can be observed (#3, Figure 28). These results are consistent with the *Pourbaix diagram* of pristine nickel.[95] In particular, the broad peak at 521 cm<sup>-1</sup> can be ascribed to vibrations of the Ni-O stretching modes that is overlaying the symmetric stretching mode of Ni-OH (around 453 cm<sup>-1</sup>).[194, 195, 197] One possible explanation of the reduced Ni-OH peak lies in dehydration of Ni(OH)<sub>2</sub> at increased anodic potential leading to strong Ni-O vibrations.[194] As presumably  $\gamma$ -NiOOH is formed beforehand, the reduced species is rather likely to be  $\alpha$ -Ni(OH)<sub>2</sub> than the  $\beta$ -form even though mixed phases cannot be excluded.[198] Small additional peaks might be assigned to phosphates (P-O stretching:  $\nu=1,051$  cm<sup>-1</sup>; 863 cm<sup>-1</sup>).[199] A possible explanation of the observed phosphate peaks could lie in the incorporation of phosphate ions into the loose  $\alpha$ -Ni(OH)<sub>2</sub> structure or the attachment of phosphates onto the surface. Previously, it has been shown that counterions as carbonate, sulfate or acetate can be incorporated into the nickel hydroxide structure.[200] The interlayer distance of turbostratic  $\alpha$ -Ni(OH)<sub>2</sub> (~0.8 nm) surpasses the ion radii of phosphate (~0.24 nm, [201]) more than threefold leaving space for phosphate molecules.

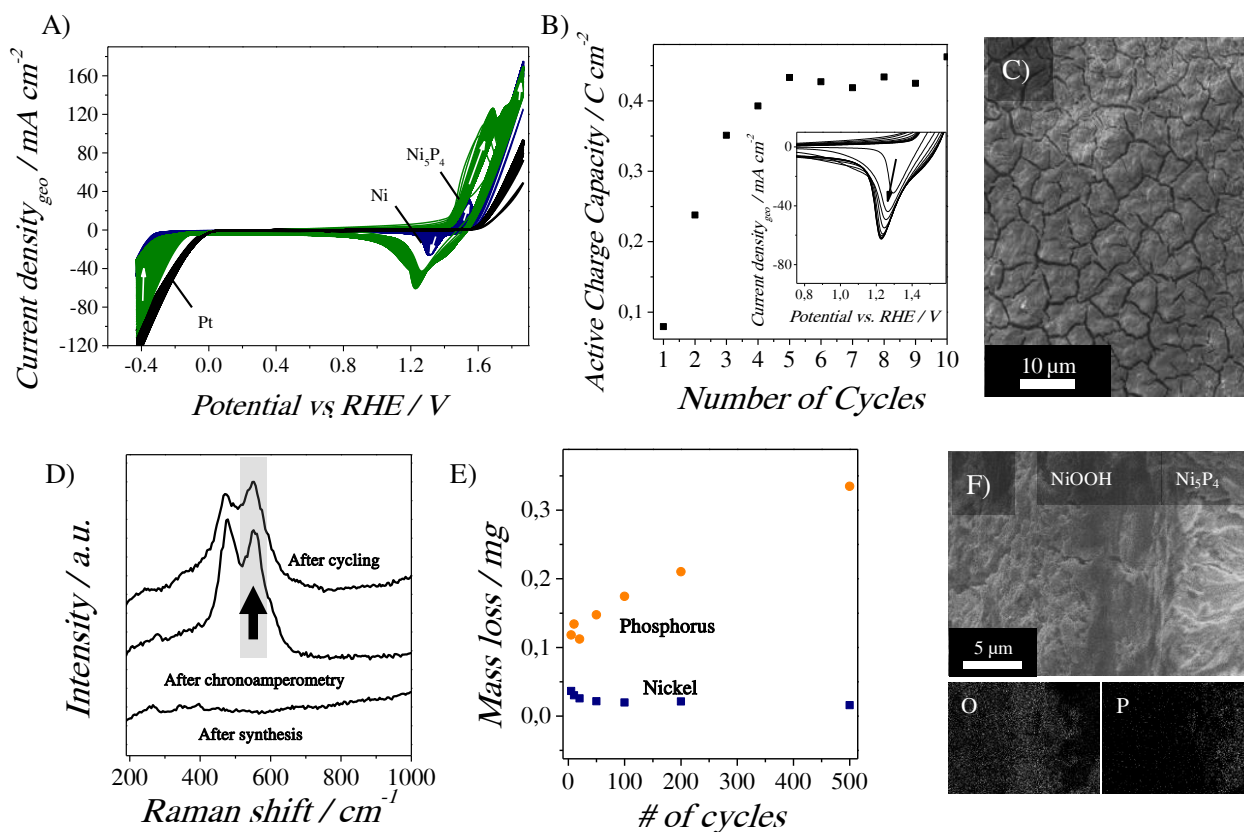


Figure 29: A) Electrochemical aging of Pt, Ni and Ni<sub>5</sub>P<sub>4</sub> was performed between -0.43V and 1.77 V vs. RHE using a scan rate of 40  $\text{mV s}^{-1}$  rotating the working electrode at 2,000 rpm. B) Active charge capacity obtained by integrating the current time curves of the reduction peak at around 1.25 V vs. RHE and its dependence on the cycle numbers. C) Surface morphology of Ni<sub>5</sub>P<sub>4</sub> after cycling and D) the corresponding Raman spectrum directly after synthesis, chronoamperometry (1.47 V vs. RHE) and 500 cycles. E) Nickel and phosphorus content in solution removed at 0.57 V vs. RHE and monitored after different OER cycles by ICP-OES. F) Cross-section SEM image of Ni<sub>5</sub>P<sub>4</sub> after cycling and the corresponding EDX mapping data.

Additionally, the Ni(II)/Ni(III) oxidation or the Ni(III)/Ni(II) reduction peak in Figure 28 can be used as indicator for the amount of active NiOOH present. Due to the proximity of the Ni(II)/Ni(III) transition / OER and the possibility of superposed phosphate formation, the cathodic peak (Ni(III)/Ni(II)) at around 1.3 V vs. RHE was used for the determination of active charge capacity. Herein, integrating the current density vs. time peak at around 1.3 V vs. RHE leads to the active charge capacity.[202] The capacity of the former Ni<sub>5</sub>P<sub>4</sub> sample exceeds more than 4,000 times the one of pristine nickel (Ni<sub>5</sub>P<sub>5</sub>: 74.2  $\text{mC cm}^{-2}$ ; Ni: 0.0169  $\text{mC cm}^{-2}$ ). The facilitated formation of higher oxides is attributed to the presence of phosphorus in the starting material and the unique morphology.

With the intention of further understanding the system on hand, electrochemical aging (500 cycles between -0.43 V and 1.75 V vs. RHE) was performed and is shown in Figure 29. Interestingly, in other literature sources, the anodic and cathodic peak from the Ni(II)/Ni(III) redox couple are both shifted to higher potentials.[196, 203] Here, an anodic peak shift to higher potentials and a cathodic peak shift to lower potentials were observed, indicating structure reinforcement with prolonged cycling time speaking for the transformation of the  $\alpha/\gamma$  into the  $\beta/\beta$  form observed from Raman spectroscopy as described further on. The change in charge capacity during cycling is displayed in Figure 29. The charge capacity increases strongly during the first cycles whereas minimal changes can be observed after five cycles. The resulting convergence in oxide growth during cycling can be attributed to the increased hindrance of hydroxide and water transport to the inner oxide regions, limiting the growth. Earlier, it was observed that  $\gamma$ -NiOOH is formed after chronoamperometric measurements for 10 h at high potentials. After cycling and one respective scan to high potentials (1.7 V vs. RHE), Raman spectroscopy indicates NiOOH formation with characteristic peaks at  $\sim 550\text{ cm}^{-1}$  and  $\sim 470\text{ cm}^{-1}$ . Due to cycling, the peak ratio ( $I_{470}/I_{550}$ ) changes in comparison to chronoamperometric aging, thus, indicating that structurally more ordered  $\beta$ -NiOOH is formed.[196]

After electrochemical cycling, characteristic tribasic phosphate peaks from FT-IR could be detected in solution, thus, supporting the theory of phosphate formation during cycling and NiOOH formation on the surface (Figure 30).[204, 205] It can further be argued that other non-tribasic phosphates can form but missing P-O(H) stretching modes (would arise at  $860\text{ cm}^{-1}$ ) and missing P-OH bending and stretching modes suggest otherwise.[199] The two peaks at  $561\text{ cm}^{-1}$  and  $601\text{ cm}^{-1}$  were assigned to  $\nu_1(\text{OPO})$  bending modes. The peak with the highest intensity at  $967\text{ cm}^{-1}$  was assigned to  $\nu_2(\text{PO})$  symmetric stretching. The antisymmetric stretching modes  $\nu_3(\text{PO})$  could be found between  $1,100\text{ cm}^{-1}$  and  $1,000\text{ cm}^{-1}$ . The broad band at around  $3,420\text{ cm}^{-1}$  and

the sharper peak at  $1,632\text{ cm}^{-1}$  correspond to O-H stretching and bending modes of  $\text{H}_2\text{O}$ , respectively. O-H stretching modes were found at  $645\text{ cm}^{-1}$ . The phosphorus and nickel content in solution was monitored with ICP-OES at different cycles (Figure 29). Hereby, an increasing amount of phosphorus is released into solution in form of phosphates whereas only marginal amounts of nickel were found with increased cycle number, speaking for the resilient character of nickel during catalysis. After 500 cycles, solely the hexagonal diffraction pattern from  $\text{Ni}_5\text{P}_4$  was found by PXRD, thus, revealing the amorphous character of upper  $\text{NiOOH}$  (Figure 30). Its importance for electrocatalysis becomes clear when knowing that well-crystalline nickel oxyhydroxide was found less active towards the OER than amorphous material.[206] In this manner, the higher structural disorder may favor vacancies, defects or changes in oxidation state of the metal ion preferential for the OER.[207, 208] However, amorphous materials are also more difficult to characterize and research is still ongoing to unravel the whole promotional effect of amorphous nickel based materials towards the OER. EDX-mapping before and after cycling demonstrates the transformation from phosphide to oxide material during cycling whereas almost no phosphorus can be detected after cycling (Figure 30).

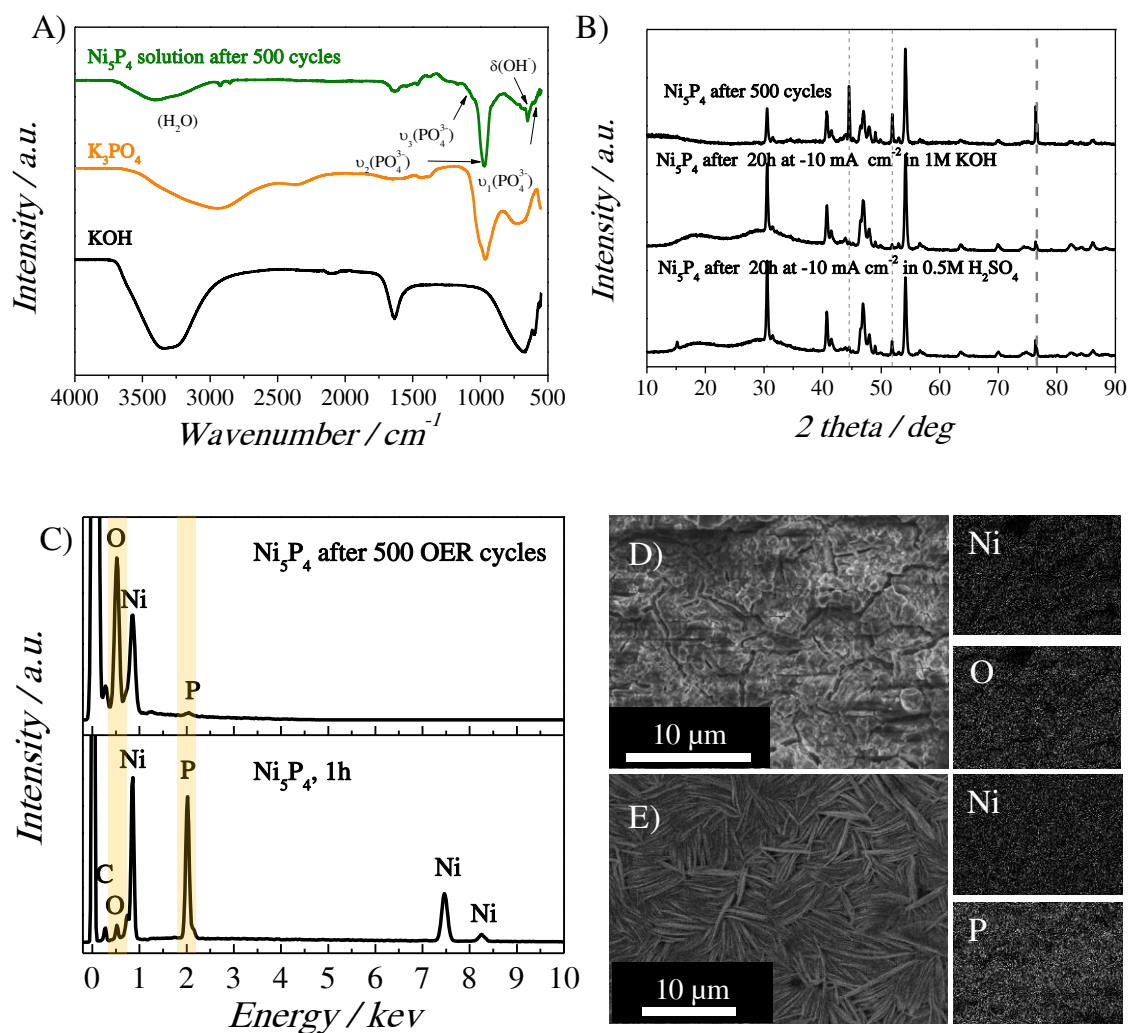


Figure 30: A) FT-IR-measurement of the solution after electrochemical aging and  $K_3PO_4$  and KOH as reference. B) PXRD pattern of  $Ni_5P_4$  after long-term electrochemical measurements of HER and OER. The potential was held for 20 h at  $-10 \text{ mA cm}^{-2}$  in alkaline/acidic solution (HER) or was cycled 500 times between  $-0.43 \text{ V}$  and  $1.75 \text{ V}$  vs. RHE in alkaline medium (OER). The dashed lines represent the diffraction pattern of cubic nickel due to cutting and exposing of the nickel substrate after electrochemistry measurements (Ni: ICDD 04-016-4761). C) EDX spectrum of  $Ni_5P_4$  directly after synthesis (bottom) and after 500 OER cycles (top) with the corresponding SEM images (D, E).

### 5.3.2.1 Stability

Without any pre-treatment before, the stability of  $Ni_5P_4$  and Ni was tested in 1 M KOH keeping the current density constant at  $10 \text{ mA cm}^{-2}$  for 20 h (Figure 31). Not only the activity of  $Ni_5P_4$  compared to nickel was superior but also its stability over time which can be attributed to the bounteous existence of active material.

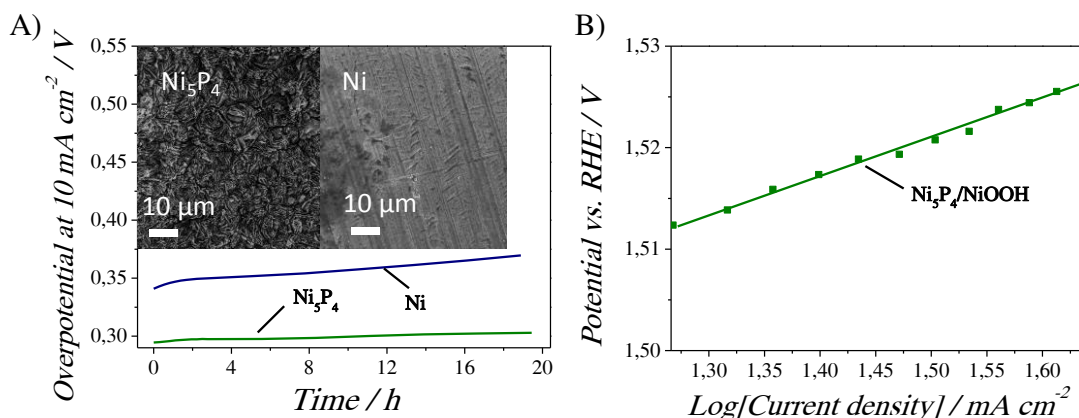


Figure 31: A) Long-term stability measurements of Ni (navy) and Ni<sub>5</sub>P<sub>4</sub> (olive) in 1 M KOH without electrochemical pre-treatment keeping the current density constant at 10 mA cm<sup>-2</sup> (iR corrected) and the corresponding post-catalytic SEM images. B) Tafel plots (log (current density) vs. overpotential) of Ni<sub>5</sub>P<sub>4</sub> without pre-treatment in 1 M KOH measured via chronoamperometric measurements in 10 mV steps (each step 20 min).

### 5.3.2.2 Reaction kinetics

In order to study the kinetic parameters involved, chronoamperometry measurements were performed in 10 mV steps, each step 20 minutes in order to give the system enough time to equilibrate to the active species, thus, monitoring only the OER (Figure 31). A *Tafel slope* of ~40 mV dec<sup>-1</sup> was found which is in correlation with the observed *Tafel slope* found in literature for NiOOH. Thereby, different mechanisms based on a *Tafel slope* of 40 mV dec<sup>-1</sup> have been discussed. A hydrogen peroxide path for instance was proposed by Bell and coworkers where discharging of an OH<sup>-</sup> ion and the subsequent electron transfer as RDS leads to physisorbed H<sub>2</sub>O<sub>2</sub> as intermediate.[196] Another possible mechanism encompasses the formation of Ni-OH as first step, the oxidation to Ni-O, and the final recombination of two adsorbed O<sub>ad</sub>. [209] However, about the exact mechanism can only be speculated. Even though the activity of Ni<sub>5</sub>P<sub>4</sub>/NiOOH is much higher than for Ni/NiOOH, the *Tafel slope* as intensive parameter – no dependency on e.g. surface area – stayed the same.

With all data on hand, it was established that Ni<sub>5</sub>P<sub>4</sub> is indeed oxidized to higher (oxy)hydroxides and one can now lay out a possible reaction mechanism. With the

knowledge of phosphate formation during oxidation and NiOOH formation on the electrode, the following reaction is proposed. For pristine nickel, only three electrons per nickel atom are transferred to form NiOOH at higher potentials ( $E > 1.3$  V vs. RHE) whereas more than three times more electrons are transferred for Ni<sub>5</sub>P<sub>4</sub>. Furthermore, three times more OH<sup>-</sup> is consumed in comparison to pure nickel per nickel atom. As the potential strongly depends on the concentration of OH<sup>-</sup> ions, the pH was checked with a pH meter before and after electrocatalytic cycling. However, due to OH<sup>-</sup> excess in solution, the possible potential shift due to OH<sup>-</sup> consumption during oxidation was found to be negligible.



The transformation of Ni<sub>5</sub>P<sub>4</sub> into the active catalyst and the accompanied superior catalytic activity may be assigned to the following reasons:

- the hexagonal crystal structure of Ni<sub>5</sub>P<sub>4</sub> favors the conversion to hexagonal Ni(OH)<sub>2</sub> and NiOOH due to structural similarity,
- the facile oxidation of P<sup>n-</sup> to stable phosphates as shown by FT-IR measurements,
- the sheet-like morphology enables the formation of active catalyst by higher accessibility of active sites,
- and the formally higher oxidation state of nickel.

In cobalt borides, the transformation to higher oxides was attributed to increased number of unpaired valence electrons.[210] Similarly, the paramagnetic nature of Ni<sub>5</sub>P<sub>4</sub> implies unpaired electrons and could be also considered as a reason for the observed ameliorated oxide formation.[174] However, profound explanations were missing and additional studies have yet to be conducted to unravel the whole

promotional effect of phosphorus containing materials in the nickel (oxy)hydroxide formation.

### 5.3.3 Full water splitting

Finally, the practical relevance for the overall water splitting reaction is illustrated in Figure 32.  $\text{Ni}_5\text{P}_4$  was used as anode and cathode material simultaneously and compared with pristine nickel and platinum in alkaline medium (1 M KOH). Less than 1.7 V is necessary to reach  $10 \text{ mA cm}^{-2}$  whereas 1.8 V is needed for platinum and over 1.9 V for nickel. Even optimized systems using foams instead of foils with much higher surface area are in the same overpotential/current density range as the presented catalyst.[211] When dividing the overpotential necessary to reach  $10 \text{ mA cm}^{-2}$  by the theoretical necessary potential to split water (1.23 V), a simplified voltage efficiency can be obtained. The calculated efficiency translates into 72% under these simplified conditions and makes  $\text{Ni}_5\text{P}_4/\text{NiOOH}$  one of the state-of-the-art catalysts for full water splitting.

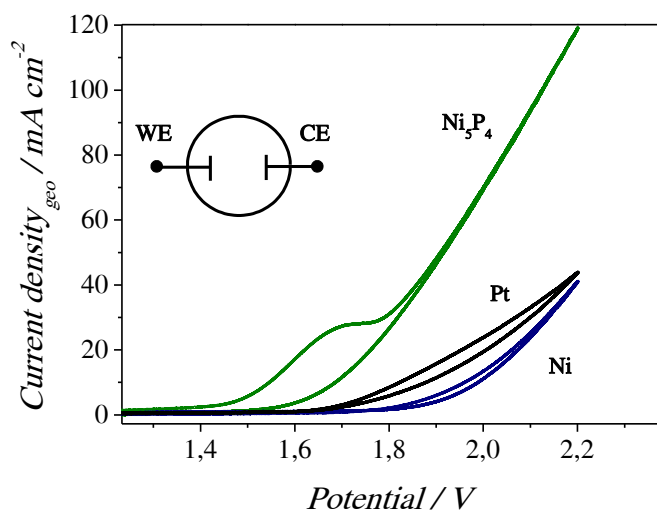


Figure 32:  $\text{Ni}_5\text{P}_4$ , Pt and Ni foils tested in a two electrode setup in 1 M KOH while stirring the solution.

## 5.4 Summary

The results described herein introduce a new catalyst type for the hydrogen and oxygen evolution reaction. The facile synthesis of  $\text{Ni}_5\text{P}_4$  based on earth abundant materials and its high activity accentuate the promising potential towards full electrocatalytic water splitting. A possible formation mechanism was proposed based on monitoring of the nickel phosphide growth. It was shown that bilayer structures on top of nickel emerge as crystalline  $\text{Ni}_{12}\text{P}_5$  and  $\text{Ni}_5\text{P}_4$ . Thereby,  $\text{Ni}_{12}\text{P}_5$  was found in close proximity to the support whereby the phosphorus-rich phase was found on top. Hexagonal single crystals emerge as plates with preferential growth in  $[10\bar{1}0]$  direction. Additionally, the hierarchical morphology and intrinsic properties of  $\text{Ni}_5\text{P}_4$  give rise to high hydrogen evolution activity following the *Volmer-Heyrovski* mechanism with the *Heyrovski* step as RDS. Post-characterization after long-term stability measurements demonstrates the high durability of  $\text{Ni}_5\text{P}_4$  in acidic and basic solution. As only little information about the oxygen evolution reaction of nickel phosphides exist, in-depth assessment of processes arising at the metallic interface was conducted. The propensity of *in-situ* phosphate formation during oxygen evolution allows for straightforward materialization of active catalyst with amorphous character. The formation of  $\gamma$ -NiOOH (keeping the potential constant for 10 h,  $> 1.4$  V vs. RHE) and  $\beta$ -NiOOH (500 cycles,  $-0.43$  V -  $1.75$  V vs. RHE) in  $\text{Ni}_5\text{P}_4$  is favored compared to pristine nickel. As (oxy)hydroxides are not only useful in electrocatalysis, but also in organic synthesis,[212] or secondary alkaline batteries,[206] the concept of starting with ordered phosphide material may be adapted for other phosphorus containing materials. Additionally, this is – to the author’s knowledge – the first in-depth assessment of transformation of  $\text{Ni}_5\text{P}_4$  to amorphous nickel oxyhydroxide during the oxygen evolution reaction. Further data for nickel nitrides and sulfides – not elaborated further in this thesis – also clearly

indicates a Ni(II)/Ni(III) formation peak in cyclic voltammetry measurements preceding the oxygen evolution reaction. It is therefore advisable that also other sulfides, selenides or borides reported in literature as being active towards the OER should be reviewed under the aspect of amorphous oxyhydroxide formation during oxygen evolution. Further investigation about the exact active specimen is thereby inevitable. The judicious choice of phosphide material (e.g. Ni<sub>2</sub>P, Ni<sub>12</sub>P<sub>5</sub>...) may lead to enhanced accessibility of other *in-situ* formed, amorphous oxygen evolution catalysts. The active charge capacity of Ni<sub>5</sub>P<sub>4</sub> surpasses that of nickel about 4,000 times already after the first cycle, thus, explaining the high activity of Ni<sub>5</sub>P<sub>4</sub>. A much higher amount of nickel centers may be surface exposed due to the formation of nickel oxyhydroxide domains in comparison to its nickel congener.

## 6 Experimental and theoretical benchmarking of nickel based materials for the hydrogen evolution reaction

---

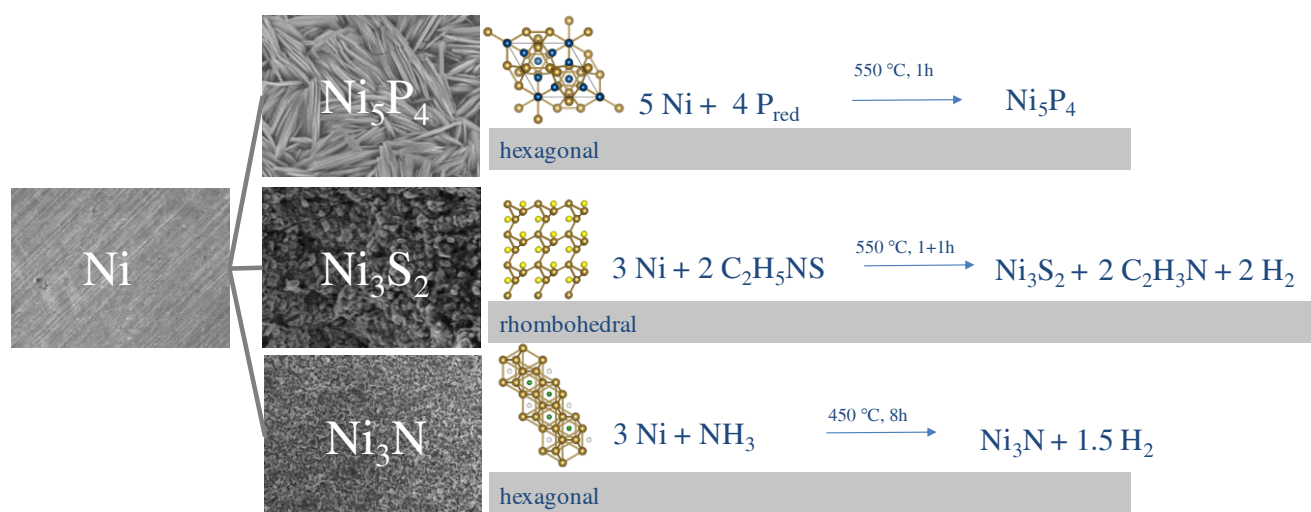
### 6.1 Background

As seen in the previous chapter, nickel phosphide exhibits high activity towards the HER and can be synthesized by easy means. Other research groups reported high activity and stability on several classes of materials including sulphides, carbides and nitrides.[37, 46, 213] Composite materials such as nickel–molybdenum nitride or cobalt phosphosulphide have demonstrated high activity even under acidic conditions.[214, 215] Only recently, a study of transition metal phosphides revealed theoretical and experimental insights into the inherent properties of phosphide materials.[36] Moreover, former studies showed that the heat of adsorption scales relatively accurately with the measured catalytic activity.[33, 36, 43, 216]

However, theoretical and experimental correlations of other nickel based ceramics do not exist and their high activity towards the HER is still not fully understood. To address this point, the catalytic activity of different nickel based alloys was measured and compared to their hydrogen adsorption free energy using density functional theory (DFT). Thereby, DFT can provide useful parameters for the understanding of intrinsic activity and correlations to experimental data are only feasible if strict interplay of all three subparts – material chemistry, electrochemistry and theoretical chemistry – is ensured. Already known materials active towards the HER such as  $\text{Ni}_3\text{S}_2$ , Pt or Ni were compared experimentally and theoretically to still not evaluated and novel materials such as  $\text{Ni}_5\text{P}_4$  and  $\text{Ni}_3\text{N}$ . All materials were chosen for two reasons: the distinct chemical diversity between the heteroatoms on the one hand and the existence of highly ordered crystal structures on the other. The preparation pathways

---

of all materials including their morphology and crystal structure are compared in Scheme 2. All theoretical calculations were realized in the theory department of the Friedrich-Alexander University Erlangen-Nürnberg by Hannah Schlott as part of her master degree under the supervision of Prof. Bernd Meyer.[217] By pre- and post-catalytic characterizations of all catalysts and underpinned DFT calculations, correlations between the hydrogen adsorption free energy and the heteroatom influence were studied. However, still facing challenges must not be underestimated as e.g. varying active surface areas or morphologies and will be discussed further.



Scheme 2: Overview of all synthesized materials with different morphologies and their crystal structures.

## 6.2 Preparation

As for nickel phosphide, the strategy of choice was synthesizing the active catalyst directly onto pristine nickel foil. The direct modification of the support material offers the advantage of higher surface area control with less synthesis steps required. Furthermore, the use of polymeric binders, commonly utilized to bind nanoparticles onto the electrode, was redundant and could be prevented (cf. chapter 5). But before going more into detail about the electrocatalytic performance and the hydrogen adsorption energies of these materials, one has to delve more on synthesis strategies,

their structures and properties in order to understand why these materials may ultimately have the potential to become a replacement for noble metal catalysts.

What all these materials have in common is an electropositive metal center with electronegative main group elements prompting similar characteristics. The bonding characteristic in these material classes is very diverse ranging from metallic to ionic and covalent bonding. However, as one prerequisite of an efficient electrocatalyst is their low electrical resistivity, all investigated materials were chosen due to their high conductivity.

Carbides and nitrides share similar crystal structures and are in general relatively alike while phosphides and sulfides are more diverse and complex. Since carbon and nitrogen are relatively small elements, interstitial, compact crystal structures are formed such as e.g.  $\text{Ni}_3\text{C}$  and  $\text{Ni}_3\text{N}$ . For  $\text{Ni}_3\text{N}$  and  $\text{Ni}_3\text{C}$ , stable interstitial structures were predicted by geometric considerations only. Hägg and coworkers suggested a not exceeding ratio of non-metal to metal radius of around 0.59 for the stable formation of interstitial compounds.[218] Since sulfur (1.05 Å) and phosphorus (1.07 Å) comprise much higher atomic radii than carbon (0.76 Å) and nitrogen (0.71 Å), interstitial compounds are not formed with e.g. nickel (1.24 Å).[219] The larger anion size (together with lower lattice energy) is the reason why larger degrees of non-stoichiometric compounds can be found for sulfides and phosphides.[151]

### **6.2.1 Nickel sulfide ( $\text{Ni}_3\text{S}_2$ )**

Nickel sulfide has found its way into electrochemical devices through supercapacitors[220, 221], lithium ion batteries[222] and as water splitting catalyst[223, 224, 225, 226]. Particularly, heazlewoodite ( $\text{Ni}_3\text{S}_2$ ) is of special interest in electrocatalysis due to its high conductivity.  $\text{Ni}_3\text{S}_2$  adopts a hexagonal crystal structure with short Ni-Ni bonds. The shortest nickel-nickel separations (2.49 Å and 2.50 Å) are equal or only slightly larger than the shortest Ni-Ni bonds in cubic metallic

nickel (2.49 Å) leading to metallic conductivity.[227] Unlike other sulfides as NiS or NiS<sub>2</sub>, a continuous network of Ni-Ni bonds is formed throughout the material.[228] Heazlewoodite has been synthesized previously by using elemental sulfur[229, 230, 231], thiourea[232, 233, 234], H<sub>2</sub>S[227], Na<sub>2</sub>S[235] or octanethiol[236] as precursors and can be found naturally in copper-nickel sulfide ores. However, the sulfidation of pristine metal is often accompanied by other sulfide formation as e.g. NiS due to non-stoichiometric reaction partners.[237] Therefore, careful design and control of synthesis conditions is mandatory. Herein, thioacetamide (TAA) was chosen as a simple and low cost sulfidation source, decomposing into acetonitrile and H<sub>2</sub>S at around 180 °C. After decomposition of TAA, acetonitrile was collected and evolved H<sub>2</sub>S was used for further sulfidation making the need for gas bottles redundant. A more detailed synthesis description can be found in the appendix. As already mentioned in the introduction, a series of crystal structures of nickel sulfide are known due to the large anion size. After one hour of reaction between H<sub>2</sub>S and nickel foil, several sulfide phases were formed as observed by PXRD (Figure 33). After an additional annealing step at 550 °C for one hour, pristine Ni<sub>3</sub>S<sub>2</sub> was obtained (Figure 33). This result is well in line with other work in literature where NiS decomposition was observed at elevated temperatures forming Ni<sub>3</sub>S<sub>2</sub> and elemental sulfur (Bp: 446 C).[238] The cross-section SEM/EDX image indicates a film thickness of ~10 μm with homogeneous nickel/sulfur distribution and underlying nickel (Figure 33). The theoretically obtained Ni/S ratio coincides well with the experimentally obtained value determined by EDX measurements (Ni/S<sub>theo</sub>: 1.5; Ni/S<sub>EDX</sub>: 1.48 ± 0.16, three samples).

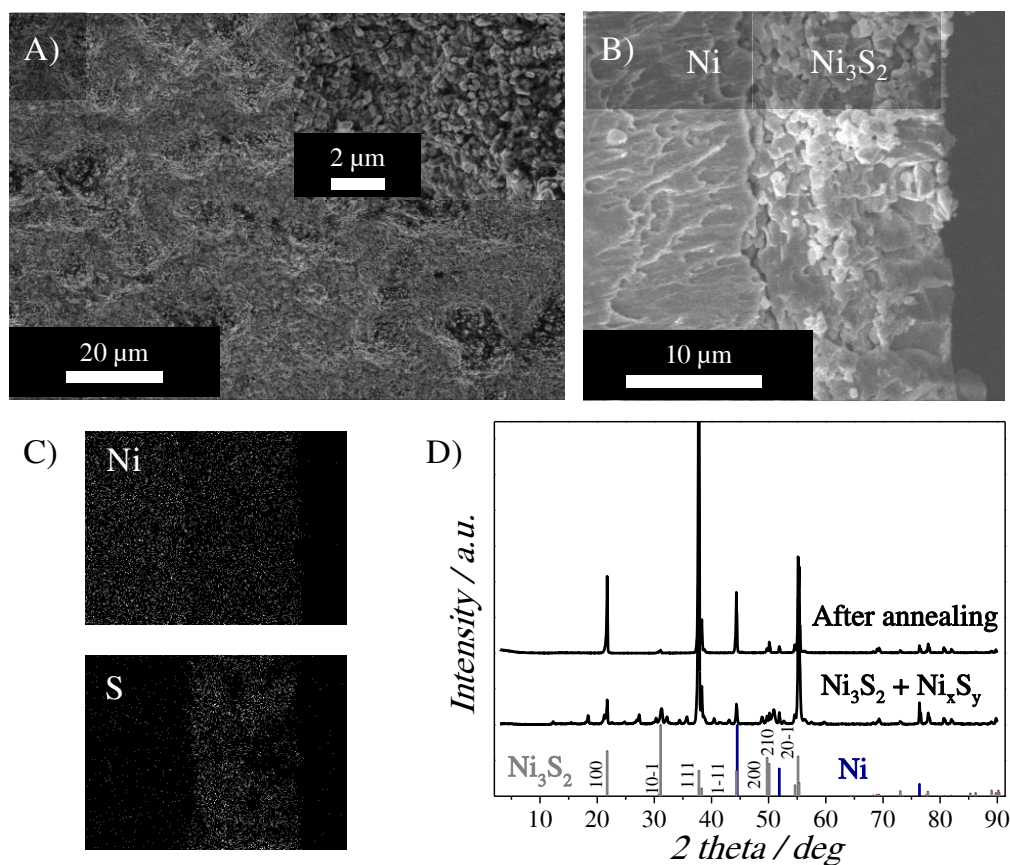


Figure 33: A) Top-view and B) cross-section SEM image of  $\text{Ni}_3\text{S}_2$  after synthesis and C) the corresponding EDX mapping of sulfur and nickel. D) PXRD pattern of synthesized  $\text{Ni}_3\text{S}_2$  on nickel foil with selected reference peaks of Ni (ICDD: 04-008-845) and  $\text{Ni}_3\text{S}_2$ : (ICDD: 04-014-7901).

### 6.2.2 Nickel nitride ( $\text{Ni}_3\text{N}$ )

Nickel nitride can be described as metallic interstitial compound with hexagonal crystal structure where nitrogen is found in the octahedral holes of the basically fcc nickel framework (cf.  $\text{Ni}_3\text{C}$ , chapter 4). Similar to heazlewoodite,  $\text{Ni}_3\text{N}$  possesses metallic conductivity with short Ni-Ni bonds between 2.62 Å and 2.69 Å. Despite the given prerequisite of high conductivity,  $\text{Ni}_3\text{N}$  is still unexplored as hydrogen evolution catalyst which is predominantly owing to the difficulty in synthesizing phase-pure materials. In 2015, a facile and straightforward synthesis route of  $\text{Ni}_3\text{N}$  was proposed by using melamine, cyanuric acid and barbituric acid as precursors.[239] Despite the practicability of the synthesis, carbon impurities were always found. Other nitrogen sources comprise urea[240], nitrogen[241, 242] or azides[243]. However,

surrounding/incorporated carbon or high necessary pressures going with them are rather disadvantageous for the aimed purpose. As phase-pure materials are compulsory for the sought after intention,  $\text{NH}_3$  was chosen as nitrogen source due to its high worldwide production volumes (*Haber-Bosch process*) and its nitriding abilities.[244] In this context, reports on nickel nitride from ammonia and nickel are already dating back to the early 20<sup>th</sup> century leading to  $\text{Ni}_3\text{N}$  and  $\text{H}_2$ . [245, 246] After 8 h of constant  $\text{NH}_3$  flow over cleaned nickel foil, the typical hexagonal reflections were observed by PXRD. The PXRD pattern can be found together with the corresponding SEM image in Figure 34. Scaling problems due to non-stoichiometric reactants were not accounted due to the limited amount of existing nickel nitride phases ( $\text{Ni}_2\text{N}$ ,  $\text{Ni}_3\text{N}$  and  $\text{Ni}_4\text{N}$ ) and the instability of most of the other phases.[247]

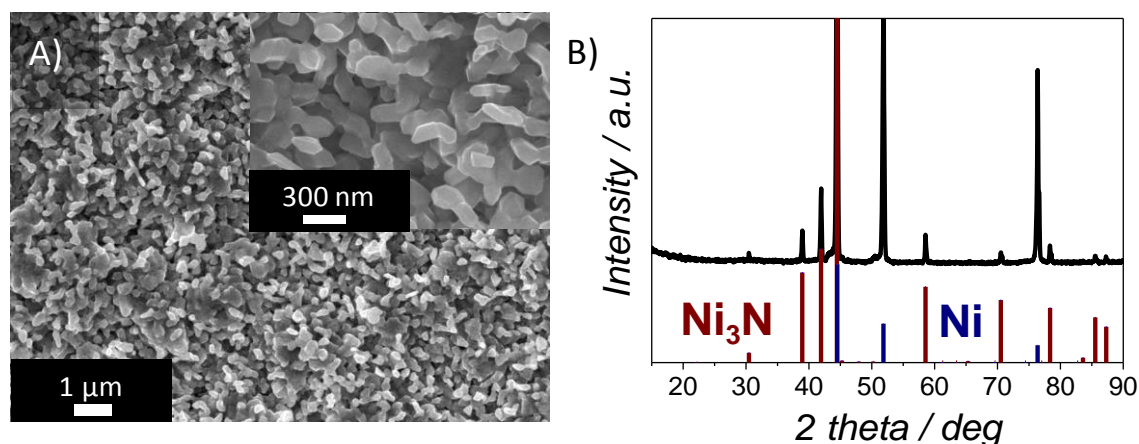


Figure 34: A) PXRD of  $\text{Ni}_3\text{N}$  with reference patterns of  $\text{Ni}$  (ICDD: 04-008-845) and  $\text{Ni}_3\text{N}$  (ICDD: 04-011-1882) and the corresponding SEM image (B).

### 6.2.3 Nickel phosphide ( $\text{Ni}_5\text{P}_4$ )

The preparation and characteristics of nickel phosphide were described in detail in the previous chapter and the interested reader is therefore referred to chapter 5.

Nevertheless, for the sake of completeness, the corresponding PXRD and SEM images can be found in Figure 35.

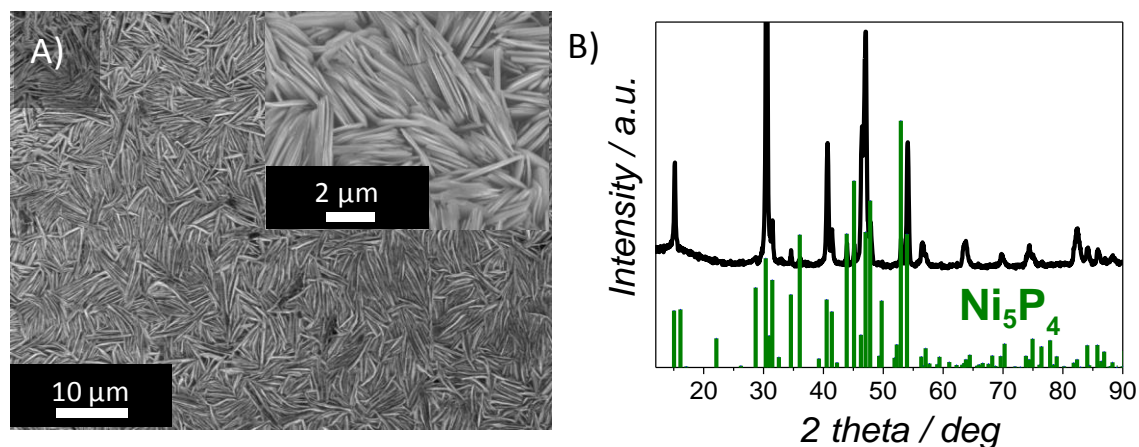


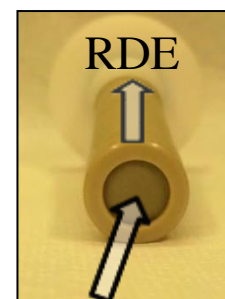
Figure 35: A) SEM image of  $\text{Ni}_5\text{P}_4$  after 1 h at 550 °C under high and low magnification and the resulting PXRD (B),  $\text{Ni}_5\text{P}_4$ : ICDD: 04-014-7901.

### 6.3 Adsorption and the famous Volcano plot

In the previous section, routes towards crystalline nickel ceramics have been explored using abundant and easy to handle starting materials. In the following, nickel sulfides, nitrides and phosphides were experimentally evaluated towards the HER and their dependency on the hydrogen adsorption free energy ( $\Delta G$ ) was studied. In the past, pristine metals were either often tested without rotation connected directly to the potentiostat or by using nanoparticles on an inert electrode surface (e.g. glassy carbon) where convection can be deliberately evoked. As

described in chapter 5 in more detail, the use of nanoparticles is

accompanied by possible interference during electrocatalytic testing. For pristine metals, overpotentials due to diffusion problems, caused by slow transport of reactants and products, should not be underestimated. Due to the highly active



Electrode

Figure 36: Rotating disk electrode adapted for the specific use of foils under rotation during the HER.

nature of the investigated materials towards the HER, gas bubble accumulation was a challenge in the beginning. Therefore, a special in-house adapted hanging-meniscus disk with an exposing surface area of  $0.43 \text{ cm}^2$  was used for measuring foils under rotation (Figure 36). Figure 37 displays the current voltage characteristics of each material in 1 M KOH, rotating the working electrode at 2,000 rpm. In order to avoid imprecise results, chronoamperometric measurements were performed resting for 60 s at a certain potential whereby the potential was moved in 10 mV steps towards more negative values. Before measurement of each catalyst, the corresponding materials were exposed to repetitive cycling in the hydrogen evolution region in order to reduce possible oxide layers on top.

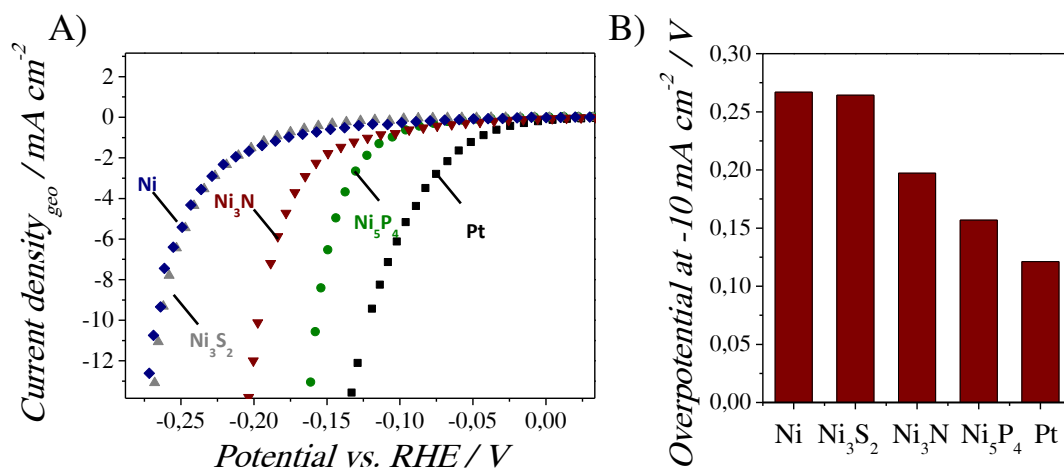


Figure 37: A) Current voltage characteristics of  $\text{Ni}_3\text{N}$ ,  $\text{Ni}_5\text{P}_4$ ,  $\text{Ni}_3\text{S}_2$ , Pt and Ni in 1 M KOH rotating the working electrode at 2,000 rpm and the corresponding overpotential at  $-10 \text{ mA cm}^{-2}$  (B).

As a figure of merit, the overpotential at  $-10 \text{ mA cm}^{-2}$  was taken due to its direct impact for solar-based water-splitting devices and is shown in Figure 37 (cf. chapter 1).[248] All characteristic tests were performed in strongly alkaline (1 M KOH) medium since dissolution was initiated for Ni,  $\text{Ni}_3\text{N}$  and  $\text{Ni}_3\text{S}_2$  in acidic medium (0.5 M  $\text{H}_2\text{SO}_4$ ) when no load was applied. While Figure 37 displays the activity of the electrode material based on the geometrical current density, it would be useful to

know the electrochemically active surface area (ECSA). Even though the apparent current density is rather practical considering the applicability in real devices, the real surface area is much more desirable for fundamental research. In this manner, the electrochemically active surface area for each system was estimated by electrochemical double layer capacitance ( $C_{DL}$ ) measurements.[248] In  $C_{DL}$  measurements, the scan rate and the capacitive current – where no faradaic current response occurs – are strongly dependent on each other. According to equation 6.1, the current response due to electrode charging obtained from cyclic voltammetry is directly proportional to the scan rate  $\nu$  and  $C_{DL}$ .

$$I = C_{DL} \nu \quad 6.1$$

A voltage window of 0.1 V around the open circuit potential was used and all measured current was assumed to be double layer charging current. Exemplarily, the current voltage response of  $Ni_5P_4$  at different scan rates is shown in Figure 38. The resulting scan rate vs. current (density) response of  $Ni_5P_4$  is shown in Figure 38, resulting in a straight line with the slope equal to  $C_{DL}$ . For  $Ni_5P_4$ , the electrochemical double layer capacitance was approximately 1 mF  $cm^{-2}$ . For ECSA determination, the measured double layer capacitance was correlated with the specific capacitance  $C_s$  of ideally clean, smooth and bright electrodes of the tested material (equation 6.2). However, experimentally obtained values of  $C_s$  vary between 20-80  $\mu F cm^{-2}$  for pristine nickel while no values are available for the investigated ceramic materials.[249]

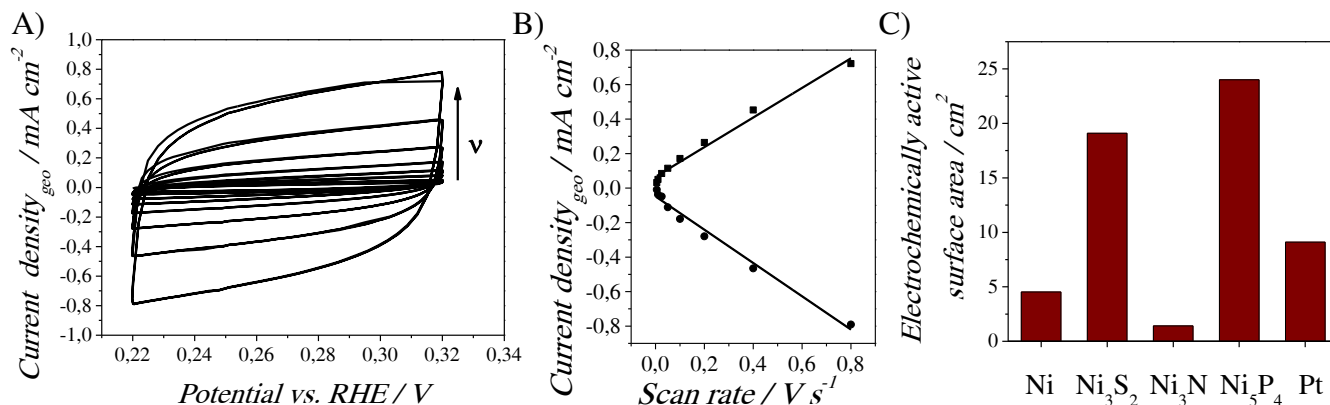


Figure 38: Determination of the electrochemically active surface area: A)  $C_{DL}$  measurements of  $Ni_5P_4$  from cyclic voltammetry in 1 M KOH. A non-faradaic region was selected depending on the open circuit potential. The latter was held for 300 s followed by the measurement of cyclic voltammetry in a 0.1 V window around the open circuit potential with the following scan rates  $v$ : 0.005, 0.01, 0.025, 0.05, 0.1, 0.2, 0.4, and 0.8  $V s^{-1}$ . B) The anodic and cathodic charging current taken from the most positive and negative potential applied during cycling and its dependency on the scan rate. The mean of both linear fits (anodic and cathodic) was taken for determining  $C_{DL}$ . C) Determined electrochemically active surface areas of all investigated materials per geometrical area of material ( $cm^2$ ).

Therefore,  $C_S$  was estimated to be 40  $\mu F cm^{-2}$  for all materials as proposed in literature for metals, metal oxides and phosphides.[36, 248]

$$ECSA = C_{DL} C_S^{-1} \quad 6.2$$

Even though the determination of ECSA by capacitance measurements is often used in the field, some uncertainties remain. Hereby, the ECSA can only serve as approximation due to different factors affecting the measured capacitance. In this manner, occurring pseudo capacitance or altered conductivities have to be named that can lead to divergent results. However, the conductivities for all materials are assumed to be relatively alike (metallic).[174, 227] As a general trend, however, it becomes clear that  $Ni_5P_4$  shows the highest electrochemically active surface area followed by  $Ni_3S_2$ , Pt, Ni and  $Ni_3N$  (Figure 38). In Figure 39, the hydrogen adsorption Gibbs free energy ( $\Delta G$ ) is plotted against the calculated exchange current densities. All calculation details can be found in [217]. Nickel can be found on the left branch of the volcano where hydrogen bonding is rather strong. In this manner, the hydrogen adsorption free energy for nickel was used as benchmarking and reference value. It

coincides well – marginally shifted to the left – with reported values from Nørskov and coworkers.[216] Platinum – taken from the same reference – on the other hand possesses  $\Delta G$  values close to zero and can be found on the top of the volcano. This is well in line with experimental observations where Pt shows the highest activity in 1 M KOH followed by  $\text{Ni}_5\text{P}_4$ .

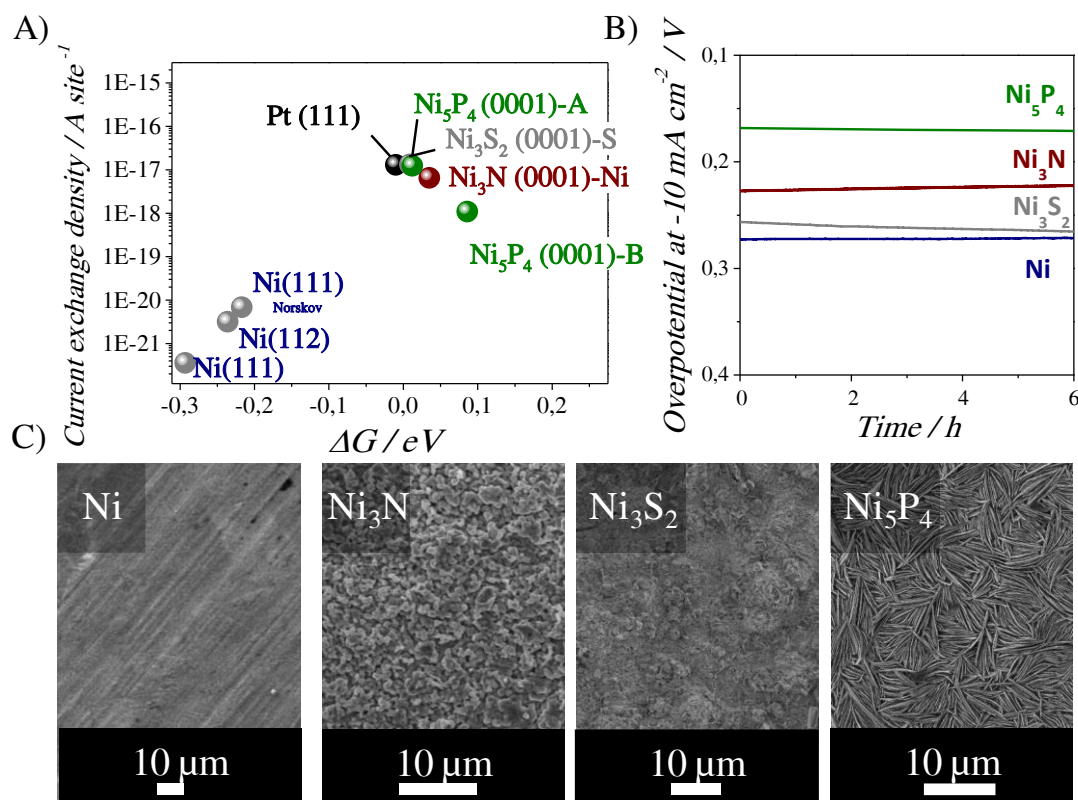


Figure 39: A) Volcano plot of calculated  $\Delta G$  as function of exchange current density. Nickel was employed as benchmarking value in order to correlate with in literature reported values.[216] B) Long-term stability testing (6 h) for Ni,  $\text{Ni}_3\text{N}$ ,  $\text{Ni}_3\text{S}_2$  and  $\text{Ni}_5\text{P}_4$  in 1 M KOH and the resulting SEM images (C) of  $\text{Ni}_3\text{S}_2$ ,  $\text{Ni}_5\text{P}_4$ , Ni and  $\text{Ni}_3\text{N}$  after the 6 h test.

Both materials are highly resistant against corrosion even under acidic conditions (cf. chapter 5.3.1). As observed from experimental data, nickel phosphide and nitride show higher, nickel sulphide very similar catalytic behavior compared to pristine nickel. Certainly, all non-metal containing materials tested here were found on the right branch or on the top of the volcano with increased free energy of adsorption

compared to nickel. In literature, also MoS<sub>2</sub> as well as metal phosphides were found on the right branch of the volcano.[35, 36] For Ni<sub>3</sub>S<sub>2</sub>, two surface terminations have been investigated: Ni- and S-terminated surfaces with the latter being the thermodynamically more stable termination (Figure 40). However, surface reconstruction was theoretically observed with permanent change of the active surface which is as well in line with experimental data. After stability testing for six-hours at -10 mA cm<sup>-2</sup>, the morphology of Ni<sub>3</sub>S<sub>2</sub> changed considerably accompanied by a decrease in catalytic performance. In literature, the electrocatalytic performance of Ni<sub>3</sub>S<sub>2</sub> towards the HER is controversially discussed. Supporting our earlier mentioned experimental results, Ni<sub>3</sub>S<sub>2</sub> was found to be unstable in acid where leaching into solution occurs, thus, shaping up Raney nickel related coatings[62, 133, 134, 135] (reported exception: [250]). In alkaline as well as in neutral solutions, however, high stability and performance were reported in literature[225, 251, 252, 253] (reported exception: [133]). However, long-term stability measurements and post-characterizations of the catalysts were often missing. From the results on hand, it is concluded that Ni<sub>3</sub>S<sub>2</sub> is also unstable in alkaline solution due to changes in morphology (Figure 39), constant decrease during chronopotentiometry measurements and reconstruction observed from theoretical calculations. PXRD still shows characteristic Ni<sub>3</sub>S<sub>2</sub> reflections after testing (not shown here). Nevertheless, this only means that Ni<sub>3</sub>S<sub>2</sub> is simply too thick to be completely converted during the six-hour test or that on-top deposited nickel acts as a barrier against further dissolution.

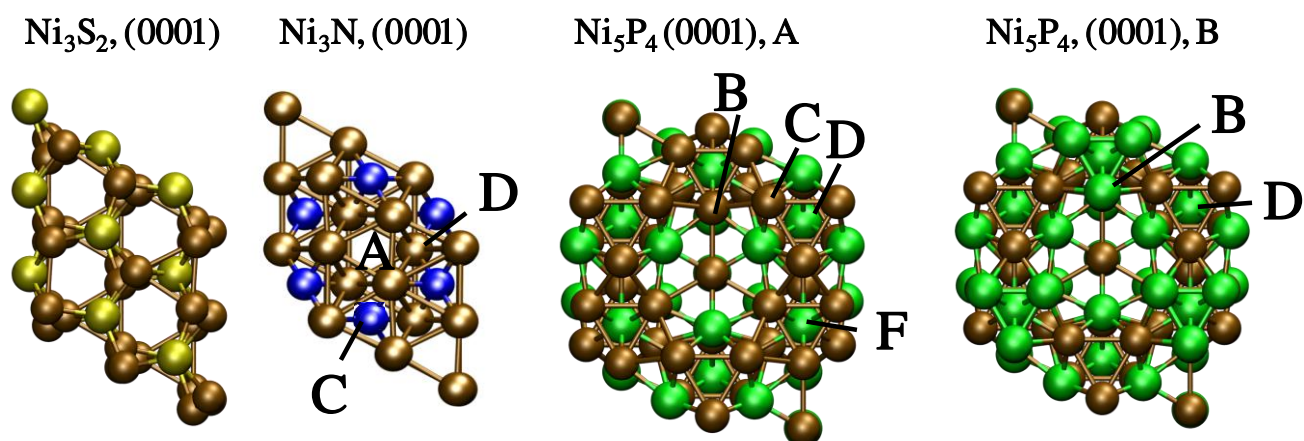


Figure 40: Crystal structures of  $\text{Ni}_5\text{P}_4$ ,  $\text{Ni}_3\text{S}_2$  and  $\text{Ni}_3\text{N}$  in (0001) termination. Possible adsorption sites are indicated. Brown: nickel, green: phosphorous, blue: nitrogen, yellow: sulfur. Adapted from [217]. As reconstruction of the surface was experimentally and theoretically observed for  $\text{Ni}_3\text{S}_2$ , details about possible adsorption sites were omitted.

When taking only theoretical calculations into account,  $\text{Ni}_3\text{S}_2$  appears on top of the volcano. However, due to the instability discussed before, the active catalyst consists most likely of nickel on top of  $\text{Ni}_3\text{S}_2$  deposited at low potentials when  $\text{S}^{2-}$  is leaching into solution ( $\text{Ni}^{2+} + 2e^- \rightleftharpoons \text{Ni}$  at -0.257 V vs. SHE, [254]). The catalytic behavior of  $\text{Ni}_3\text{N}$  on the other hand is expected to differ in comparison to pristine nickel due to lattice dilation of the host matrix by interstitial nitrogen.

Similar to  $\text{Ni}_3\text{S}_2$ , two surface terminations of the (0001) surface were taken into account for  $\text{Ni}_3\text{N}$ : N- and Ni-terminations (Figure 40). In contrast to  $\text{Ni}_3\text{S}_2$ , it was found that the nickel terminated surface was stabilized, not the heteroatom terminated one. For the N-terminated surface, adsorbed ammonia is very likely to form, to be released, and, due to the layered structure, the newly shaped surface is in effect again Ni-terminated. Therefore, only Ni-terminated surfaces were considered in the following discussion. In this configuration, it was found that due to the more complex crystal structure, various surface sites evince different hydrogen affections. The most probable and energetic favored adsorption sites lie in between the nickel triangle (A, D) and on nitrogen (C) in Figure 40. Experimentally, the morphology before and after stability testing changes only insignificantly and only slight changes in current density

were observed (Figure 39). Similar to pristine nickel, the performance of  $\text{Ni}_3\text{N}$  even increases slightly with the passage of time, presumably due to other surface processes as e.g. reduction of oxide layers taking place. One reason for the higher catalytic behavior may lie in the layered structure where nitrogen is interstitially incorporated. After ammonia removal, dense nickel terminations promote stable behaviour in alkaline media. Similar to stress or strain induced lattice dilation from underlying heterometals,[255, 256, 257] underlying nitrogen increases the unit cell parameters and induces changes in adsorbate binding energies. As remarked in the beginning of this chapter,  $\text{Ni}_3\text{N}$  can also be obtained by means of urea, a practical choice due to its easy handling.[240] Hereby, nickel nitride nanoparticles are stabilized by carbon layers formed *in-situ* during synthesis. However,  $\text{Ni}_3\text{N}$  obtained from the urea-glass route at low temperatures did not result in high activity presumably due to thick carbon layers surrounding the active catalyst as observed for Ni/Mn@C in chapter 3. Nevertheless,  $\text{Ni}_3\text{N}$ 's isotopic equivalent  $\text{Fe}_3\text{N}$  was reported to be an active photocatalyst for the hydrogen evolution.[258]

As shown in chapter 5.3.1,  $\text{Ni}_5\text{P}_4$  exhibits stable behavior along with high activity towards the HER in base. However, its crystal structure is rather complex. The hexagonally packed crystal structure contains diverse surface sites which makes especially  $\text{Ni}_5\text{P}_4$  difficult to evaluate. In  $\text{Ni}_5\text{P}_4$ , preferential growth along the  $[10\bar{1}0]$  direction was observed. It was therefore assumed that the (0001) plane located perpendicular to the surface contributes the most to the electrocatalytic activity. Thus, theoretical calculations have been performed on the (0001) surface. As before, a detailed description of possible surface sites and calculated hydrogen adsorption energies can be found in [217]. However, two terminations were elaborated further, labeled as A and B in Figure 40. In termination B, hydrogen adsorption takes place at nickel (B) or on already adsorbed hydrogen on nickel (B) indicated in Figure 40. Readily hydrogen adsorption at nickel (D) was observed making it the energetic most stable

---

position, thus, playing presumably only a minor role in the hydrogen evolution. For site A, possible adsorption sites are rather difficult to predict since a strong coverage dependency was found. Possible adsorption sites with  $\Delta G$  close to 0 are located between two nickel atoms (B and C, bridged), on one side of the nickel triangle above phosphorous (F) and at phosphorous directly (C). Similar to site B, hydrogen is adsorbed relatively strongly to nickel (D), contributing supposedly only marginally to the overall activity. Despite all the possible adsorption sites, termination A is located further on top of the volcano than termination B predicting higher catalytic activity. Furthermore,  $\text{Ni}_5\text{P}_4$  demonstrated higher activity also experimentally compared to  $\text{Ni}_3\text{N}$  which was also obtained theoretically speaking for a high proportion of adsorption site A in comparison to B. However, different aspects should be kept in mind and are further elaborated. Other reasons for the high activity for  $\text{Ni}_5\text{P}_4$  in comparison to  $\text{Ni}_3\text{N}$  are

- the higher electrochemically active surface area of  $\text{Ni}_5\text{P}_4$  compared to  $\text{Ni}_3\text{N}$ ,
- the geometrically and electrochemically active surface area might not scale with the number of active sites since some facets might display higher activity than others as shown for  $\text{MoS}_2$  where edge sites are more active than basal plane sites,[35, 37]
- different morphologies and solvent interactions influencing the transport of reactants/products (it has been shown that the effect of molecular water on the adsorption is relatively small[216]),
- DFT calculations themselves display a certain error depending on the functional used,
- the interaction of underlying nickel might play a certain role as it is located on the left branch of the volcano and a synergetic effect may be expected.

Moreover, the operation mechanism might be different depending on the used material what further work has to shed light on. For instance, the reaction kinetics differ for the given materials and *Tafel slopes* obtained by current voltage extrapolation range between  $\sim 55\text{-}95\text{ mV dec}^{-1}$  for nickel phosphides, nitrides and sulfides.

Since  $\Delta G$  displays an intrinsic parameter, not accounting for the surface roughness or area, the geometrical current density was normalized to the electrochemically active surface area. The resulting graph is displayed in Figure 41. Here, nickel nitride assimilates in performance to platinum which was predicted by theoretical calculations. Nonetheless,  $\text{Ni}_5\text{P}_4$ 's activity reduces due to its high electrochemically active surface area compared to  $\text{Ni}_3\text{N}$  or Ni. It is noted that due to great differences in ECSA, other effects such as diffusion limitation or bubble formation may arise and can be misinterpreted for hydrogen evolution (low current density) or can limit the performance (high current density).

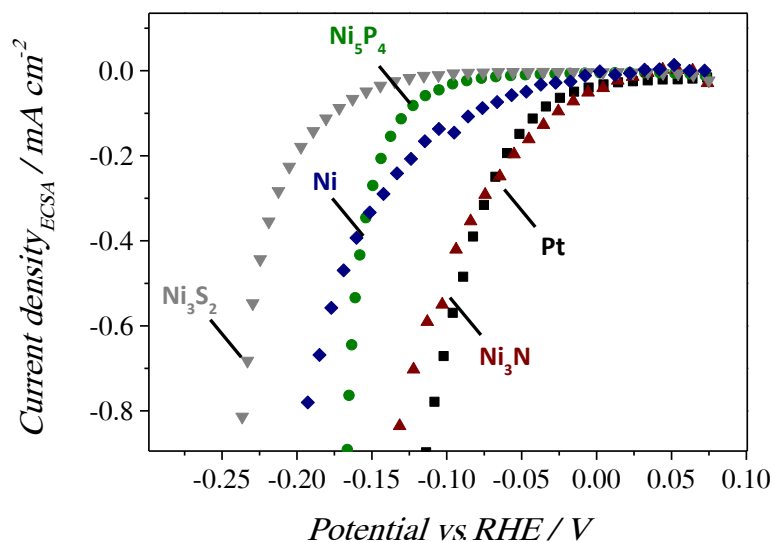


Figure 41: Current voltage characteristics extrapolated to the electrocatalytically active surface area.

As described in the previous chapter, the activity of  $\text{Ni}_5\text{P}_4$  towards the HER was drastically improved by directly modifying high surface area nickel foam. As proof of concept, nickel nitride's surface area was consequently increased by modifying nickel foam through ammonia treatment at  $400\text{ }^\circ\text{C}$  for 14 h. Thereby, higher surface area was achieved along with higher catalytic performance (Figure 42). Current densities up to  $100\text{ mA cm}^{-2}$  were realized at  $\sim 0.15\text{ V}$  overpotential in 1 M KOH. Thus,  $\text{Ni}_3\text{N}$  numbers among the best state-of-the-art electrocatalysts for the HER in alkaline medium. The corresponding SEM images before and after testing are shown in Figure 42. Low and high magnification SEM images further revealed homogeneous covering of  $\text{Ni}_3\text{N}$ . Hereby, hexagonal crystals can be observed at high magnification. From PXRD, the characteristic hexagonal  $\text{Ni}_3\text{N}$  reflections were obtained. Similar to  $\text{Ni}_5\text{P}_4$ , the modified foam was susceptible to breaking, thus, speaking for a change in bonding state with a higher covalent to metallic proportion than its metallic congener.

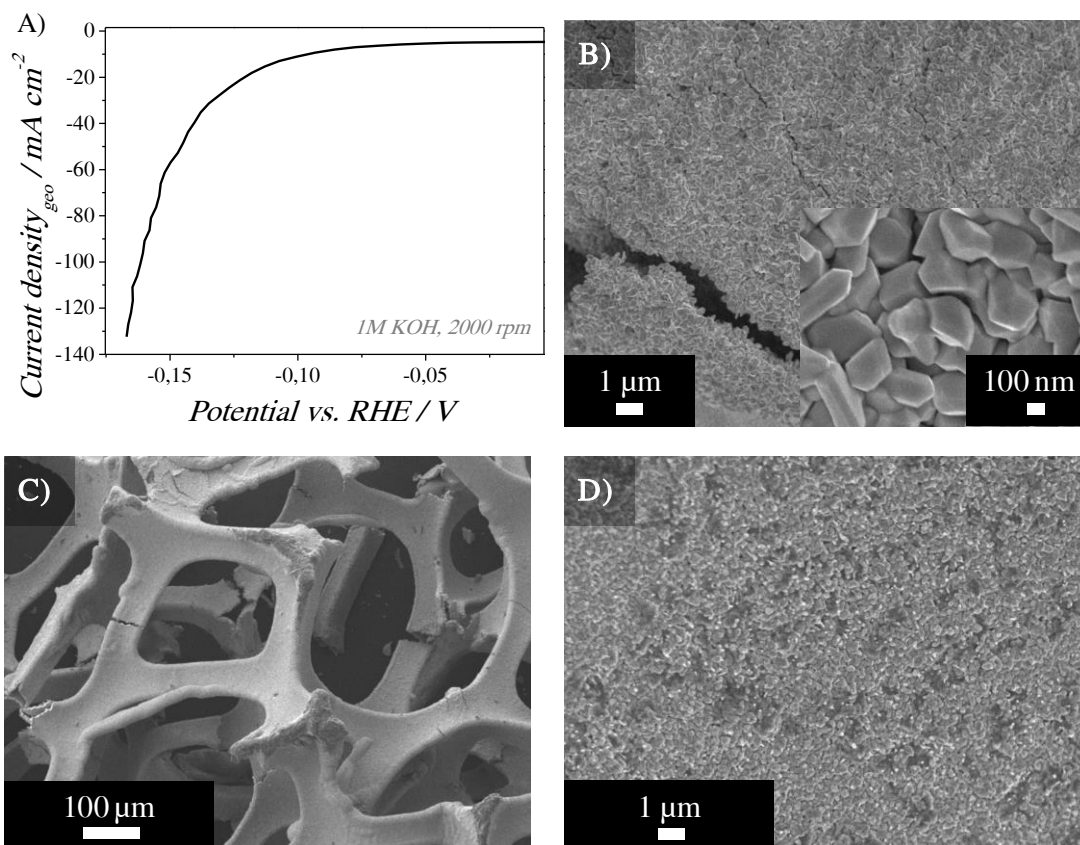


Figure 42: A) Current voltage characteristics of nickel nitride on nickel foam and the corresponding SEM image before (B, C) after (D) electrochemical testing. After modification of pristine nickel foam with  $Ni_3N$ , the foam darkened similar to  $Ni_3P_4$ .

## 6.4 Summary

The behavior of different heteroatom containing nickel alloys towards the HER was elucidated by experimental testing and theoretical calculations, and profound understanding of all presented materials has been gained. Hereby, this is the first, systematic study – to the best of the authors knowledge – where nickel is transformed into nickel sulfide, phosphide and nitride and evaluated theoretically and experimentally towards the HER. Up to now, most theoretical and experimental work was dedicated to pristine metals and data for heteroatom containing nickel alloys does not exist. However, nickel phosphide for instance shows a much higher activity towards the HER than pristine nickel in alkaline and acidic solution. Therefore, further

understanding was needed and trends had to be evaluated which was addressed in this chapter. Theoretical calculations performed by Hannah Schlott and Prof. Bernd Meyer underpin the experimental observations where non-metal elements incorporated into the nickel structure lead to new adsorption sites changing the catalyst's activity. The hydrogen adsorption Gibbs free energy was used as descriptor providing insights into possible adsorption sites. All presented results required stringent optimization of synthesis conditions, careful electrocatalytic testing and attention to detail during theoretical calculations. Strong site-dependency of  $\Delta G$  was revealed and has been observed also only recently in transition metal phosphides insinuating inherent differences to their pristine transition metals counterparts.[36] A Volcano-like relationship was established depending on the heteroatom and the evolving crystal structure. As nickel is located on the left branch of the volcano, a shift towards preferential binding was observed for all materials. Interestingly,  $\text{Ni}_3\text{S}_2$  possesses theoretically almost ideal hydrogen adsorption energy as well as high exchange current density but lacks in stability. Given these insights, stabilization and protection of  $\text{Ni}_3\text{S}_2$  (0001) facets should be the logical focus in the future for assimilation of Pt-like behavior towards the HER. In a similar manner, further research on structuring  $\text{Ni}_5\text{P}_4$  with more surface exposed and active terminations A may increase even further the electrocatalytic performance. From theoretical calculations,  $\text{Ni}_5\text{P}_4$  was found on top of the volcano followed by  $\text{Ni}_3\text{N}$  with hydrogen adsorption energies close to zero. However, when taken the electrochemically active surface area into account,  $\text{Ni}_3\text{N}$  assimilates to platinum behavior predicted from DFT calculation. As proof of concept, high surface area nickel foam was modified with  $\text{Ni}_3\text{N}$  on top with increased amount of active sites, thus, leading to enhanced performance towards the HER. Even though DFT calculations display a feasible approach to predict catalytic performance, real life systems encompass different factors (surface area, morphology, solvent interactions, defects...) that should not be underestimated and

– if possible – have to be accounted for. Nevertheless, sources of errors were minimized and the presented results display a further step towards cost-efficient, earth abundant and highly efficient catalysts that potentially compete with noble metals as platinum in the hydrogen evolution reaction.

## 7 Conclusions and perspectives

---

The growing need for sustainable energy storage was the fundamental motivation of the thesis on hand. As hydrogen displays a highly attractive energy carrier and intermediate in the production of other practical fuels/chemicals, the focus was laid on the electrocatalytic water splitting reaction to obtain hydrogen. In order to breathe life into this technology, cost-efficient, scalable and efficient catalysts are indispensable. As both, the hydrogen and oxygen evolution reactions are still taking place well away from the equilibrium potential, both reactions were studied in detail. In this manner, the conceptual elucidation of palpable precepts was shown in detail to target the development of state-of-the-art catalysts for full water splitting. The preparation and evolution of Mn-, N-, S-, P-, C-containing nickel alloys were introduced, accompanied by theoretical and experimental elucidation of their activity towards the HER and OER. As a fundamental tenet, two pathways were chosen to enhance the electrocatalytic performance. The first encompasses the direct amelioration of intrinsic properties through appropriate material selection. Thereby, new and unexplored materials such as Ni<sub>5</sub>P<sub>4</sub>, Ni<sub>3</sub>N or Ni/Mn@NDC towards the HER and OER were examined. The second was based on increasing the surface area of the catalytic material with an increased amount of active sites. Here, both strategies could be combined. In order to obtain an increased amount of active sites, the active catalytic material has to either possess a high surface area by itself or must be anchored onto a high surface area support.

Based on these ideas, support as well as active catalysts were synthesized in chapter 3 in a single step from readily available starting materials. Nickel/manganese nanoparticles were created *in-situ* while high porosity carbon support was attained using salt mixtures concurrent as the template and as the reaction medium. Hereby,

---

nitrogen was found to be the reducing agent for nickel whereas the molten state of the salt provided the high surface area. On the basis of the described one-step doctrine, the straightforward and facile preparation of nickel phosphides, sulfides and nitrides on nickel foil/foam was elucidated in chapter 5 and 6. Clearly, the advantage of this pathway lies in the scalable preparation from easily obtained materials and the moderate temperatures employed. Especially attractive seems the conversion of high surface area nickel foam with outstanding catalytic behavior towards the HER. However, not only “technical” factors such as the catalyst’s high catalytic performance and easy preparation were highlighted, but also a deeper understanding of growth, inherent properties and kinetic parameters of the catalytic material were gained. Furthermore, advanced catalysts displaying alluring intrinsic properties such as hardness, corrosion resistance in acidic and basic medium, and high performances towards the HER were designed. By systematically pursuing the concept of *Sabatier’s principle*, readily tuning of catalytic sites was demonstrated. Exemplarily, the catalytic performance was affected positively towards the HER when manganese – binding hydrogen loosely – was combined with nickel – binding hydrogen tightly (chapter 3) – thus unveiling the synergetic effect of both metals. In the same manner, theoretical, material and electrochemistry were dovetailed, and insights of possible hydrogen adsorption sites for nickel sulfides, nitrides and phosphides were gained. It was shown that nickel terminated facets in the  $\text{Ni}_3\text{N}$  structure provide the active sites rather than the nitrogen termination. Hereby, the adsorption energy is positively shifted due to lattice dilation of underlying nitrogen atoms. By systematically bringing materials with optimized hydrogen adsorption free energy onto high surface area support, catalytic performances approaching the golden standards of noble metals were feasible. Distinct hydrogen adsorption sites on  $\text{Ni}_3\text{N}$ , accomplished through DFT calculation, effectively led to high electrocatalytic performance towards the HER (chapter 6). In the same manner, its isotopic counterpart, nickel carbide – featuring slightly larger

---

carbon interstitially incorporated in the metallic nickel scaffold – was synthesized in the form of nanoparticles with high surface area. In contrast with the simplicity of only one synthesis step employed, multiple-step preparation offers the ascendancy of tailoring every preparation step separately. The active catalyst ( $\text{Ni}_3\text{C}$ ) was prepared independently and anchored onto an inert carbon support with high surface area. In this manner, an easy-to-handle synthesis strategy was chosen, offering higher scale-up possibilities. Instead of creating a burst nucleation through hot injection of reactants into the reaction medium, the synthesis was conducted in a temperature ramping fashion. Due to stabilization through oleylamine ligands, the nucleation was delayed, leading to small nanoparticles with homogeneous size distribution. It was withal possible to elucidate the growth and evolution of other materials described in this thesis. Nickel carbide growth for instance followed *Ostwald's rule of stages*, where in the beginning formed, amorphous nickel nanoparticles were subsequently transformed in crystalline cubic nickel and hexagonal  $\text{Ni}_3\text{C}$  nanoparticles. Moreover, supported nickel phosphide growth is presumably dominated by grain boundary diffusion instead of charged ion diffusion and a three-layered structure consisting of Ni,  $\text{Ni}_{12}\text{P}_5$ , and  $\text{Ni}_5\text{P}_4$  was observed. The anisotropic unit cell of  $\text{Ni}_5\text{P}_4$  led to the growth of plates along the  $[10\bar{1}0]$  direction. The growth was spatially confined through impinging plates, leading to growth of hexagons perpendicular to the substrate's surface.

In contrast to directly grown nickel phosphide on existing support, carbide particles were anchored onto high surface area carbon paper and the surrounding organic ligands removed, leaving active sites free for access. As the preparation of each catalyst's subpart was optimized, current densities over  $100 \text{ mA cm}^{-2}$ , at necessary overpotentials lower than 0.2 V, could be achieved along with long-term stability in alkaline medium. In contrast thereto, manganese-doped nickel particles embedded into high surface area support offered the advantage of preparation simplicity owing

to a lower number of necessary synthesis steps (chapter 3). However, despite the ease of preparation, the carbon surrounding the metallic nanoparticles was boon and bane at the same time. The small nanoparticles were stabilized, further growth prevented, and high surface area to volume ratio was achieved. However, blocking of active sites was rather derogatory for high oxygen evolution. The carbon shell was blocking the transformation to active nickel oxide material during the oxygen evolution. Similar to nickel carbide nanoparticles where blocking ligands were removed in order to vacate active sites, benign oxidation led to higher accessibility of active sites. Hereby, the post-annealed catalyst demonstrated increased accessibility of reactants and products to the active metal centers, while keeping the morphology and porosity intact. As nickel phosphide ( $\text{Ni}_5\text{P}_4$ ) was brought directly onto the substrate, the problem of blocked active sites became redundant and was not encountered. In this manner, the in-depth assessment of nickel phosphide transformation during OER revealed  $\gamma$ -NiOOH and  $\beta$ -NiOOH formation depending on the conditions used. In this context, it is the first time – to the best of the authors knowledge – that evidence is provided in favor of the transformation of  $\text{Ni}_5\text{P}_4$  into an amorphous, highly active nickel oxyhydroxide based catalyst towards the OER. Similarly, the possible transformation of other transition metal alloys such as sulfides, nitrides or selenides – reported as true catalyst in literature – during the OER should be taken into account. Additionally, all synthesis strategies offer their conveniences for distinct application fields. The direct modification of already existing support is highly attractive for industrial processes where scalability, efficiency, easy handling and cost-efficiency are irremissible. Nevertheless, the catalyst is subjected to high current densities (several  $\text{A cm}^{-2}$ ), emphasizing the need for improved inherent properties such as a low *Tafel slope*. Especially  $\text{Ni}_5\text{P}_4$  demonstrated high efficiency and stability in acidic environment accompanied by a low *Tafel slope* of  $40 \text{ mV dec}^{-1}$ , which is close to that of platinum. The electrocatalytic water splitting reaction only touches one aspect of

---

the spacious range of applications for transition metal phosphides which is waiting for the  $\text{Ni}_5\text{P}_4$  nanostructure system.  $\text{Ni}_3\text{C}$  nanoparticles are proposed for photoelectrocatalysis, where a low *Tafel slope* is not coercively necessary as are other factors such as e.g. the tunability of layer thickness. It can be used as cathode material for photovoltaic devices where the sensitive deposition onto photoabsorber material is mandatory. As the particles are in the size range of 35 nm and dispersed in solution, the catalyst thickness can theoretically be optimized separately, so that a sufficient amount of light can reach the semiconductor whilst maintaining its catalytic activity.

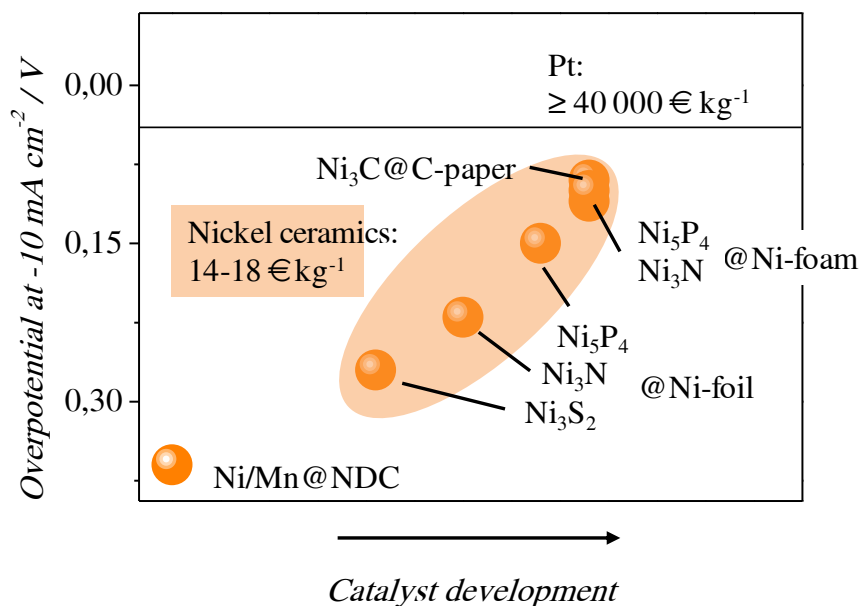


Figure 43: Schematic development of catalysts described in the thesis on hand benchmarked on the necessary overpotential at  $-10 \text{ mA cm}^{-2}$  towards the HER. The platinum standard is indicated as black line with costs over  $40,000 \text{ € kg}^{-1}$ . Nickel carbides, sulfides, phosphides and nitrides (shaded in orange) assimilate in performance towards platinum at much lower costs.

Clearly, much effort has been undertaken to challenge platinum-like behavior in terms of efficiency and long-term stability towards the hydrogen evolution reaction. Nevertheless, it was shown that many materials evaluated in this thesis demonstrated the compatibility of these two key-points accompanied by much lower costs. Figure 43 shows the systematic catalyst development during the thesis on hand

benchmarked at the overpotential of  $-10 \text{ mA cm}^{-2}$  for the HER. Moreover, a simplified calculation of catalyst costs (euro  $\text{kilo}^{-1}$ ) was performed. The calculation details can be found in the appendix. In this manner, the following prices for the presented materials and noble metal standards were obtained: Ni:  $\sim 20 \text{ € kg}^{-1}$ ,  $\text{Ni}_3\text{S}_2$ :  $\sim 15 \text{ € kg}^{-1}$ ;  $\text{Ni}_3\text{N}$ :  $\sim 18 \text{ € kg}^{-1}$ ;  $\text{Ni}_5\text{P}_4$ :  $\sim 14 \text{ € kg}^{-1}$ ; Pt:  $\sim 42,228 \text{ € kg}^{-1}$ ; Pd:  $\sim 24,339 \text{ € kg}^{-1}$ ; Ru:  $\sim 1,965 \text{ € kg}^{-1}$ ; Ir:  $\sim 16,803 \text{ € kg}^{-1}$ . Clearly, platinum is more than two thousand times more expensive than for instance nickel. On a mole basis, nickel is even more cost-efficient. Combined with readily available nonmetals such as phosphorous, carbon or nitrogen, even lower prices are obtained. Even though no material has yet demonstrated superior behavior towards the HER than platinum, the investment cost for electrolyzers is a central criterion. Eminently, the use of precious metals in new, evolving technologies is being impeded on a large scale due to their high cost, and higher availability of cost-efficient catalyst materials is utterly desirable. Future research will be required to further tackle the challenge to evaluate the durability of these materials over months or even years. As the cathodic reaction of the water splitting reaction is also employed in the chloralkali process, electrolysis costs can be reduced by using the here described materials. Furthermore, research concerning the applicability under real-world conditions – e.g. neutral pH, waste water, etc. – is still pending and has to be undertaken in the years to come. However, the presented results suggest that nickel nitrides, carbides and phosphides demonstrate the ability to approach noble metal standards towards the HER in a much more cost-efficient manner by using abundant and low-cost precursors.

## 8 Appendix

---

### 8.1 Abbreviations

Acac	Acetylacetonate
Bp	Boiling Point
BET	Brunauer-Emmet-Teller
BVE	Butler-Volmer Equation
CA	Chronoamperometry
C <sub>DL</sub>	Double Layer Capacitance
CE	Counter Electrode
CP	Chronopotentiometry
CV	Cyclic Voltammetry
DCDA	Dicyanodiamide
Deg	Degree
DeNO <sub>x</sub>	NO <sub>x</sub> Reduction
(NL)DFT	Non Local Density Functional Theory
EA	Elemental Analysis
ECSA	Electrochemically Active Surface Area
EDX	Energy-dispersive X-ray Spectroscopy
EELS	Electron Energy Loss Spectroscopy
Fcc	Face Centered Cubic
FT-IR	Fourier Transform Infrared Spectroscopy
GDP	Gross Domestic Product
HAADF-STEM	High Angle Annular Dark Field - Scanning Transmission Electron Microscopy

H <sub>ad</sub>	Adsorbed Hydrogen
H <sub>cp</sub>	Hexagonal Closed Packed
HER	Hydrogen Evolution Reaction
HR(SEM)	(High Resolution) Scanning Electron Microscope
HR(TEM)	(High Resolution) Transmission Electron Microscope
ICDD	International Centre for Diffraction Data
ICP-OES	Inductively Coupled Plasma Optical Emission Spectrometry
LSV	Linear Sweep Voltammetry
M	Metal
M <sub>p</sub>	Melting Point
NDC	Nitrogen-doped Carbon
ODE	1-Octadecene
OA	Oleylamine
OER	Oxygen Evolution Reaction
ORR	Oxygen Reduction Reaction
P	Phosphorous
P <sub>pmv</sub>	Parts per Million by Volume
PPP	Purchasing Power Parity
PXRD	Powder X-Ray Diffraction
R <sub>ct</sub>	Charge Transfer Resistance
RDE	Rotating Disk Electrode
RDS	Rate Determining Step
RE	Reference Electrode
RHE	Reversible Hydrogen Electrode
RT	Room Temperature
SAED	Selected Area Electron Diffraction

SCE	Saturated Calomel Electrode
TAA	Thioacetamide
TGA	Thermogravimetric Analysis
Toe	Tons of Oil Equivalent
V <sub>oc</sub>	Open-Circuit Potential
WE	Working Electrode
Wt%	Weight Percent
X@Y	Compound X loaded/grown on Compound Y
XPS	X-Ray Photoelectron Spectroscopy

## 8.2 Chemicals and materials

Thioacetamide (TAA, Sigma Aldrich,  $\geq 99.0\%$ ), red phosphorous (Sigma Aldrich,  $\geq 97.0\%$ ) and  $\text{NH}_3$  (Air liquide) was used as received. Nickel foil was purchased from Sigma (thickness: 0.125 mm,  $\geq 99.9\%$ ) and sonicated for five minutes in acetone and ethanol. Platinum disks were purchased from Goodfellow (diameter: 10 mm, thickness: 0.125 mm, 99.95%). Nickel foam was obtained from MTI cooperation (porosity:  $\geq 95\%$  (80-110 pores per inch; average hole diameters: 0.25 mm; surface density:  $346 \text{ g m}^{-2}$ )) was sonicated and washed for five minutes in acetone and ethanol prior to modification. Carbon paper 2050A was obtained from Spectracarb™ (30\*30\*0.254 cm; resistivity:  $18 \text{ m}\Omega \text{ cm}^2$  (through plane),  $5.4 \text{ m}\Omega \text{ cm}$  (in plane)). Stock solutions of oleylamine (70%, Aldrich) and 1-octadecene (90%, Aldrich) were prepared by degassing in vacuo for 24 h at  $120 \text{ }^\circ\text{C}$ . Nickel(II) acetylacetonate (5 g, Aldrich), manganese chloride ( $\text{MnCl}_2$ , Acros), nickel chloride ( $\text{NiCl}_2$ , Aldrich), lithium chloride ( $\text{LiCl}$ , Roth) and dicyandiamide (DCDA, Aldrich) were used as received.

### 8.3 Experimental part

#### Chapter 3: Nickel and manganese based materials embedded into highly porous nitrogen-doped carbon for the tunable electrocatalysis of HER and OER

##### Synthesis

Sample	MnCl <sub>2</sub>	NiCl <sub>2</sub>	LiCl	DCDA	FeCl <sub>2</sub>	CoCl <sub>2</sub>
Mn <sub>0</sub> Ni <sub>1</sub>	0	1	2	0.5	0	0
Mn <sub>0.1</sub> Ni <sub>1</sub>	0.1	1	2	0.5	0	0
Mn <sub>0.5</sub> Ni <sub>1</sub>	0.5	1	2	0.5	0	0
Mn <sub>1</sub> Ni <sub>1</sub>	1	1	2	0.5	0	0
Mn <sub>1</sub> Ni <sub>0.5</sub>	1	0.5	2	0.5	0	0
Mn <sub>1</sub> Ni <sub>0.1</sub>	1	0.1	2	0.5	0	0
Mn <sub>1</sub> Ni <sub>0</sub>	1	0	2	0.5	0	0
Fe <sub>1</sub> Ni <sub>0</sub>	0	0	2	0.5	1	0
Co <sub>1</sub> Ni <sub>0</sub>	0	0	2	0.5	0	1

Table S1: Molar ratios of used precursors and the respective sample denotation.

The synthesis was adapted from Shalom and coworkers.[80] In Table S1, the molar ratio of the mixed salts and organic precursors are indicated. All materials were mixed, thoroughly grinded and heated up first to 400 °C for 6 h (40 K min<sup>-1</sup>) and then to 800 °C for 10 h (40 K min<sup>-1</sup>) in an inert atmosphere (N<sub>2</sub>). The salt was removed by grinding the black product followed by washing with water for 24 h. After filtration in vacuo and washing with water and ethanol, the product was dried at 50 °C for a few hours. The alteration of the electrochemical properties was achieved by heating up all samples to 300 °C for 10 h with a heating ramp of 30 K min<sup>-1</sup>. The best OER performance catalyst was selected for further oxidation studies by changing the heating time to 3 h and 15 h, respectively.

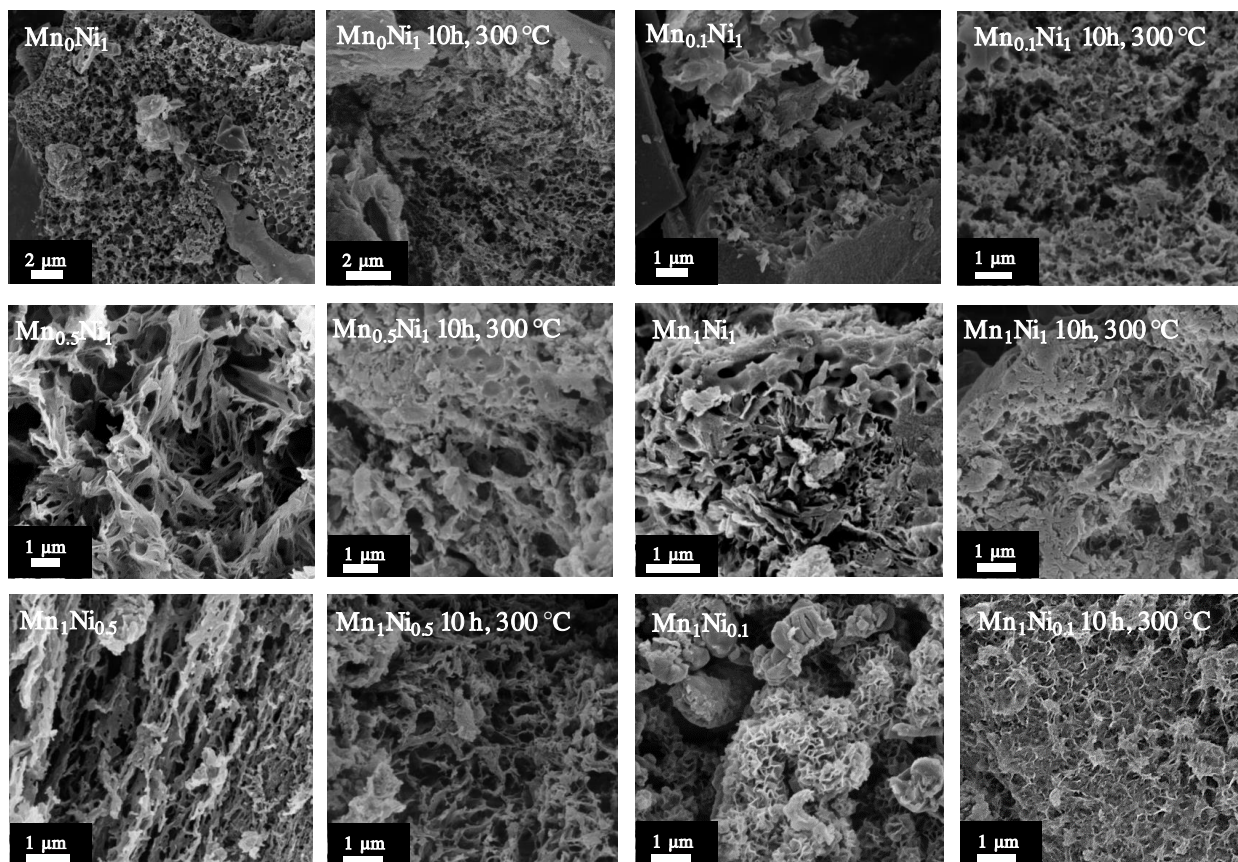


Figure S1: SEM image of  $Mn_xNi_y$  directly after synthesis and after thermal treatment at 300 °C for 10 h.

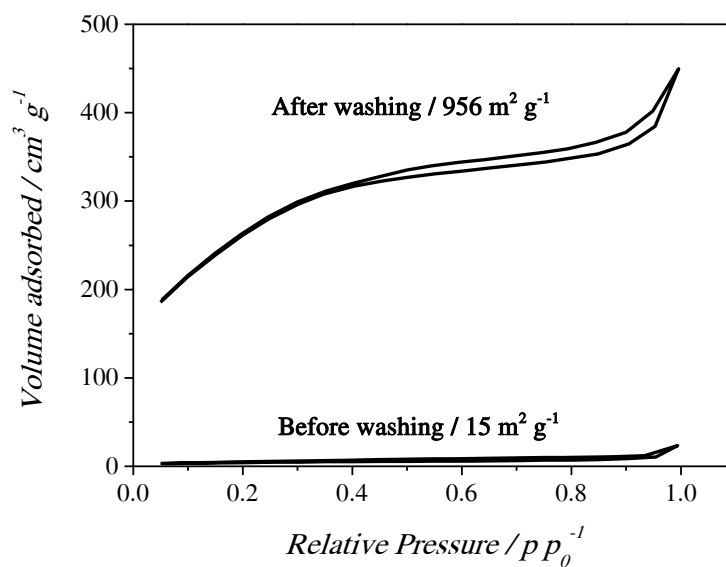


Figure S2: Nitrogen sorption isotherm after synthesis of  $Mn_0Ni_1$  at 800 °C before and after washing with water for 24 h.



Figure S3: SEM images of  $\text{MnCl}_2$  (1),  $\text{CoCl}_2$  (1) and  $\text{FeCl}_2$  (1) mixed with  $\text{LiCl}$  (2) /  $\text{DCDA}$  (0.5) and heated up to  $800^\circ\text{C}$ . The numbers in brackets display the molar ratio of the used compounds.

For ICP-OES, a SISTA-MPX (Varian) instrument was used with wavelengths of 257.61 / 259.37 nm for manganese and 216.55 / 231.60 nm for nickel. A FEI TITAN microscope equipped with a post column EELS spectrometer (GATAN Tridiem) provided TEM, EELS, STEM and EDX images. Prior to the measurements, the sample dispersion in chloroform was deposited onto holey carbon copper grids. The operational voltage was 300 V. A LEO 1550-Gemini instrument provided SEM images (acceleration voltage of 5 kV). 5 mg of catalyst was dispersed in 95  $\mu\text{l}$  of ethanol and 5  $\mu\text{l}$  of Nafion<sup>®</sup> by sonication for 30 min. An aliquot of 5  $\mu\text{l}$  was deposited onto a polished glassy carbon electrode (0.2  $\text{cm}^2$ ). The sample were dried at  $50^\circ\text{C}$  until a homogeneous film was observed. The  $iR$  drop ( $i$  = current;  $R$  = ohmic resistance) of the measured potential-current curves was corrected by high frequency impedance. The used frequencies ranged between 0.1 Hz and 1 kHz whereby high frequencies were used for determination of the solution resistance (in our setup  $\sim 45\ \Omega$ , 0.1 M KOH). A three electrode setup was used and all measurements were performed in 0.1 M KOH. A saturated calomel electrode served as reference electrode, a platinum wire as counter electrode. Since rotation at higher speed (2,000 rpm) resulted in detachment of the catalyst, the working electrode was rotated at 400 rpm.

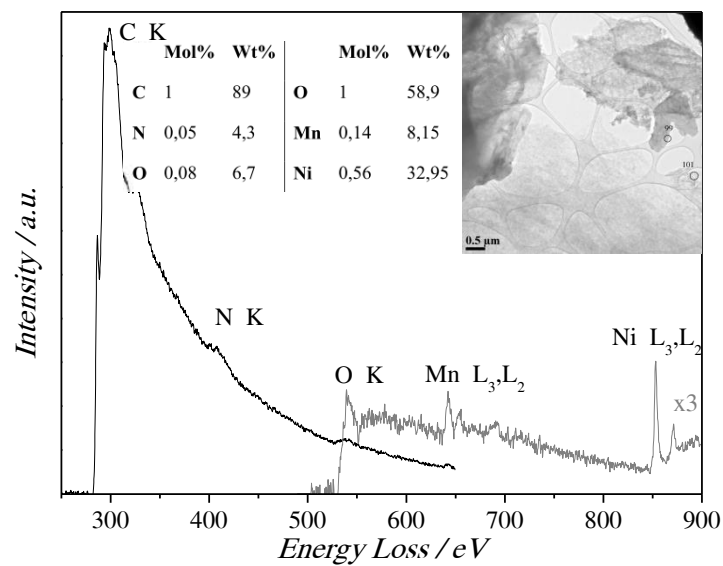


Figure S4: EELS of  $Mn_1Ni_1$  directly after synthesis where the analyzed area is indicated as #99.

Sample	Surface area ( $m^2 g^{-1}$ )	Average pore radius (nm)
$Mn_0Ni_1$	950	1.4
$Mn_{0.1}Ni_1$	800	1.6
$Mn_{0.5}Ni_1$	950	1.5
$Mn_1Ni_1$	980	1.6
$Mn_1Ni_{0.5}$	970	1.6
$Mn_1Ni_{0.1}$	60	5.2
$Mn_1Ni_0$	30	6.6

Table S2: Surface area and average pore radius for all  $Mn_xNi_y$  samples.

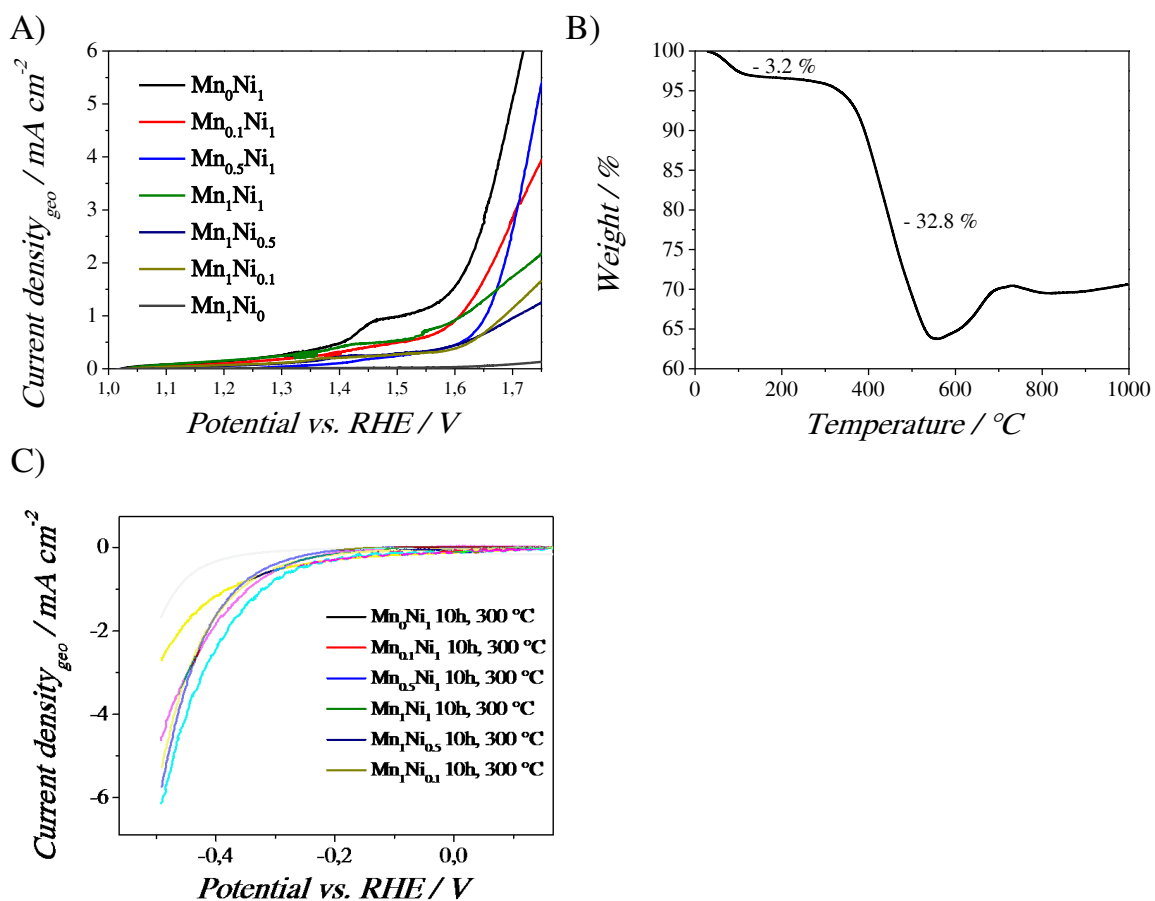


Figure S5: OER performance directly after synthesis (A) and HER performance after 10 h at 300 °C under air (C) of Mn<sub>x</sub>Ni<sub>y</sub> in 0.1 M KOH and rotation of the working electrode at 400 rpm. B) The temperature was chosen according to TGA measurements in air.

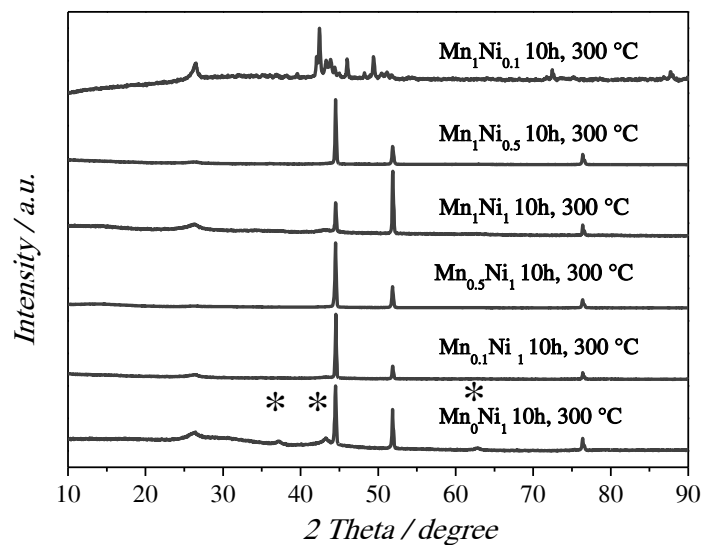


Figure S6:  $Mn_xNi_y$  after oxidation at 300 °C for 10 h. Characteristic NiO reflections are indicated with a star (111, 200, 220; ICDD: 04-013-0890).

Sample	Surface area ( $m^2 g^{-1}$ )	N [wt%]	C [wt%]
$Mn_{0.1}Ni_1$ after synthesis	800	5	42
$Mn_{0.1}Ni_1$ , 3 h, 300 °C	880	5	43
$Mn_{0.1}Ni_1$ , 10 h, 300 °C	1,200	4	43
$Mn_{0.1}Ni_1$ , 15 h, 300 °C	250	2	11

Table S3: Surface area obtained from nitrogen sorption, carbon and nitrogen content from elemental analysis after activation of  $Mn_{0.1}Ni_1$  at 300 °C for different time intervals.

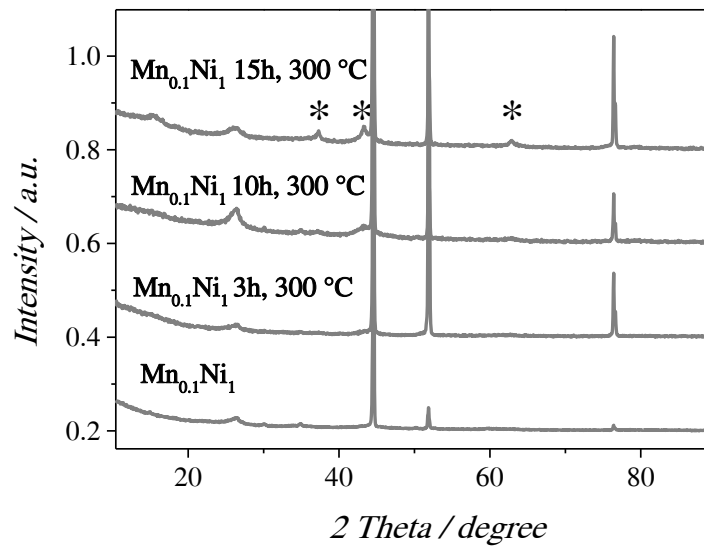


Figure S7: PXRD of  $Mn_{0.1}Ni_1$  at 300 °C in air for different time intervals. Characteristic NiO reflections are indicated with a star (111, 200, 220; ICDD: 04-013-0890)

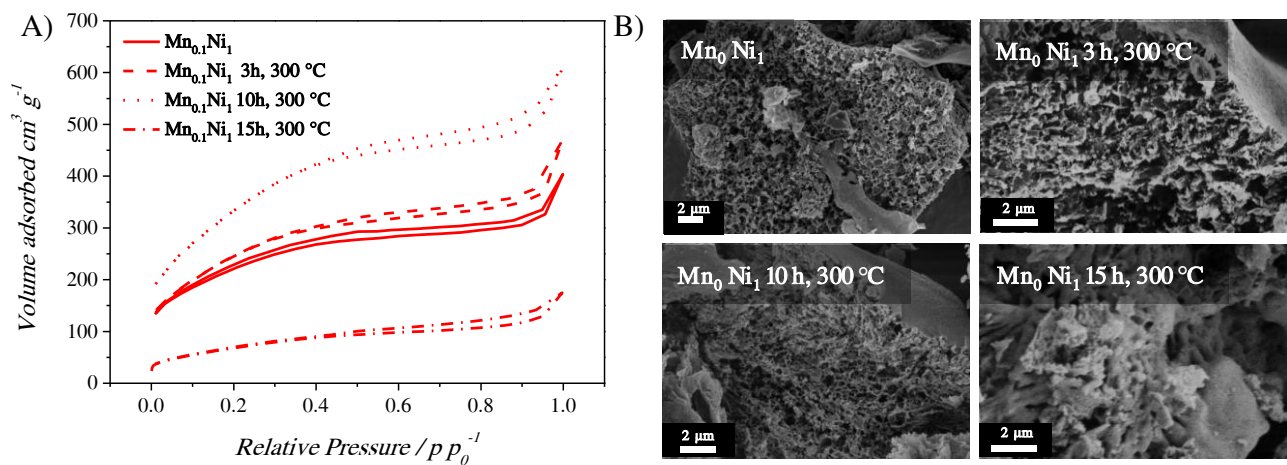


Figure S8: A) Nitrogen sorption isotherms of  $Mn_{0.1}Ni_1$  after different time intervals keeping the temperature constant at 300 °C and (B) the corresponding SEM images.

## **Chapter 4: Ni<sub>3</sub>C nanoparticle formation and its electrochemical performance towards the hydrogen evolution reaction**

### **Synthesis**

Nickel acetylacetonate (250 mg, 1 mmol), 1-octadecene (6.4 ml, 20 mmol) and oleylamine (4.6 ml, 14 mmol) were added to a 100 ml three neck round bottom flask equipped with a condenser and a septum. A glass covered magnetic stir bar was used. The flask was heated to 100 °C under rigorous stirring and set under vacuum for three hours. After backfilling with nitrogen, the flask was heated to 320 °C and aliquots were taken in different time intervals through a metallic tube by means of applied overpressure. The heated flask at 100 °C after three hours was set as absolute point  $t = 0$  s. First, the solution exhibited green color. With increasing time, blackening occurred along with formation of white fume. After cooling down, the black solution was centrifuged at 7,500 rpm for 30 min. The supernatant was removed, the precipitate dispersed in ethanol/hexane (1:3 vol%) and again centrifuged. This washing step was repeated three times and the precipitate collected in hexane for storage. Usually, around 40-50 mg of final product was obtained.

### **Preparation for electrocatalysis**

First, a stock solution of 0.46 mg ml<sup>-1</sup> of Ni<sub>3</sub>C in hexane was prepared. Carbon paper with a diameter of 1 mm was put on a glass slide which was heated to 100 °C. Afterwards, 5 ml of Ni<sub>3</sub>C stock solution was dropcasted and the solvent evaporated. In order to remove the organic oleylamine ligands that are capping the nanoparticle surface, Ni<sub>3</sub>C@carbon paper was heated to 350 °C for 3 h in 5% H<sub>2</sub>/Ar.

## **Chapter 5: Evolution of nanostructured Ni<sub>5</sub>P<sub>4</sub> and its use as cost-efficient bifunctional electrocatalyst towards the HER and OER**

### **Synthesis of Ni<sub>5</sub>P<sub>4</sub> on nickel foil**

Due to the nature of red phosphorous, the synthesis should be carried out only by appropriately trained personal in air-free atmosphere. Friction and higher temperatures will cause ignition and careful handling is mandatory. 400 mg of red phosphorous and cleaned nickel foil (20\*20 mm) was introduced into a 100 ml three neck-round bottom flask. Afterwards, the system was evacuated three times and set under nitrogen. The flask was heated up to 550 °C (0.9 K s<sup>-1</sup>) for different time intervals in a high temperature heating mantel. At around 420 °C, phosphorous started to sublime and phosphorous deposition on the colder upper side walls of the vessel was observed. By removing the heating mantel at certain time intervals followed by fast quenching through nitrogen, the growth mechanism was studied. The time intervals are indicated in the main text. After the reaction, the foil was taken out after cooling to RT and was sonicated in distilled water for one minute in order to mechanically remove excess phosphorous. A mass gain of 13.9 mg was observed due to the formation of nickel phosphide. In order to modify nickel foam, 400 mg of red phosphorous was provided to a 100 ml three necked flask, nickel foam (20\*20 mm) was put on top, and the same synthesis steps as for nickel foil were applied. The only difference was the reduced heating time of 20 min since Ni<sub>2</sub>P phases in PXRD appeared after longer heating times.

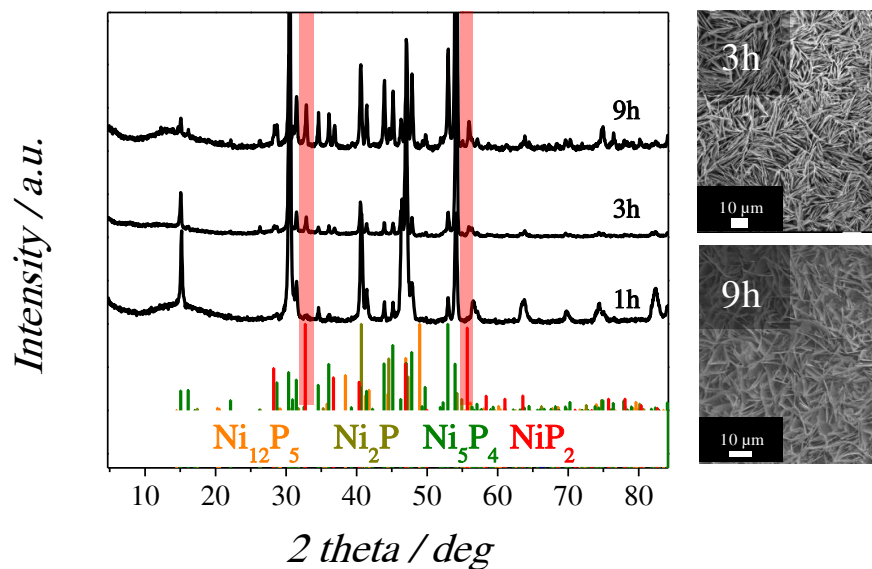


Figure S9: PXRD pattern of longer reaction times of nickel foil with red phosphorous (one hour, three hours and nine hours) and the corresponding SEM images after three and nine hours. The SEM image after one hour can be found in the main text.

Catalyst	Current density <sub>geo</sub> (mA cm <sup>-2</sup> )	Overpotential (V)	Electrolyte solution	Ref.
Ni <sub>5</sub> P <sub>4</sub> on nickel foil	-10	0.14	0.5 M H <sub>2</sub> SO <sub>4</sub>	This work
Ni <sub>5</sub> P <sub>4</sub> on nickel foil	-10	0.15	1 M KOH	This work
Ni <sub>5</sub> P <sub>4</sub> on nickel foam	-200	0.20	0.5 M H <sub>2</sub> SO <sub>4</sub>	This work
Ni <sub>2</sub> P NP (0.38 mg cm <sup>-2</sup> )	-20	0.25	1 M KOH	[148]
Ni <sub>2</sub> P NP (0.38 mg cm <sup>-2</sup> )	-20	0.14	0.5 M H <sub>2</sub> SO <sub>4</sub>	[148]
Ni <sub>2</sub> P NP	-20	0.13	0.5 M H <sub>2</sub> SO <sub>4</sub>	[129]
Ni <sub>2</sub> P NP	-20	0.18	1 M KOH	[129]
Mo <sub>2</sub> C/CNT	-10	0.15	0.1 M HClO <sub>4</sub>	[259]

Table S4: State-of-the-art HER catalysts and their performance in acid and in base (as mentioned in the main text).

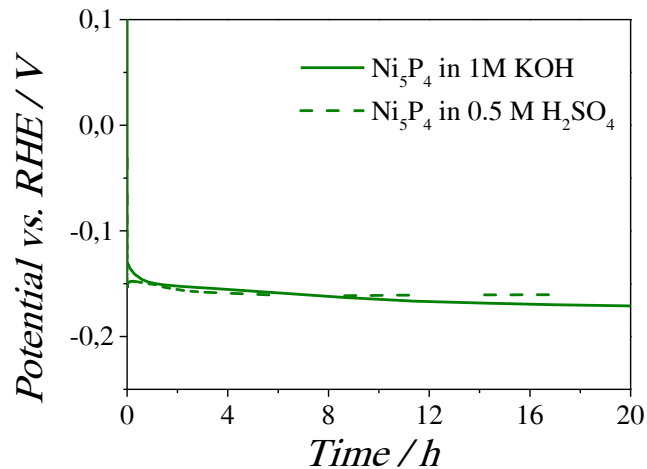


Figure S10: Long-term stability measurement of  $\text{Ni}_5\text{P}_4$  in 1 M KOH and 0.5 M  $\text{H}_2\text{SO}_4$  for a 20-hour period keeping the current density at  $-10 \text{ mA cm}^{-2}$  while monitoring the potential.

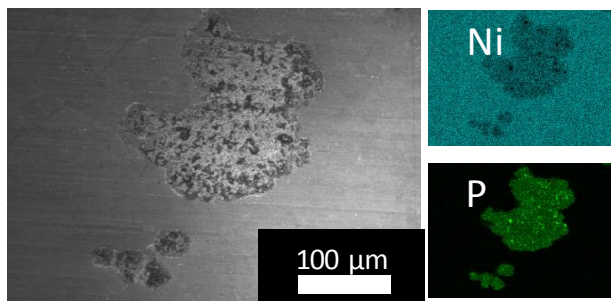


Figure S11: Formation of nickel phosphide islands after phosphidation of nickel foil.

The onset overpotential for the oxygen evolution reaction was determined with an optical oxygen probe. Hereby, chronoamperometry measurements were performed scanning from 1.40 V to 1.65 V vs. RHE in 5 mV steps while each potential was held for 60 s. A three electrode setup was used with an optical Fibox 3 oxygen probe close to the WE.

Catalyst	Current density (mA cm <sup>-2</sup> )	Overpotential (V)	Electrolyte solution	Ref.
NiOOH/Ni <sub>5</sub> P <sub>4</sub>	10	0.29	1 M KOH	This work
NiFeO <sub>x</sub> electrodepos.	10	0.35	1 M NaOH	[248]
IrO <sub>x</sub> electrodepos.	10	0.32	1 M NaOH	[248]
NiO <sub>x</sub> electrodepos.	10	0.42	1 M NaOH	[248]
NiCoO <sub>x</sub> electrodepos.	10	0.38	1 M NaOH	[248]
Co-P	10	0.34	1 M KOH	[49]

*Table S5: Selected state-of-the-art electrocatalysts for the oxygen evolution reaction.*

## **Chapter 6: Experimental and theoretical benchmarking of nickel based materials for the hydrogen evolution reaction**

### **Synthesis of Ni<sub>3</sub>S<sub>2</sub> on nickel foil**

The cleaned nickel foil was introduced into a three necked round bottom flask, evacuated three times, set under nitrogen and heated up to 550 °C. Three gram of TAA were provided into a round bottom flask connected with a trap filled with distilled water in order to collect emerging acetonitrile. The trap was in turn connected to the nickel foil including flask. By heating up the TAA containing flask to 400 °C, H<sub>2</sub>S and acetonitrile was generated. Acetonitrile was collected as liquid in the trap and H<sub>2</sub>S as gas could be introduced into the preheated sample containing flask. Both flasks were kept at the corresponding temperature for one hour. The final crystalline Ni<sub>3</sub>S<sub>2</sub> was obtained after annealing for one additional hour in nitrogen at 550 °C.

### **Synthesis of Ni<sub>3</sub>N on nickel foil**

The clean nickel foil (40\*20 mm) was introduced into a two-necked round bottom flask that was evacuated and set under NH<sub>3</sub> three times. The foil was kept at 450 °C for eight hours while a small flow of NH<sub>3</sub> was guaranteed. The flask was cooled down to RT and was left for a few hours in NH<sub>3</sub> for further exposure.

### **Preparation before electrochemistry**

The cleaned nickel foil was immersed in concentrated HNO<sub>3</sub> for two minutes and rinsed afterwards with distilled water before testing. The platinum foil was kept in 5 M H<sub>2</sub>SO<sub>4</sub> before use in order to remove impurities from the surface. Afterwards, the foils were first polished with diamond powder (1 μm, AS) followed by alumina powder (0.05 μm, AS) in an ethanol slurry. Ni<sub>5</sub>P<sub>4</sub>, Ni<sub>3</sub>N and Ni<sub>3</sub>S<sub>2</sub> were cleaned with ethanol and acetone prior to use. It is known that nickel can form a passivation layer of NiO

when in contact with air. For  $\text{Ni}_5\text{P}_4$ , it was also found that phosphate layers form on top. Therefore, before each measurement, the catalysts were precathodized in order to remove potential oxide layers.

#### **Electrochemically active surface area:**

Capacitance measurements have been performed by keeping the working electrode at open circuit voltage for 300 s and scanning afterwards at eight different scan rates (0.005, 0.01, 0.025, 0.05, 0.1, 0.2, 0.4, and  $0.8 \text{ V s}^{-1}$ ) around the open circuit potential (0.1 V window). The determined ECSA was used for normalization by dividing the current densities by the average measured ECSA value obtained from all materials ( $11.62 \text{ cm}^2$ ).

#### **7 Calculation of precursor price**

For cost calculation of nickel phosphides, sulfides, nitrides, pristine nickel, iridium, and platinum, all materials were disassembled into their constituting elements ( $\text{Ni}_5\text{P}_4$ : 5 Ni; 4 P). The next step comprised finding the most common mining form of these elements and the corresponding price was obtained from [260]. The price for phosphorous was obtained from phosphate rocks, sulfur from elemental sulfur and nitrogen from ammonia. The preparation costs were not included.

## 8.4 Characterization methods

### 8.4.1 X-ray powder diffraction

In general, diffraction occurs when light is scattered. In crystalline materials, the atoms are arranged periodically and repetitively in a crystal lattice. When electromagnetic radiation (e.g. X-rays) with wavelengths similar to the distance between atoms is used, diffraction patterns can be obtained, thus, giving information about the three

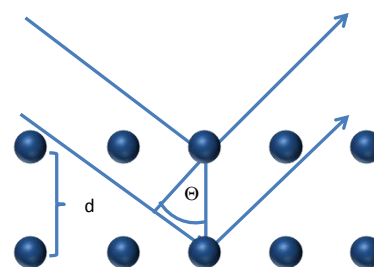


Figure S12: Derivation of Bragg's law.

dimensional arrays of atoms or molecules within the crystal. The condition for diffraction (Figure S12) was described by William Henry and William Laurence Bragg by the following equation:

$$2d \sin \vartheta = n \lambda \quad 8.1$$

where  $\lambda$  is the X-ray wavelength,  $\theta$  the angle of incident X-rays,  $d$  the interlayer spacing and  $n$  represents an integer. The rough particles size can be calculated by Scherrer's equation:

$$d = \frac{k \lambda}{\beta \cos(\vartheta)} \quad 8.2$$

where  $d$  displays the average particle sized,  $k$  the shape factor,  $\lambda$  the X-ray wavelength,  $\beta$  the full width at half maximum and  $\theta$  the diffraction angle. As shape factor, 0.9 was used assuming spherical crystallites and all data was fitted using a Lorentzian function. A Bruker D8 Advance instrument equipped with a scintillation detector was used for PRXD analysis with Cu K $\alpha$  ( $\lambda = 1.5418 \text{ \AA}$ ) radiation. As reference database, ICDD PDF 4+ was used – the corresponding reference patterns are indicated.

#### **8.4.2 Inductively coupled plasma-optical emission spectrometry and elemental analysis**

Elemental microanalysis works by sample combustion in O<sub>2</sub> atmosphere at temperatures over 1,000 °C where carbon, nitrogen, hydrogen and sulphur can be quantified. Hereby, SO<sub>2</sub>, CO<sub>2</sub>, H<sub>2</sub>O and N<sub>2</sub> (from NO<sub>x</sub>) are separated and detected via thermoconductivity measurements. ICP-OES measurements are based on emission of electromagnetic radiation characteristic for a certain element. Usually, the sample aerosol is injected into argon plasma where atomization occurs and atoms become excited and ionized. From the intensity of the electromagnetic radiation at a certain wavelength, the concentration can be determined when combined with calibration solutions.[261] Before each measurement, residual carbon was burned at 1,000 °C in air for 5 h and the metal oxide residue was dissolved in aqua regia. For ICP-OES measurements, the nickel content was determined at 231.60 nm and 221.64 nm and the phosphorous content was determined at 213.61 nm. For both elements, a four-point calibration was used.

#### **8.4.3 X-Ray photoelectron spectroscopy**

X-ray photoelectron spectroscopy (XPS) is a powerful surface technique where the sample is irradiated with X-ray in the range of 100-10,000 eV in high vacuum. Electrons from the core levels are freed and their kinetic energy measured. With increased atomic number, electrons are bound tighter resulting in increased binding energy ( $E_{bind}$ ). Based on the conservation of energy, the following equation can be deduced:

$$E_{kin} = E_{phot} - E_{bind} \quad 8.3$$

where  $E_{kin}$  displays the kinetic energy measured and  $E_{phot}$  the energy of incoming photons. Depending on the surrounding atoms, shifts in binding energy can be observed and are therefore used to distinguish between different chemical species.

#### 8.4.4 Scanning electron microscopy / scanning transmission electron microscopy

SEM and (S)TEM are both technics based on the interaction of electrons with the sample (Figure S13). In short, an electron gun produces electrons, accelerating through (electro)magnetic fields and lenses vertically through the microscope.

##### 8.4.4.1 Scanning electron microscopy

When hitting the specimen, different interaction of the sample with the electrode can be observed: secondary electrons are generated by collision of electrons from the beam and valence electrons from the specimen. The secondary electrons generated are close to the surface due to their comparable low energy (electrons at deeper regions can be easily absorbed by the specimen).

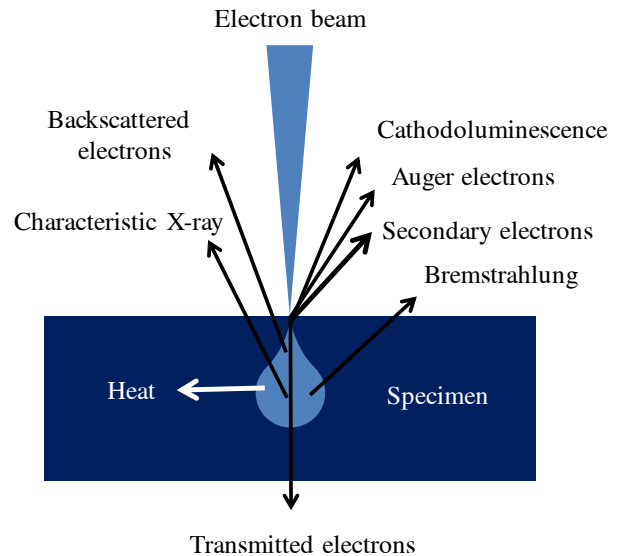


Figure S13: Interactions of the electron beam with the specimen.

Therefore, topographic information can be obtained due to local curvatures (e.g. edges, plates) that facilitate the release of a higher amount of electrons close to the surface. Another important type of electrons is donated as backscattering electrons – here, the incident electrons are scattered back on the nucleus escaping the surface from much higher depth and higher energy than secondary electrons. In contrast to secondary electrons where the electron yield will not change drastically with atomic number of the specimen, information about composition can be drawn from backscattering electrons. Hereby, the specimen with low atomic number will appear darker relative to regions with high atomic number where more electrons can be scattered. Furthermore, information about the present specimen can be obtained by

energy-dispersive X-ray (EDX). In combination with SEM, electrons from the inner shells can be excited. The resulting hole is occupied by an electron from the outer shell resulting in the emission of X-rays. An elemental signature can be obtained depending on the wavelength. As scanning electron microscope, a JEOL JSM-7500F instrument equipped with two EDX detectors (Oxford) and a LEO 1550-Gemini instrument were used with acceleration voltages ranging between 5 kV and 15 kV.

#### **8.4.4.2 (Scanning) transmission electron microscopy**

In TEM, electrons are also accelerated and interact with the sample but are led through a very thin film to attain higher resolutions. Hereby, the contrast correlates to the thickness of the sample and to the composition. Higher scattering from heavier elements appear darker than lighter elements that scatter less. The opposite effect can be observed in STEM mode where elements with higher atomic number appear lighter. Thereby, HAADF detectors allow the differentiation between heavy and light elements as observed in chapter 3. In general, the higher the applied acceleration voltages, the higher the resolution. Furthermore, diffraction of electrons leads to a selected area diffraction pattern (SAED) where information about the present species can be obtained. Hereby, information obtained from the microscopy image can be correlated to the preset crystal, therefore, making it highly useful for small samples amounts.

#### **8.4.5 Electron-energy-loss spectroscopy**

While EDX is useful in identifying the atomic composition of the specimen, electron-energy-loss spectroscopy (EELS) demonstrates sensitivity to the binding state of the probed specimen. Hereby, electrons are accelerated onto the sample where energy loss occurs when they are inelastically scattered. By means of an electron spectrometer, the energy loss can be determined and conclusion on the atomic composition and the binding state can be drawn.

#### 8.4.6 Raman/Infrared spectroscopy

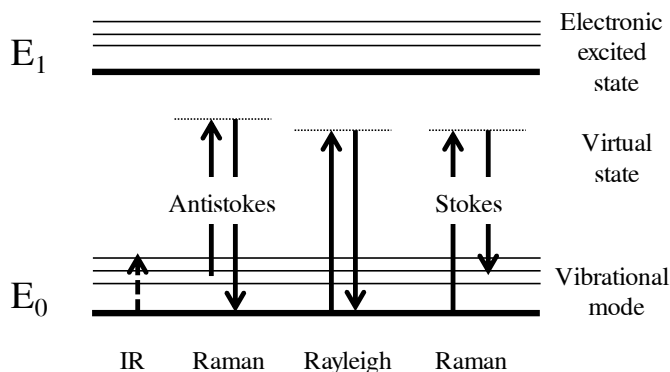


Figure S14: Energy levels reached by Raman and IR spectroscopy.

Raman and infrared spectroscopy are both methods based on detecting vibrational modes of molecules either by direct absorption of photons (infrared spectroscopy) or by inelastic scattering of photons (Raman) and is

displayed in Figure S14. The latter works by irradiation of monochromatic light on the sample where scattering occurs. The electromagnetic radiation and its oscillating electric field induce an electric dipole in the molecule and change the polarizability because of orbital distortion. The Raman-active vibrational modes can be detected when the polarizability of the molecule changes along the normal coordinate. Thereby, elastic scattering contributes the main part of the scattering light and is referred to as Rayleigh scattering. The other scattering process is inelastic scattering where the scattered light can be either shifted to lower energies (stokes) or to higher energies (anti-stokes). An attenuated total reflection Thermo Scientific™ Nicolet™ iS™5 FT-IR spectrometer was used for FT-IR measurements. Raman spectra were recorded using an alpha300 R confocal Raman microscope from WiTec equipped with a frequency doubled 532 nm ND/YAG laser.

#### 8.4.7 Optical oxygen probe measurements

The oxygen probe measurements are based on fluorescent quenching of a fluorophore (e.g. a ruthenium dye) by oxygen. The tip of the oxygen probe – where the fluorophore is embedded – can be in direct contact with the investigated solution. The fluorophore can be excited by a light source through an optical cable. If no oxygen

is present, fluorescence emission from the dye can be detected by a spectrometer. If oxygen is present, the energy is transferred non-radiantly from the fluorophore to oxygen. Thereby, fluorescence quenching takes place depending on the concentration of present oxygen as described ideally by the *Stern-Volmer equation* :[262, 263]

$$\frac{I_0}{I} = 1 + K_{SV} * p[O_2] \quad 8.4$$

with  $I_0$  and  $I$  as luminescence intensities without and with oxygen,  $K_{SV}$  as Stern-Volmer constant and  $p[O_2]$  as partial pressure of oxygen present. The calibration of the oxygen probe was done by a two-point calibration. The 100% air saturation sample was prepared by bubbling air through distilled water for 30 minutes whereas the 0% air saturation was achieved by using a solution of 1 mg sodium sulfite (will be converted to sulfate) and 10 mg cobalt chloride (as catalyst) in a 100 ml flask.

#### **8.4.8 Thermogravimetric analysis**

Thermodynamic events such as thermal stability, phase transitions, adsorption and desorption of gases can be monitored by TGA measurements. Typically, the mass loss of a compound is monitored with changing time and temperature. A Perkin-Elmer STA 6000 was used for TGA measurements.

#### **8.4.9 Electrochemistry**

##### **General information**

If not otherwise stated, electrochemical measurements were either performed at a Bio-logic MPG-2 test station or a Gamry 600 potentiostat. As working electrode, the electrodes were cut and mounted on an adapted RDE electrode (Gamry lithium battery standard cell kit) exposing a well-defined surface area of  $0.43 \text{ cm}^2$  as displayed in Figure 36. For linear sweep voltammetry and chronoamperometry measurements, the working electrode was rotated at 2,000 rpm in order to move the solution in a well-controlled and defined manner. Thereby, the analyte can diffuse to the electrode

faster due to the thinner stagnant layer and higher current can be measured (decrease in diffusion overpotential). Forced convection is especially desired for steady state experiments where the RDE demonstrates a reliable technique with reproducible results. Thereby, ions or molecules can move from the bulk solution to the electrode surface. The following equation displays the dependence of rotation speed and the diffusion layer thickness:

$$\delta = 1.61 D^{1/3} \nu^{1/6} \omega^{-1/2} \quad 8.5$$

where  $\delta$  displays the thickness of the diffusion layer,  $D$  the diffusion coefficient,  $\omega$  the rotation speed and  $\nu$  the kinematic viscosity. On the one hand, a strong improvement of activity was observed when rotating the working electrode at 2,000 rpm. On the other, catalyst blocking by evolving gas bubbles could be observed for the non-rotating electrodes.

## Methods

In linear sweep voltammetry, the potential is scanned from a lower limit to an upper limit in a fixed potential range and the voltage scan rate can be adjusted. By applying an additional reverse scan, cyclic voltammograms are obtained. In all cases, the corresponding current response is recorded. As the scan rate is changed, an altered current response can be observed. In chronoamperometric measurements a certain potential is applied for a specific time. In doing so, long-term stability measurements and changes on the surface can be monitored. In chronopotentiometry measurements, a certain current is set and the potential consequently monitored.

Due to the fact that the electrode processes are not only governed by the quality of the catalysts, other factors have to be compensated for. Therefore, the electrolyte resistance between the two electrodes were kept relatively small using 1 M KOH and 0.5 M H<sub>2</sub>SO<sub>4</sub> with high conductivity that belong to the electrolytes with the highest

worldwide production volumes. In electrochemical impedance measurements, a certain AC potential is applied and the current response is recorded. Information about double layer capacitance, solution resistances or charge transfer resistances can be obtained. In Figure S15, a Randles equivalent circuit is schematically drawn representing an electrochemical half-cell.

From the model, the resistance of a certain system denoted as  $R_s$  (including solution-, wire- or substrate-resistance) can be obtained.  $R_s$  is obtained at high frequencies where the curve intersects with  $Z_{im}$ . Thereby, the  $C_{DL}$  approach 0 and  $R_s$  used for  $iR_s$  compensation can be obtained. Typical values ranged between 3-4  $\Omega$  (1 M KOH, 0.5 M  $H_2SO_4$ ) and 40-50  $\Omega$  (0.1 M KOH, 0.05 M  $H_2SO_4$ ) for the used setup. The potential drop can be determined accordingly:

$$\Delta E = i * R_s = E_{applied} - E_{real} \quad 8.6$$

Where  $E_{applied}$  is the applied potential by the potentiostat,  $E_{real}$  is the real potential at the working electrode,  $i$  is the measured current at  $E_{applied}$  and  $R_s$  is the resistance of the system. The setup used for measurements was optimized using an in-house designed electrochemical cell where the reference electrode can be placed in close proximity to the working electrode. Moreover, it is possible to obtain information about charge transfer resistance ( $R_{CT}$ ) and double layer capacitance ( $C_{DL}$ ). EIS measurements were performed by applying on the open circuit potential an AC voltage of 10 mV rms between 0.1 Hz and 20 kHz recording every 10 points per decade whereby the higher frequency impedance was used to account for solution resistance. A saturated calomel electrode in base (1 M KOH) and an Ag/AgCl (sat) electrode in acid (1 M  $H_2SO_4$ ) was used as reference electrode. Both electrodes were regularly tested against a master SCE electrode. A coiled platinum wire (Sigma Aldrich) was used as counter electrode. All potentials are indicated vs. RHE and the following conversion from SCE to RHE in 1 M KOH was used.

$$E(RHE) = E(SCE) + 0.059 * 14 + 0.244 \quad 8.7$$

All potentials were indicated vs. RHE and the following conversion from Ag/AgCl to RHE in 0.5 M H<sub>2</sub>SO<sub>4</sub> was used.

$$E(RHE) = E(Ag/AgCl) + 0.197 \quad 8.8$$

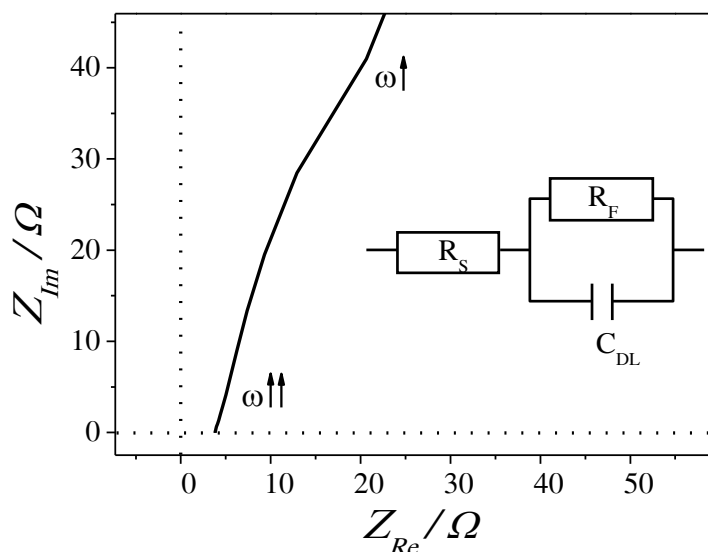


Figure S15: Typical impedance spectrum in the high frequency end of Ni<sub>5</sub>P<sub>4</sub> with high charge transfer resistance  $R_{CT}$  displayed in the schematically drawn Randles circuit.

#### 8.4.10 Nitrogen sorption

Adsorption measurements are based on the enrichment of gas molecules (adsorptive) at a solid surface (adsorbent). Nitrogen sorption works at constant temperatures of 77 K and the gas is dosed in small portions into the sample tube. Some molecules are adsorbed by the sample reducing its amount in the gas phase. The equilibrium pressure is monitored and the quantity of gas can be determined. Therefore, a dependence of amount adsorbed and relative pressure can be observed. Possible resulting isotherms are displayed in Figure S16. Depending on the isotherm different pore types can be distinguished: macropores with pore widths over 50 nm, mesopores with pore widths between 2 nm and 50 nm and micropores with pores diameter below 2 nm. When adsorption and desorption curves do not coincide, an

adsorption hysteresis can be observed. Before nitrogen sorption experiments at 77 K, all samples were first degassed at 150 °C for 20 h. The measurement itself was performed using a Quantachrome Quadrasorb Si porosimeter and applying the Brunauer-Emmet-Teller (BET) model to the isotherms apparent surface area determination. The relative pressure range of  $p/p^0 < 0.3$  of the adsorption branch was used for surface area analysis.

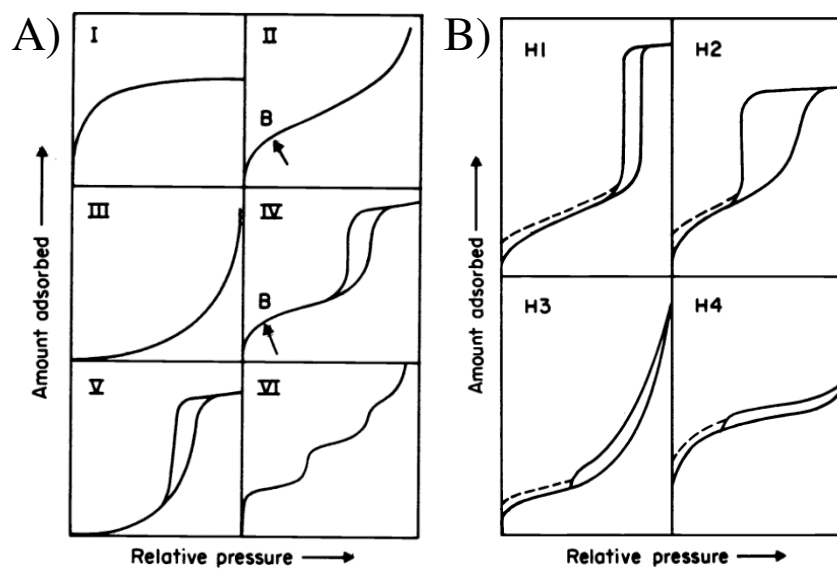


Figure S16: Isotherms (A) and hysteresis (B) types according to IUPAC. Taken from [84].

## 9 References

---

- [1] United Nations, Population Division, World Population Prospects: The 2015 Revision. [http://esa.un.org/unpd/wpp/Publications/Files/Key\\_Findings\\_WPP\\_2015.pdf](http://esa.un.org/unpd/wpp/Publications/Files/Key_Findings_WPP_2015.pdf) (accessed 15.12.2015).
  - [2] British Petroleum Company, BP Statistical Review of World Energy June 2015. [http://www.bp.com/content/dam/bp-country/de\\_de/PDFs/brochures/bp-statistical-review-of-world-energy-2015-full-report.pdf](http://www.bp.com/content/dam/bp-country/de_de/PDFs/brochures/bp-statistical-review-of-world-energy-2015-full-report.pdf) (accessed 14.12.2015).
  - [3] The World Bank, Health Nutrition and Population Statistics: Population estimates and projections. <http://data.worldbank.org/data-catalog/health-nutrition-and-population-statistics> (accessed 15.12.2015).
  - [4] World Energy Council, World Energy Scenarios: Composing Energy Futures to 2050. [https://www.worldenergy.org/wp-content/uploads/2013/09/World-Energy-Scenarios\\_Composing-energy-futures-to-2050\\_Full-report.pdf](https://www.worldenergy.org/wp-content/uploads/2013/09/World-Energy-Scenarios_Composing-energy-futures-to-2050_Full-report.pdf) (accessed 15.12.2015).
  - [5] World Bank, World Development Indicators. <http://data.worldbank.org/indicator> (accessed 03.01.2016).
  - [6] Mattias Lindgren, Income per person. <http://www.gapminder.org/data/> (accessed 03.01.2016).
  - [7] Carbon Dioxide Information Analysis Center, Per capita CO<sub>2</sub> emissions (metric tons of CO<sub>2</sub>). <http://cdiac.ornl.gov/> (accessed 03.01.2016).
  - [8] M. Ball, M. Wietschel, *The Hydrogen Economy: Opportunities and Challenges*, Cambridge University Press, **2009**.
  - [9] D. A. J. Rand, R. Dell, *Hydrogen Energy: Challenges and Prospects*, The Royal Society of Chemistry, **2008**.
  - [10] Earth System Research Laboratory, Trends in Atmospheric Carbon Dioxide. (accessed 25.10.2015).
  - [11] D. Das, T. N. Veziroğlu, *International Journal of Hydrogen Energy* **2001**, *26*, 13.
  - [12] M. Balat, *International Journal of Hydrogen Energy* **2008**, *33*, 4013.
  - [13] U. Eberle, B. Muller, R. von Helmolt, *Energy & Environmental Science* **2012**, *5*, 8780.
  - [14] National Renewable Energy Laboratory, Current (2009) State of the Art Hydrogen Production Cost Estimate Using Water Electrolysis. (accessed 11.12.2015).
  - [15] G. Ertl, H. Knözinger, F. Schüth, J. Weitkamp, *Handbook of Heterogeneous Catalysis*, Wiley-VCH, Weinheim, **2008**.
  - [16] U.S. Department of Energy, Where the energy goes: gasoline vehicles. <http://www.fueleconomy.gov/feg/atv.shtml> (accessed 27.12.2015).
  - [17] G. Sandstede, E. J. Cairns, V. S. Bagotsky, K. Wiesener, *Handbook of Fuel Cells*, **2010**.
  - [18] P. Kaiser, R. B. Unde, C. Kern, A. Jess, *Chemie Ingenieur Technik* **2013**, *85*, 489.
  - [19] O. Strohbach, Weltpremiere: Audi eröffnet Power-to-Gas-Anlage. <https://www.audi-mediacycenter.com/de/pressemitteilungen/weltpremiere-audi-eroeffnet-power-to-gas-anlage-784/download> (accessed 01.11.2015).
  - [20] M. W. Melaina, O. Antonia, M. Penev, Blending hydrogen into natural gas pipeline networks: a review of key issues. <http://www.nrel.gov/docs/fy13osti/51995.pdf> (accessed 29.10.2015).
  - [21] D. Esposito, M. Antonietti, *Chemical Society Reviews* **2015**, *44*, 5821.
  - [22] J. A. Bakken, R. Jensen, B. Monsen, O. Raaness, A. N. Wærnes, *Pure and Applied Chemistry* **1998**, *70*, 1223.
  - [23] S. Trasatti, *Advances in electrochemical science and engineering*, **2008**.
  - [24] K. C. Neyerlin, W. Gu, J. Jorne, H. A. Gasteiger, *Journal of The Electrochemical Society* **2007**, *154*, B631.
  - [25] N. M. Marković, B. N. Grgur, P. N. Ross, *The Journal of Physical Chemistry B* **1997**, *101*, 5405.
-

- [26] A. Lasia, Handbook of Fuel Cells, **2010**.
- [27] J. O. M. Bockris, B. E. Conway, E. B. Yeager, *Comprehensive Treatise of Electrochemistry*, Plenum Press, **1980**.
- [28] M. Gong, D.-Y. Wang, C.-C. Chen, B.-J. Hwang, H. Dai, *Nano Research* **2015**, 1.
- [29] O. A. Petrii, G. A. Tsirlina, *Electrochimica Acta* **1994**, 39, 1739.
- [30] S. Trasatti, Handbook of Fuel Cells, **2010**.
- [31] S. Trasatti, *Journal of Electroanalytical Chemistry and Interfacial Electrochemistry* **1972**, 39, 163.
- [32] G. Jerkiewicz, *Progress in Surface Science* **1998**, 57, 137.
- [33] P. Quaino, F. Juarez, E. Santos, W. Schmickler, *Beilstein Journal of Nanotechnology* **2014**, 5, 846.
- [34] R. Parsons, *Transactions of the Faraday Society* **1958**, 54, 1053.
- [35] T. F. Jaramillo, K. P. Jørgensen, J. Bonde, J. H. Nielsen, S. Horch, I. Chorkendorff, *Science* **2007**, 317, 100.
- [36] J. Kibsgaard, C. Tsai, K. Chan, J. D. Benck, J. K. Nørskov, F. Abild-Pedersen, T. F. Jaramillo, *Energy & Environmental Science* **2015**, 8, 3022.
- [37] J. Kibsgaard, Z. Chen, B. N. Reinecke, T. F. Jaramillo, *Nature Materials* **2012**, 11, 963.
- [38] M. M. Jaksic, *International Journal of Hydrogen Energy* **1986**, 11, 519.
- [39] M. H. Miles, *Journal of Electroanalytical Chemistry and Interfacial Electrochemistry* **1975**, 60, 89.
- [40] C. J. H. Jacobsen, S. Dahl, B. S. Clausen, S. Bahn, A. Logadottir, J. K. Nørskov, *Journal of the American Chemical Society* **2001**, 123, 8404.
- [41] V. Molinari, C. Giordano, M. Antonietti, D. Esposito, *Journal of the American Chemical Society* **2014**, 136, 1758.
- [42] P. Strasser, Q. Fan, M. Devenney, W. H. Weinberg, P. Liu, J. K. Nørskov, *The Journal of Physical Chemistry B* **2003**, 107, 11013.
- [43] J. Greeley, T. F. Jaramillo, J. Bonde, I. Chorkendorff, J. K. Nørskov, *Nature Materials* **2006**, 5, 909.
- [44] Y. Liu, S. Liu, D. He, N. Li, Y. Ji, Z. Zheng, F. Luo, S. Liu, Z. Shi, C. Hu, *Journal of the American Chemical Society* **2015**, 137, 12697.
- [45] A.-M. Alexander, J. S. J. Hargreaves, *Chemical Society Reviews* **2010**, 39, 4388.
- [46] L. Ma, L. R. L. Ting, V. Molinari, C. Giordano, B. S. Yeo, *Journal of Materials Chemistry A* **2015**, 3, 8361.
- [47] H. B. Wu, B. Y. Xia, L. Yu, X.-Y. Yu, X. W. Lou, *Nature Communications* **2015**, 6.
- [48] P. C. K. Vesborg, B. Seger, I. Chorkendorff, *The Journal of Physical Chemistry Letters* **2015**, 6, 951.
- [49] N. Jiang, B. You, M. Sheng, Y. Sun, *Angewandte Chemie International Edition* **2015**, 54, 6251.
- [50] H. Vrubel, T. Moehl, M. Gratzel, X. Hu, *Chemical Communications* **2013**, 49, 8985.
- [51] A. K. M. S. Huq, A. J. Rosenberg, *Journal of The Electrochemical Society* **1964**, 111, 270.
- [52] M. Hambourger, M. Gervaldo, D. Svedruzic, P. W. King, D. Gust, M. Ghirardi, A. L. Moore, T. A. Moore, *Journal of the American Chemical Society* **2008**, 130, 2015.
- [53] A. Sobczynski, A. Yildiz, A. J. Bard, A. Campion, M. A. Fox, T. Mallouk, S. E. Webber, J. M. White, *The Journal of Physical Chemistry* **1988**, 92, 2311.
- [54] I. Arul Raj, V. K. Venkatesan, *International Journal of Hydrogen Energy* **1988**, 13, 215.
- [55] H. Tributsch, J. C. Bennett, *Journal of Electroanalytical Chemistry and Interfacial Electrochemistry* **1977**, 81, 97.
- [56] M. Antonietti, N. Fechner, T.-P. Fellingner, *Chemistry of Materials* **2014**, 26, 196.
- [57] W. Schwieger, A. G. Machoke, T. Weissenberger, A. Inayat, T. Selvam, M. Klumpp, A. Inayat, *Chemical Society Reviews* **2016**.
- [58] R. Srivastava, P. Mani, N. Hahn, P. Strasser, *Angewandte Chemie International Edition* **2007**, 46, 8988.

- [59] C. Cui, L. Gan, M. Heggen, S. Rudi, P. Strasser, *Nature Materials* **2013**, *12*, 765.
- [60] R. B. Levy, M. Boudart, *Science* **1973**, *181*, 547.
- [61] S. Carenco, D. Portehault, C. Boissière, N. Mézailles, C. Sanchez, *Chemical Reviews* **2013**, *113*, 7981.
- [62] D. M. Muir, E. Ho, *Transactions of the Institutions of Mining and Metallurgy, Section C: Mineral Processing and Extractive Metallurgy* **2006**, *115*, 57.
- [63] G. Wedler, *Lehrbuch der Physikalischen Chemie*, Wiley, **2005**.
- [64] E. Lassner, W. D. Schubert, *Tungsten: Properties, Chemistry, Technology of the Element, Alloys, and Chemical Compounds*, Springer US, **2012**.
- [65] I. Nikolov, K. Petrov, T. Vitanov, A. Gushev, *International Journal of Hydrogen Energy* **1983**, *8*, 437.
- [66] J. D. Benck, Z. Chen, L. Y. Kuritzky, A. J. Forman, T. F. Jaramillo, *ACS Catalysis* **2012**, *2*, 1916.
- [67] M. B. I. Janjua, R. L. Le Roy, *International Journal of Hydrogen Energy* **1985**, *10*, 11.
- [68] I. Chorkendorff, J. W. Niemantsverdriet, *Concepts of Modern Catalysis and Kinetics*, Wiley, **2003**.
- [69] D. Friedman, T. Masciangioli, S. Olson, C. S. Roundtable, B. C. S. Technology, D. E. L. Studies, N. R. Council, *The Role of the Chemical Sciences in Finding Alternatives to Critical Resources: A Workshop Summary*, National Academies Press, **2012**.
- [70] R. L. LeRoy, *International Journal of Hydrogen Energy* **1983**, *8*, 401.
- [71] J. R. Holst, A. I. Cooper, *Advanced Materials* **2010**, *22*, 5212.
- [72] V. Georgakilas, D. Gournis, V. Tzitzios, L. Pasquato, D. M. Guldi, M. Prato, *Journal of Materials Chemistry* **2007**, *17*, 2679.
- [73] K. K. Chung, N. Fechler, M. Antonietti, *Advanced Porous Materials* **2014**, *2*, 61.
- [74] N. Fechler, T.-P. Feller, M. Antonietti, *Advanced Materials* **2013**, *25*, 75.
- [75] F. Schipper, A. Vizintin, J. Ren, R. Dominko, T.-P. Feller, *ChemSusChem* **2015**, *8*, 3077.
- [76] American Chemical Society National Historic Chemical Landmarks, Production of Aluminum: The Hall-Héroult Process.  
<http://www.acs.org/content/acs/en/education/whatischemistry/landmarks/aluminumprocess.html> (accessed 2016.01.02).
- [77] D. Portehault, S. Devi, P. Beaunier, C. Gervais, C. Giordano, C. Sanchez, M. Antonietti, *Angewandte Chemie International Edition* **2011**, *50*, 3262.
- [78] X. Liu, M. Antonietti, C. Giordano, *Chemistry of Materials* **2013**, *25*, 2021.
- [79] W. Lei, D. Portehault, R. Dimova, M. Antonietti, *Journal of the American Chemical Society* **2011**, *133*, 7121.
- [80] M. Shalom, V. Molinari, D. Esposito, G. Clavel, D. Ressnig, C. Giordano, M. Antonietti, *Advanced Materials* **2014**, *26*, 1272.
- [81] G. J. Janz, *Molten Salts Handbook*, **1967**, pp. 102.
- [82] M. A. Bredig, U. S. A. E. Commission, L. Oak Ridge National, *Mixtures of metals with molten salts*, Oak Ridge National Laboratory, Oak Ridge, Tenn., **1963**.
- [83] Centre for Research in Computational Thermochemistry, NiCl<sub>2</sub>-LiCl.  
[http://www.crct.polymtl.ca/fact/phase\\_diagram.php?file=LiCl-NiCl2.jpg&dir=FTsalt](http://www.crct.polymtl.ca/fact/phase_diagram.php?file=LiCl-NiCl2.jpg&dir=FTsalt) (accessed 11.12.2015).
- [84] K. S. W. Sing, D. H. Everett, R. A. W. Haul, L. Moscou, R. A. Pierotti, J. Rouquerol, T. Siemieniewska, *Handbook of Heterogeneous Catalysis*, **2008**.
- [85] Jonas Pampel, Tim-Patrick Feller, *Advanced Energy Materials*, **2016**.
- [86] M. J. Bojdys, J.-O. Müller, M. Antonietti, A. Thomas, *Chemistry – A European Journal* **2008**, *14*, 8177.
- [87] A. V. Ryazhkin, T. Miyahara, T. Ogasawara, A. M. Patselov, E. G. Chernyshev, Y. A. Babanov, V. P. Pilyugin, *The Physics of Metals and Metallography* **2009**, *107*, 179.
- [88] G. J. Janz, *Molten salts handbook*, Academic Press, New York, **1967**.
- [89] R. J. Toh, A. Y. S. Eng, Z. Sofer, D. Sedmidubsky, M. Pumera, *ChemElectroChem* **2015**, *2*, 982.

- [90] A. Bélanger, A. K. Vijh, *Journal of The Electrochemical Society* **1974**, *121*, 225.
- [91] R. Subbaraman, D. Tripkovic, K.-C. Chang, D. Strmcnik, A. P. Paulikas, P. Hirunsit, M. Chan, J. Greeley, V. Stamenkovic, N. M. Markovic, *Nature Materials* **2012**, *11*, 550.
- [92] J. A. Rodriguez, D. W. Goodman, *Science* **1992**, *257*, 897.
- [93] E. Kampshoff, E. Hahn, K. Kern, *Physical Review Letters* **1994**, *73*, 704.
- [94] I. J. Godwin, M. E. G. Lyons, *Electrochemistry Communications* **2013**, *32*, 39.
- [95] G. K. Schweitzer, L. L. Pesterfield, *The Aqueous Chemistry of the Elements*, Oxford University Press, **2009**.
- [96] I. C. Man, H.-Y. Su, F. Calle-Vallejo, H. A. Hansen, J. I. Martínez, N. G. Inoglu, J. Kitchin, T. F. Jaramillo, J. K. Nørskov, J. Rossmeisl, *ChemCatChem* **2011**, *3*, 1159.
- [97] Y. Zhao, R. Nakamura, K. Kamiya, S. Nakanishi, K. Hashimoto, *Nature Communications* **2013**, *4*.
- [98] R. Subbaraman, D. Tripkovic, D. Strmcnik, K.-C. Chang, M. Uchimura, A. P. Paulikas, V. Stamenkovic, N. M. Markovic, *Science* **2011**, *334*, 1256.
- [99] P. A. Thiel, T. E. Madey, *Surface Science Reports* **1987**, *7*, 211.
- [100] A. G. Gavriliuk, I. A. Trojan, V. V. Struzhkin, *Physical Review Letters* **2012**, *109*, 086402.
- [101] Y. Li, H. Wang, L. Xie, Y. Liang, G. Hong, H. Dai, *Journal of the American Chemical Society* **2011**, *133*, 7296.
- [102] J. Liang, Y. Yang, J. Zhang, J. Wu, P. Dong, J. Yuan, G. Zhang, J. Lou, *Nanoscale* **2015**, *7*, 14813.
- [103] A. V. Syugaev, N. V. Lyalina, S. F. Lomaeva, S. M. Reshetnikov, *Protection of Metals and Physical Chemistry of Surfaces* **2012**, *48*, 515.
- [104] X. Fan, Z. Peng, R. Ye, H. Zhou, X. Guo, *ACS Nano* **2015**, *9*, 7407.
- [105] Y. Goto, K. Taniguchi, T. Omata, S. Otsuka-Yao-Matsuo, N. Ohashi, S. Ueda, H. Yoshikawa, Y. Yamashita, H. Oohashi, K. Kobayashi, *Chemistry of Materials* **2008**, *20*, 4156.
- [106] Y. Leng, H. Shao, Y. Wang, M. Suzuki, X. Li, *Journal of Nanoscience and Nanotechnology* **2006**, *6*, 221.
- [107] Z. L. Schaefer, K. M. Weeber, R. Misra, P. Schiffer, R. E. Schaak, *Chemistry of Materials* **2011**, *23*, 2475.
- [108] Y. Leng, Y. Liu, X. Song, X. Li, *Journal of Nanoscience and Nanotechnology* **2008**, *8*, 4477.
- [109] W. Zhou, K. Zheng, L. He, R. Wang, L. Guo, C. Chen, X. Han, Z. Zhang, *Nano Letters* **2008**, *8*, 1147.
- [110] D. L. Leslie-Pelecky, X. Q. Zhang, S. H. Kim, M. Bonder, R. D. Rieke, *Chemistry of Materials* **1998**, *10*, 164.
- [111] S. I. Nikitenko, Y. Koltypin, O. Palchik, I. Felner, X. N. Xu, A. Gedanken, *Angewandte Chemie International Edition* **2001**, *40*, 4447.
- [112] C. N. Chinnasamy, B. Jeyadevan, K. Shinoda, K. Tohji, A. Narayanasamy, K. Sato, S. Hisano, *Journal of Applied Physics* **2005**, *97*, 10J309.
- [113] Y. T. Jeon, J. Y. Moon, G. H. Lee, J. Park, Y. Chang, *The Journal of Physical Chemistry B* **2006**, *110*, 1187.
- [114] V. Tzitzios, G. Basina, M. Gjoka, V. Alexandrakis, V. Georgakilas, D. Niarchos, N. Boukos, D. Petridis, *Nanotechnology* **2006**, *17*, 3750.
- [115] M. Han, Q. Liu, J. He, Y. Song, Z. Xu, J. M. Zhu, *Advanced Materials* **2007**, *19*, 1096.
- [116] S. Mourdikoudis, L. M. Liz-Marzán, *Chemistry of Materials* **2013**, *25*, 1465.
- [117] J. V. Hoene, R. G. Charles, W. M. Hickam, *The Journal of Physical Chemistry* **1958**, *62*, 1098.
- [118] J. D. S. Newman, G. J. Blanchard, *Langmuir* **2006**, *22*, 5882.
- [119] S. Carenco, C. Boissière, L. Nicole, C. Sanchez, P. Le Floch, N. Mézailles, *Chemistry of Materials* **2010**, *22*, 1340.
- [120] H. Cölfen, M. Antonietti, *Mesocrystals and Nonclassical Crystallization*, **2008**, pp. 7.
- [121] W. B. Pearson, *A Handbook of Lattice Spacings and Structures of Metals and Alloys*, Vol. 4, **1958**, pp. 254.
- [122] S. A. Sadeek, *Anales de la Asociación Química Argentina* **2005**, *93*, 165.

- [123] K. Nakamoto, P. J. McCarthy, A. Ruby, A. E. Martell, *Journal of the American Chemical Society* **1961**, *83*, 1066.
- [124] M. Hesse, H. Meier, B. Zeeh, *Spektroskopische Methoden in der organischen Chemie*, Thieme, **2005**.
- [125] S. G. Kwon, T. Hyeon, *Accounts of Chemical Research* **2008**, *41*, 1696.
- [126] C. B. Murray, D. J. Norris, M. G. Bawendi, *Journal of the American Chemical Society* **1993**, *115*, 8706.
- [127] L. H. Gade, *Koordinationschemie*, **1998**, pp. 87.
- [128] R.-K. Chiang, R.-T. Chiang, *Inorganic Chemistry* **2007**, *46*, 369.
- [129] E. J. Popczun, J. R. McKone, C. G. Read, A. J. Biacchi, A. M. Wiltrout, N. S. Lewis, R. E. Schaak, *J Am Chem Soc* **2013**, *135*, 9267.
- [130] A. E. Henkes, Y. Vasquez, R. E. Schaak, *Journal of the American Chemical Society* **2007**, *129*, 1896.
- [131] K.-Y. Niu, J. Park, H. Zheng, A. P. Alivisatos, *Nano Letters* **2013**, *13*, 5715.
- [132] A. V. Syugaev, N. V. Lyalina, S. F. Lomayeva, A. N. Maratkanova, *Journal of Solid State Electrochemistry* **2015**, *1*.
- [133] T. Borucinsky, S. Rausch, H. Wendt, *Journal of Applied Electrochemistry* **1997**, *27*, 762.
- [134] G. P. Power, *Electrochimica Acta* **1982**, *27*, 359.
- [135] E. Ghali, C. Meric, D. Deroo, *Journal of Applied Electrochemistry* **1981**, *11*, 153.
- [136] S. Fletcher, *Journal of Solid State Electrochemistry* **2009**, *13*, 537.
- [137] X. Wang, Y. V. Kolen'ko, L. Liu, *Chemical Communications* **2015**, *51*, 6738.
- [138] H. Vrubel, X. Hu, *Angewandte Chemie International Edition* **2012**, *51*, 12703.
- [139] J. Albero, P. Riente, J. N. Clifford, M. A. Pericàs, E. Palomares, *The Journal of Physical Chemistry C* **2013**, *117*, 13374.
- [140] A. V. Tivanski, Y. He, E. Borguet, H. Liu, G. C. Walker, D. H. Waldeck, *The Journal of Physical Chemistry B* **2005**, *109*, 5398.
- [141] M. Shalom, S. Inal, C. Fettkenhauer, D. Neher, M. Antonietti, *Journal of the American Chemical Society* **2013**, *135*, 7118.
- [142] F. Nozaki, M. Tokumi, *Journal of Catalysis* **1983**, *79*, 207.
- [143] F. Nozaki, T. Kitoh, T. Sodesawa, *Journal of Catalysis* **1980**, *62*, 286.
- [144] J. F. Callejas, J. M. McEnaney, C. G. Read, J. C. Crompton, A. J. Biacchi, E. J. Popczun, T. R. Gordon, N. S. Lewis, R. E. Schaak, *ACS Nano* **2014**.
- [145] P. Jiang, Q. Liu, Y. Liang, J. Tian, A. M. Asiri, X. Sun, *Angewandte Chemie International Edition* **2014**, *53*, 12855.
- [146] A. Lu, Y. Chen, H. Li, A. Dowd, M. B. Cortie, Q. Xie, H. Guo, Q. Qi, D.-L. Peng, *International Journal of Hydrogen Energy* **2014**, *39*, 18919.
- [147] E. J. Popczun, C. G. Read, C. W. Roske, N. S. Lewis, R. E. Schaak, *Angewandte Chemie International Edition* **2014**, *53*, 5427.
- [148] L. Feng, H. Vrubel, M. Bensimon, X. Hu, *Physical Chemistry Chemical Physics* **2014**, *16*, 5917.
- [149] Z. Huang, Z. Chen, Z. Chen, C. Lv, H. Meng, C. Zhang, *ACS Nano* **2014**, *8*, 8121.
- [150] P. Xiao, M. A. Sk, L. Thia, X. Ge, R. J. Lim, J.-Y. Wang, K. H. Lim, X. Wang, *Energy & Environmental Science* **2014**, *7*, 2624.
- [151] S. T. Oyama, *Handbook of Heterogeneous Catalysis*, **2008**.
- [152] J. Spivey, Y. F. Han, K. Dooley, *SPR Catalysis V26*, Royal Society of Chemistry, **2014**.
- [153] A. R. J. Kucernak, V. N. Naranammalpuram Sundaram, *Journal of Materials Chemistry A* **2014**, *2*, 17435.
- [154] A. B. Laursen, K. R. Patraju, M. J. Whitaker, M. Retuerto, T. Sarkar, N. Yao, K. V. Ramanujachary, M. Greenblatt, G. C. Dismukes, *Energy & Environmental Science* **2015**, *8*, 1027.
- [155] Y. Luo, J. Jiang, W. Zhou, H. Yang, J. Luo, X. Qi, H. Zhang, D. Y. W. Yu, C. M. Li, T. Yu, *Journal of Materials Chemistry* **2012**, *22*, 8634.

- [156] J. D. Roy-Mayhew, G. Boschloo, A. Hagfeldt, I. A. Aksay, *ACS Applied Materials & Interfaces* **2012**, *4*, 2794.
- [157] J. Jiang, Y. Li, J. Liu, X. Huang, *Nanoscale* **2011**, *3*, 45.
- [158] P. L. Taberna, S. Mitra, P. Poizot, P. Simon, J. M. Tarascon, *Nature Materials* **2006**, *5*, 567.
- [159] Y. Shi, Y. Xu, S. Zhuo, J. Zhang, B. Zhang, *ACS Applied Materials and Interfaces* **2015**, *7*, 2376.
- [160] Y. Yang, H. Fei, G. Ruan, J. M. Tour, *Advanced Materials* **2015**.
- [161] J. Tian, Q. Liu, A. M. Asiri, X. Sun, *Journal of the American Chemical Society* **2014**, *136*, 7587.
- [162] R. Madhu, V. Veeramani, S.-M. Chen, P. Veerakumar, S.-B. Liu *Chemistry – A European Journal* **2015**.
- [163] R. Pöttgen, W. Höhle, H. G. von Schnering, *Encyclopedia of Inorganic Chemistry*, **2006**.
- [164] V. Pejović, L. J. Radonjić, M. Jančić, *Thin Solid Films* **1986**, *145*, 213.
- [165] C. Schmetterer, J. Vizdal, H. Ipser, *Intermetallics* **2009**, *17*, 826.
- [166] S. V. Muchnik, V. G. Ivanchenko, V. B. Chernogorenko, K. A. Lynchak, *Soviet Powder Metallurgy and Metal Ceramics* **1979**, *18*, 357.
- [167] E. Muthuswamy, G. H. L. Savithra, S. L. Brock, *ACS Nano* **2011**, *5*, 2402.
- [168] R. Merkle, J. Maier, *Zeitschrift für anorganische und allgemeine Chemie* **2005**, *631*, 1163.
- [169] W. W. Smeltzer, R. R. Haering, J. S. Kirkaldy, *Acta Metallurgica* **1961**, *9*, 880.
- [170] M. Ledendecker, S. Krick Calderón, C. Papp, H.-P. Steinrück, M. Antonietti, M. Shalom, *Angewandte Chemie International Edition* **2015**, *54*, 12361.
- [171] B. Elsener, M. Crobuz, M. Scorciapino, A. Rossi, *Journal of Applied Electrochemistry* **2008**, *38*, 1053.
- [172] D. S. Hall, C. Bock, B. R. MacDougall, *Journal of The Electrochemical Society* **2013**, *160*, F235.
- [173] R. Franke, T. Chassé, P. Streubel, A. Meisel, *Journal of Electron Spectroscopy and Related Phenomena* **1991**, *56*, 381.
- [174] V. Babizhetskyy, B. Kotur, S. Oryshchyn, C. Zheng, F. Kneidinger, L. Leber, C. Simson, E. Bauer, H. Michor, *Solid State Communications* **2013**, *164*, 1.
- [175] K. Mi, Y. Ni, J. Hong, *Journal of Physics and Chemistry of Solids* **2011**, *72*, 1452.
- [176] A. Matsuda, R. Notoya, *Journal of the Research Institute for Catalysis Hokkaido University* **1966**, *14*.
- [177] T. Yamazaki, M. Enyo, *Electrochimica Acta* **1990**, *35*, 523.
- [178] J. Barber, S. Morin, B. E. Conway, *Journal of Electroanalytical Chemistry* **1998**, *446*, 125.
- [179] A. C. Chialvo, M. R. Gennero de Chialvo, *Journal of Applied Electrochemistry* **1991**, *21*, 440.
- [180] K. Xu, P. Chen, X. Li, Y. Tong, H. Ding, X. Wu, W. Chu, Z. Peng, C. Wu, Y. Xie, *Journal of the American Chemical Society* **2015**, *137*, 4119.
- [181] B. T. Zhu, Z. Wang, S. Ding, J. S. Chen, X. W. Lou, *RSC Advances* **2011**, *1*, 397.
- [182] W. Zhou, X.-J. Wu, X. Cao, X. Huang, C. Tan, J. Tian, H. Liu, J. Wang, H. Zhang, *Energy & Environmental Science* **2013**, *6*, 2921.
- [183] A. T. Swesi, J. Masud, M. Nath, *Energy & Environmental Science* **2016**.
- [184] B. You, Y. Sun, *Advanced Energy Materials* **2016**, n/a.
- [185] M. T. M. Koper, *Journal of Electroanalytical Chemistry* **2011**, *660*, 254.
- [186] J. Rossmeisl, Z. W. Qu, H. Zhu, G. J. Kroes, J. K. Nørskov, *Journal of Electroanalytical Chemistry* **2007**, *607*, 83.
- [187] P. W. T. Lu, S. Srinivasan, *Journal of the Electrochemical Society* **1978**, *125*, 1416.
- [188] H. Bode, K. Dehmelt, J. Witte, *Electrochimica Acta* **1966**, *11*, 1079.
- [189] M. Fleischmann, K. Korinek, D. Pletcher, *Journal of the Chemical Society, Perkin Transactions 2* **1972**, 1396.
- [190] D. Giovanelli, N. S. Lawrence, L. Jiang, T. G. J. Jones, R. G. Compton, *Sensors and Actuators B: Chemical* **2003**, *88*, 320.
- [191] J. L. Weininger, M. W. Breiter, *Journal of The Electrochemical Society* **1963**, *110*, 484.
- [192] Y. Miao, L. Ouyang, S. Zhou, L. Xu, Z. Yang, M. Xiao, R. Ouyang, *Biosensors and Bioelectronics* **2014**, *53*, 428.

- [193] R. Kostecki, F. McLarnon, *Journal of The Electrochemical Society* **1997**, *144*, 485.
- [194] Y. L. Lo, B. J. Hwang, *Langmuir* **1998**, *14*, 944.
- [195] J. L. Bantignies, S. Deabate, A. Righi, S. Rols, P. Hermet, J. L. Sauvajol, F. Henn, *The Journal of Physical Chemistry C* **2008**, *112*, 2193.
- [196] M. W. Louie, A. T. Bell, *Journal of the American Chemical Society* **2013**, *135*, 12329.
- [197] P. Hermet, L. Gourrier, J. L. Bantignies, D. Ravot, T. Michel, S. Deabate, P. Boulet, F. Henn, *Physical Review B* **2011**, *84*, 235211.
- [198] P. Oliva, J. Leonardi, J. F. Laurent, C. Delmas, J. J. Braconnier, M. Figlarz, F. Fievet, A. d. Guibert, *Journal of Power Sources* **1982**, *8*, 229.
- [199] P. Larkin, *Infrared and Raman Spectroscopy*, Oxford, **2011**, pp. 135.
- [200] J. W. Lee, J. M. Ko, J.-D. Kim, *The Journal of Physical Chemistry C* **2011**, *115*, 19445.
- [201] G. S. Manku, *Theoretical Principles of Inorganic Chemistry*, Tata McGraw-Hill, **1980**.
- [202] M. R. G. De Chialvo, A. C. Chialvo, *Electrochimica Acta* **1993**, *38*, 2247.
- [203] L. Trotochaud, S. L. Young, J. K. Ranney, S. W. Boettcher, *Journal of the American Chemical Society* **2014**, *136*, 6744.
- [204] B. O. Fowler, *Inorganic Chemistry* **1974**, *13*, 194.
- [205] M. Salarian, W. Z. Xu, Z. Wang, T.-K. Sham, P. A. Charpentier, *ACS Applied Materials and Interfaces* **2014**, *6*, 16918.
- [206] J. McBreen, *Handbook of Battery Materials*, **2007**, pp. 135.
- [207] L. C. Seitz, B. A. Pinaud, D. Nordlund, Y. Gorlin, A. Gallo, T. F. Jaramillo, *Journal of The Electrochemical Society* **2015**, *162*, H841.
- [208] A. Bergmann, E. Martinez-Moreno, D. Teschner, P. Chernev, M. Gliech, J. F. de Araujo, T. Reier, H. Dau, P. Strasser, *Nature Communications* **2015**, *6*.
- [209] J. O. Bockris, *The Journal of Chemical Physics* **1956**, *24*, 817.
- [210] T. Osaka, Y. Iwase, H. Kitayama, T. Ichino, *Bulletin of the Chemical Society of Japan* **1983**, *56*, 2106.
- [211] J. Luo, J. Im, M. T. Mayer, M. Schreier, M. K. Nazeeruddin, N.-G. Park, S. D. Tilley, H. J. Fan, M. Grätzel, *Science* **2014**, *345*, 1593.
- [212] K. Manandhar, D. Pletcher, *Journal of Applied Electrochemistry* **1979**, *9*, 707.
- [213] F. Harnisch, G. Sievers, U. Schröder, *Applied Catalysis B: Environmental* **2009**, *89*, 455.
- [214] W.-F. Chen, K. Sasaki, C. Ma, A. I. Frenkel, N. Marinkovic, J. T. Muckerman, Y. Zhu, R. R. Adzic, *Angewandte Chemie International Edition* **2012**, *51*, 6131.
- [215] M. Caban-Acevedo, M. L. Stone, J. R. Schmidt, J. G. Thomas, Q. Ding, H. Chang, M. Tsai, J. He, S. Jin, *Nature Materials* **2015**, *14*, 1245.
- [216] J. K. Nørskov, T. Bligaard, A. Logadottir, J. R. Kitchin, J. G. Chen, S. Pandalov, U. Stimming, *Journal of The Electrochemical Society* **2005**, *152*, J23.
- [217] H. Schlott, Friedrich-Alexander-Universität Erlangen-Nürnberg **2015**.
- [218] G. Hägg, *Zeitschrift für Physikalische Chemie* **1931**, *12*, 33.
- [219] B. Cordero, V. Gomez, A. E. Platero-Prats, M. Reves, J. Echeverria, E. Cremades, F. Barragan, S. Alvarez, *Dalton Transactions* **2008**, 2832.
- [220] A. Wang, H. Wang, S. Zhang, C. Mao, J. Song, H. Niu, B. Jin, Y. Tian, *Applied Surface Science* **2013**, *282*, 704.
- [221] T.-W. Lin, C.-S. Dai, K.-C. Hung, *Scientific Reports* **2014**, *4*, 7274.
- [222] W. Duan, W. Yan, X. Yan, H. Munakata, Y. Jin, K. Kanamura, *Journal of Power Sources* **2015**, *293*, 706.
- [223] L.-L. Feng, G. Yu, Y. Wu, G.-D. Li, H. Li, Y. Sun, T. Asefa, W. Chen, X. Zou, *Journal of the American Chemical Society* **2015**, *137*, 14023.
- [224] N. Cheng, Q. Liu, A. M. Asiri, W. Xing, X. Sun, *Journal of Materials Chemistry A* **2015**, *3*, 23207.
- [225] C. Tang, Z. Pu, Q. Liu, A. M. Asiri, Y. Luo, X. Sun, *International Journal of Hydrogen Energy* **2015**, *40*, 4727.

- [226] N. Jiang, Q. Tang, M. Sheng, B. You, D. Jiang, Y. Sun, *Catalysis Science & Technology* **2015**.
- [227] S. M. Dharmaprakash, *Crystal Research and Technology* **1996**, *31*, K49.
- [228] G. V. Gibbs, R. T. Downs, C. T. Prewitt, K. M. Rosso, N. L. Ross, D. F. Cox, *The Journal of Physical Chemistry B* **2005**, *109*, 21788.
- [229] Y. Liao, K. Pan, Q. Pan, G. Wang, W. Zhou, H. Fu, *Nanoscale* **2015**, *7*, 1623.
- [230] X. Zhu, Z. Wen, Z. Gu, S. Huang, *Journal of The Electrochemical Society* **2006**, *153*, A504.
- [231] T. Matsumura, K. Nakano, R. Kanno, A. Hirano, N. Imanishi, Y. Takeda, *Journal of Power Sources* **2007**, *174*, 632.
- [232] S.-W. Chou, J.-Y. Lin, *Journal of The Electrochemical Society* **2013**, *160*, D178.
- [233] C.-W. Su, J.-M. Li, W. Yang, J.-M. Guo, *The Journal of Physical Chemistry C* **2014**, *118*, 767.
- [234] Q. Han, K. Liu, J. Chen, X. Wei, *International Journal of Hydrogen Energy* **2003**, *28*, 1207.
- [235] J.-Y. Lin, W.-Y. Wang, Y.-T. Lin, S.-W. Chou, *ACS Applied Materials & Interfaces* **2014**, *6*, 3357.
- [236] B. Busupalli, K. Date, S. Datar, B. L. V. Prasad, *Crystal Growth & Design* **2015**, *15*, 2584.
- [237] A. Stokłosa, J. Stringer, *Oxidation of Metals* **1977**, *11*, 263.
- [238] H. Kiuchi, K. Funaki, T. Tanaka, *Metallurgical Transactions B* **1983**, *14*, 347.
- [239] M. Shalom, D. Ressnig, X. Yang, G. Clavel, T. P. Fellingner, M. Antonietti, *Journal of Materials Chemistry A* **2015**, *3*, 8171.
- [240] G. Clavel, V. Molinari, A. Kraupner, C. Giordano, *Chemistry – A European Journal* **2014**, *20*, 9018.
- [241] G. J. W. R. Dorman, M. Sikkens, *Thin Solid Films* **1983**, *105*, 251.
- [242] M. Kawamura, Y. Abe, K. Sasaki, *Vacuum* **2000**, *59*, 721.
- [243] J. Choi, E. G. Gillan, *Inorganic Chemistry* **2009**, *48*, 4470.
- [244] R. Juza, W. Sachsze, *Zeitschrift für anorganische Chemie* **1945**, *253*, 95.
- [245] G. T. Beilby, G. G. Henderson, *Journal of the Chemical Society* **1901**, *79*, 1251.
- [246] R. Juza, W. Sachsze, *Zeitschrift für anorganische und allgemeine Chemie* **1943**, *251*, 201.
- [247] A. Fernández Guillermet, K. Frisk, *International Journal of Thermophysics* **1991**, *12*, 417.
- [248] C. C. L. McCrory, S. Jung, J. C. Peters, T. F. Jaramillo, *Journal of the American Chemical Society* **2013**, *135*, 16977.
- [249] J. Tamm, L. Tamm, *Research in Chemical Kinetics*, Amsterdam, **1995**, pp. 215.
- [250] D. Y. Chung, J. W. Han, D.-H. Lim, J.-H. Jo, S. J. Yoo, H. Lee, Y.-E. Sung, *Nanoscale* **2015**, *7*, 5157.
- [251] D. Y. Chung, J. W. Han, D. Lim, J. Jo, S. J. Yoo, H. Lee, Y. Sung, *Nanoscale* **2015**, *7*, 5157.
- [252] T.-W. Lin, C.-J. Liu, C.-S. Dai, *Applied Catalysis B: Environmental* **2014**, *154–155*, 213.
- [253] N. Jiang, Q. Tang, M. Sheng, B. You, D.-e. Jiang, Y. Sun, *Catalysis Science & Technology* **2015**.
- [254] W. M. Haynes, *CRC Handbook of Chemistry and Physics, 93rd Edition*, Taylor & Francis, **2012**.
- [255] J. Greeley, J. K. Nørskov, L. A. Kibler, A. M. El-Aziz, D. M. Kolb, *ChemPhysChem* **2006**, *7*, 1032.
- [256] B. Hammer, J. K. Nørskov, *Surface Science* **1995**, *343*, 211.
- [257] M. Mavrikakis, B. Hammer, J. K. Nørskov, *Physical Review Letters* **1998**, *81*, 2819.
- [258] P. Zhang, X. Wang, W. Wang, X. Lei, W. Yin, H. Yang, *RSC Advances* **2015**, *5*, 68758.
- [259] W. F. Chen, C. H. Wang, K. Sasaki, N. Marinkovic, W. Xu, J. T. Muckerman, Y. Zhu, R. R. Adzic, *Energy & Environmental Science* **2013**, *6*, 943.
- [260] U.S. Department of the Interior, U.S. Geological Survey, Mineral Commodity Summaries. <http://minerals.usgs.gov/minerals/pubs/mcs/> (accessed 12.11.2015).
- [261] M. Thompson, J. N. Walsh, *Handbook of inductively coupled plasma spectrometry*, Blackie, **1989**.
- [262] M. Asha Jhonsi, A. Kathiravan, G. Paramaguru, C. Manivannan, R. Renganathan, *Journal of Solution Chemistry* **2010**, *39*, 1520.
- [263] C. D. Geddes, J. R. Lakowicz, *Advanced Concepts in Fluorescence Sensing: Part B: Macromolecular Sensing*, Springer, **2010**.



## **Acknowledgements and personal contribution**

To begin with, I would like to express my gratitude to Markus Antonietti for giving me the opportunity to work in his department and for giving me insights in how to coalesce leadership and research.

In direct continuation, I would like to thank my direct supervisor Menny Shalom for introducing me to the field of electrocatalysis, his constant support, scientific enthusiasm and discussions as well as the opportunity to work with a high degree of autonomy.

Many thanks go to Jonas for all the fun in the office and copious exchange of ideas.

I thank Katharina Otte for taking care of our group, all the work we did together and general help.

Moreover, I thank Guylhaine Clavel, Hannah Schlott, Bernd Meyer, Sandra Krick Calderón, Christian Papp, and Hans-Peter Steinrück for the successful collaborations.

I thank everybody with whom I had fruitful scientific discussions and who helped to increase the quality of the presented thesis, especially Guylhaine, Debora, Jonas, Tim, Valerio, Thomas, Hannah, Florian, Klaus, and Laurent.

I thank Sylvia, Ursula, Heike, Rona, Jeanette, Bodo, Klaus and Tina for their help in many measurements and the technical equipment.

A special thank goes to my life partner, Ana, for her constant support and motivation during my PhD.

And, of course, my parents, grandmother and brother who always supported me in my decisions.

## 10 Declaration

---

Die vorliegende Dissertation entstand im Zeitraum zwischen September 2013 und Januar 2016 am Max-Planck-Institut für Kolloid und Grenzflächenforschung unter Betreuung von Prof. Dr. Dr. h.c. Markus Antonietti.

Hiermit erkläre ich, dass die vorliegende Arbeit selbstständig angefertigt wurde und keine anderen als die angegebenen Hilfsmittel und Quellen verwendet wurden.

The present work was carried out during the period from September, 2013 to January, 2016 at the Max Planck Institute of Colloids and Interfaces under supervision of Prof. Dr. Dr. h.c. Markus Antonietti.

I declare that I have written this work on my own and used no other than the named aids and references.

Marc Ledendecker

Potsdam, 19.01.2016